Review of the Bird Critique

by the Seismic Review Team of the Diablo Canyon Independent Safety Committee

Thomas H. Jordan (chair)

Department of Earth Sciences, University of Southern California, Los Angeles, CA 91103

Michael E. Oskin

Earth and Planetary Sciences Department, University of California Davis, Davis, CA 95616

Scott T. Marshall

Department of Geological and Environmental Sciences, Appalachian State University, Boone, NC 28608

Submitted to the Diablo Canyon Independent Safety Committee on May 30, 2025.

Summary

In filings to the U.S. Nuclear Regulatory Commission (NRC), the Diablo Canyon Independent Safety Committee (DCISC), and the California Public Utilities Commission (CPUC), Dr. Peter Bird, professor emeritus at the University of California, Los Angeles, contends that the seismic hazard at the Diablo Canyon Power Plant (DCPP) has been underestimated by Pacific Gas and Electric Company (PG&E), the plant's operator. The Bird critique comprises three main assertions: (a) In developing the seismic source characterization (SSC) used in the DCPP probabilistic seismic hazard assessment, PG&E (2015, 2024) made four false assumptions. Removing these assumptions increases the thrust-faulting rate beneath the Irish Hills by a large factor. (b) Three independent analytic methods give values for the total slip rate on shallow-dipping thrust faults under the Irish Hills in the range of 2.0-2.8 mm/yr. (c) The January 1, 2024, Noto Peninsula (Japan) earthquake (magnitude 7.5, abbreviated Noto24) is a good analog for a large thrust event beneath the Irish Hills, and the recurrence interval of a Noto24-type earthquake involving Irish Hills thrust faulting is 715-1000 yr, posing an unacceptable risk to the DCPP.

The SRT analysis discounts the plausibility of all three assertions. (a) Removing the four false assumptions in the development of a revised SSC would have little to no impact on the hazard estimates. (b) Fault system analysis yields a total slip rate of 0.29 ± 0.07 mm/yr on thrust faults beneath the Irish Hills, an order of magnitude smaller than Dr. Bird's estimates. A strain-rate analysis of Zeng's (2022) GPS velocities indicates both contraction and right-lateral shearing across and beyond the Irish Hills, consistent with transpressional tectonics. The estimation uncertainties are large (± 10 nanostrain/yr), but the contractional strain rate averaged across the Irish Hills (20-40 nanostrain/yr) is significantly lower than Dr. Bird's estimate (80-100 nanostrain/yr). (c) Based on the anomalous characteristics of Noto24, including its extreme length and high stress drop, the SRT finds that a Noto24-type earthquake is not suitable as a characteristic earthquake for thrust faulting beneath the Irish Hills. The SRT concludes that the best available science does not support the three main assertions of the Bird critique.

The SRT also addresses several technical issues raised by Dr. Bird. Assuming an Airy compensation mechanism, he claims that active thrust faulting must explain not only the 0.2 mm/yr uplift rate of the Irish Hills but also a crustal thickening rate that is about six times larger. The SRT concludes that Airy isostasy cannot be applied to the compensation of loads of as small as the Irish Hills, and it agrees with published results showing that the gravity anomalies associated with the Pismo Syncline and Irish Hills can be successfully explained by plausible models based on rigid plate-compensation without Moho variations.

Dr. Bird has questioned whether the high-angle reverse faulting in the SSC model is mechanically feasible, asserting that faults with dips of 50º-80º are mechanically impossible in the present horizontal compressive stress regime. From a review of the mechanics of fault initiation and reactivation, the SRT

concludes that reverse faulting at dip angles of 50º-80º is mechanically feasible in the transpressional regime of the Irish Hills and widely observed in inverted basin-bounding fault systems around the world.

The Southwestern Boundary Zone (SWBZ), including its possible reverse-faulting extensions along strike, was identified by PG&E, and also by Dr. Bird, as the fault system most likely to produce the largest reverse-slip earthquakes beneath the Irish Hills; the SRT agrees with this assessment. The geological structure of the Irish Hills indicates a moderate (38º ± 3º) dip of the SWBZ, consistent with fault-outcrop observations and reactivation of steeply dipping normal faults in its hangingwall to fold the Pismo Syncline. The SRT bases the SWBZ slip rates on this mean dip and a mean uplift rate of 0.18 ± 0.03 mm/yr since 124 ka ± 2.5. This short-term rate of 0.29 ± 0.07 mm/yr is marginally lower than the long-term (5.1 ± 0.4 Ma) slip rate of 0.50 ± 0.10 mm/yr inferred for the SWBZ from the kinematically constrained fault analysis.

The SRT makes several recommendations for future research that could further elucidate the hazards associated with reverse faulting beneath the Irish Hills. As Dr. Bird has emphasized in his critique, PG&E does not have a geometric model of faulting of the Irish Hills that kinematically reproduces observed folding of the Irish Hills since 5 Ma. Fault-bend fold theory provides a framework to refine existing source model geometries and reveal possible sources outside of those considered by the PG&E SSC. The SRT has derived a plausible, though preliminary, fault-bend fold model for the SWBZ, and it recommends further work to develop kinematically constrained structural models that more thoroughly explore the possible configurations of reverse faults beneath the Irish Hills.

The SRT recommends that PG&E follow up the SRT's preliminary geodetic analysis with a more complete study of the GPS data to include the examination of cross-structural profiles, strain-rate inversions, and the development of regional models that can accurately correct the GPS velocities for the interseismic deformation due to faults with known geometries and slip rates. The SRT further recommends that the fault-slip models that underlie the DCPP SSC be developed into kinematic and mechanical models that can be directly tested against the GPS data. In the long term, PG&E should consider implementing the NSHM methodology that uses an ensemble of deformation models (including NeoKinema), driven by a common set of inputs, to validate the slip rate and fault geometry inputs to the hazard models.

The SRT has not formally assessed the current SSC model, but the findings of this study regarding thrust faulting beneath the Irish Hills may be useful in future assessments. The SRT recommends modeling experiments to ascertain the sensitivity of DCPP hazard to the recommended SSC modifications. PG&E should specifically reexamine the weighting of alternative fault geometry models, and it should assess the impact of placing significantly more weight on and lowering the dip range of the SW-Vergent model, which better represents the likely reverse-fault hazard.

Table of Contents

1. Introduction 5

1.1. Charge to the Seismic Review Team 5

1.2. Review Process 6

2. Annotated Summary of the Bird Critique 7

2.1. Geological Framework and Hazard Expectations 8

2.2. Four False Assumptions in the Development of SSC15 and SSC24 11

2.3. Estimating the Total Rate of Thrust Faulting under the Irish Hills 22

2.4. A Characteristic Thrust Earthquake 28

2.5. Conclusion: Seismic Core Damage Frequency at DCPP 31

2.6. Appendix A: Missing Procedural Steps in the SSCs by PG&E (2015, 2024) 32

2.7. Appendix B: Dismissal of PG&E's Objection to the Noto Peninsula Earthquake Model 34

2.8. Statements from Other Documents of the Bird Critique 36

3. Technical Analyses 39

3.1. Gravimetric Analysis 39

3.2. Fault Reactivation Analysis 41

3.3. Fault System Analysis 44

3.4. Geodetic Analysis 51

3.5. Analysis of the 2024 Noto Peninsula earthquake 67

4. Findings and Recommendations 75

4.1. Bird's Critique of PG&E Modeling Assumptions 76

4.2. Bird's Estimates of Slip Rates 77

4.3. Noto24 as an Analog Earthquake 79

4.4. Overall Assessment of the Bird Critique 80

4.5. Findings Regarding the SSC model 80

4.6. Recommendations for Future Work 82

5. References 84

Appendix A: Biographical Sketches of SRT members 92

Thomas H. Jordan 92

Michael E. Oskin 92

Scott T. Marshall 93

Appendix B: Supplementary Figures 94

1. Introduction

Dr. Peter Bird has challenged four assumptions he states were made by Pacific Gas and Electric Company (PG&E) in developing the Seismic Source Characterization (SSC) model for the Diablo Canyon Power Plant (DCPP), and he has argued that the seismic hazard at DCPP from one or more thrust faults beneath the Irish Hills is much higher than projected by the PG&E SSC model. At its public meeting on February 19, 2025, the Diablo Canyon Independent Safety Commission (DCISC) appointed a Seismic Review Team (SRT) to conduct a peer review of the Bird critique. The SRT members are Drs. Thomas H. Jordan, Michael E. Oskin, and Scott T. Marshall. Their biographical sketches are given in Appendix A.

1.1. Charge to the Seismic Review Team

The DCISC charged the SRT to conduct a peer review of six reports submitted by Dr. Bird to the DCISC, the California Public Utilities Commission (CPUC), and the U.S. Nuclear Regulatory Commission (NRC) regarding the seismic hazard at the Diablo Canyon Power Plant (DCPP). These reports are referenced in chronological order and abbreviated as B1 through B6:

B1. *Opening Testimony of Dr. Peter Bird on Behalf of San Luis Obispo Mothers for Peace on Phase 1 Track 2 Issues* (R.23-01-007, 24 pp.), submitted to the CPUC on January 14, 2023.

B2. *Declaration of Peter Bird, Ph.D.* (50-275-LR, 26 pp.), submitted to the NRC by San Luis Obispo Mothers for Peace, Friends of the Earth, and Environmental Working Group on March 4, 2024.

B3. *Response to PG&E SSC and 2024 Update* (8 pp.), letter from Dr. Peter Bird submitted to the DCISC on May 16, 2024.

B4. *Supplemental Declaration of Peter Bird*, Ph.D (50-275, 50-323, 14 pp.), submitted to the NRC on June 7, 2024.

B5. *Correcting 4 False Assumptions in PG&E's Seismic Source Characterization [2015] and Update [2024] that Caused PG&E to Seriously Underestimate Seismic Hazard at Diablo Canyon Nuclear Power Plant* (27 viewgraphs), presentation by Dr. Peter Bird to the NRC Petition Review Board on July 17, 2024.

B6. *High Seismic Hazard and Risk at Diablo Canyon Power Plant Due to Thrust Faulting Under the Irish Hills* (27 pp.), submitted to the DCISC on October 30, 2024.

These reports, taken together, constitute the Bird critique. Report B6 summarizes Dr. Bird's main arguments and conclusions and is the focus of the SRT review.

1.2. Review Process

The SRT has reviewed Dr. Bird's submitted documents (B1-B6), and it has evaluated Dr. Bird's conclusions based on the best science available from the published literature, public PG&E reports, and expert knowledge. The Bird critique is primarily directed at the 2015 SSC model and its 2024 update. The SSC models are described in two PG&E reports:

- *Seismic Source Characterization for the Diablo Canyon Power Plant, San Luis Obispo County*, California (PG&E, March 2015, 682 pp. & Appendices A-H), here referred to as the "SSC15 report".
- *Diablo Canyon Updated Seismic Assessment, Response to Senate Bill 846* (PG&E, March 2024, 394 pp.), here referred to as the "SSC24 report".

The SSC15 model is the backbone of the current DCPP source model. The SSC24 update did not make any substantive changes to the structure of the SSC15 model (e.g., fault-system geometry), only changes to slip rates of the Hosgri and Los Osos faults and related quantities. For the purposes of this review, the SSC15 and SSC24 models are essentially the same.

Dr. Bird first presented his ideas during the SSC15 SSHAC Level 3 review, and he further developed his critique in reports submitted to the NRC, CPUC, and DCISC in 2023 and 2024. In addition to Dr. Bird's submissions, the SRT considered PG&E's rebuttals of the Bird critique in the SSC24 report (Chapter 6), the materials presented by Dr. Christopher Madugo and Dr. Albert Kottke to the DCISC at the public meeting of October 9, 2024 (Madugo & Kottke, 2024), and the NRC response (ML24302A148) of April 10, 2025.

The SRT began its review in February 2025 and paced its progress with weekly on-line meetings. During the review, the SRT members, individually and together, consulted widely with subject-matter experts in California and worldwide. The SRT also met with Dr. Peter Bird (on-line Tuesday, March 18, 2025) and PG&E representatives (in-person Friday, March 28, 2025).

The purpose of the meeting with Dr. Bird was to confirm the SRT's understanding of his arguments for high-hazard thrust faulting beneath the Irish Hills and to allow him to provide the SRT with more details about his main scientific points. During this 75-min meeting, the SRT posed 13 pre-written questions about his critique, and all were satisfactorily answered by Dr. Bird.

The PG&E session took place in-person at DCPP and was organized as a DCISC fact-finding meeting.[1] As part of this meeting, the SRT toured DCPP and briefly examined some faults in areas near the plant. Two weeks before the meeting, the SRT submitted an 11-page document to PG&E through the DCISC containing about 40 questions. None of the SRT members were directly involved in the development of the SSC15 or

[1] DCISC Report on Special Fact-Finding Meeting at DCPP on March 28, 2025, by N. Meshkati, R. McWhorter & A. Kadak, 9 pp.

the SSC24 models, and many of the questions we posed to PG&E were intended to fill gaps in the SRT's understanding of the data sets, modeling assumptions, and SSC structure. At the fact-finding meeting, the PG&E team[2] responded with written answers to most of the questions and oral answers to others. As anticipated, PG&E was able to respond to many of the questions by citing the relevant parts of the public reports that document the SSC models.

The SRT met with the technical team of the Independent Peer Review Panel (IPRP) involved in assessing the Bird critique on Friday, April 25, 2025.[3] We discussed constraints on the location and dip of thrust faults beneath DCPP, and the information geodesy could provide for understanding the regional shortening rate. We also discussed the nature of the Los Osos trend, including evidence for strike-slip faulting in offshore seismic reflection data. We touched on the PG&E-supported precariously balanced rock studies at Double Rock sea stack as evidence against ground acceleration levels of a Noto24-type event, but we found that this evidence is not sufficiently validated to be incorporated into SSC models. The SRT also shared some initial analyses of geodetic data and discussed complications in the region that arise due to the nearby San Andreas fault.

2. Annotated Summary of the Bird Critique

The most complete statement of Dr. Bird's critique is his DCISC report of October 30, 2024 (B6). The annotated summary in this section is taken largely from that document. A few salient points emphasized by Dr. Bird in three other submissions (B1, B2, and B3), but not in B6, are also included in §2.8.

The summarized points taken from the Bird documents are listed in a blue font. The text is largely verbatim, although it has been edited to follow the notation and referencing conventions of this report; unneeded explanatory material has not been included, and some points have been rephrased for precision and clarity. The points are listed in the same order as B6, and they are sequentially indexed to allow for precise referencing. The SRT considers the set of points listed in this section to be a full and complete description of the Bird critique.

The SRT comments on a point-by-point basis are given in a black font. In many cases, the comments refer to the technical material given in §3, which includes the SRT analyses of the gravimetric data (§3.1),

[2] The PG&E participants were Jeff Bachhuber, Director, Geosciences; Albert Kottke, Principal Geotechnical Earthquake Engineer; Chris Madugo, Geosciences Consultant; Steve Thompson, Contractor from Lettis Consultants International; Jearl Strickland, Consultant/Former PG&E Director; Tom Jones, Senior Director, Regulatory, Environmental and Repurposing; Philippe Soenen, Strategic Initiatives Director; and Brandy Lopez, Licensing Program Manager (DCISC Liaison and Visit Coordinator).

[3] The IPRP participants were Tim Dawson and Gordon Seitz of the California Geological Survey (CGS) and Phil Johnson of the California Coastal Commission.

fault reactivation conditions (§3.2), fault system geometry and kinematics (§3.3), geodetic data and models (§3.4), and the 2024 Noto Peninsula (Noto Hanto) earthquake as an analog for large thrust faulting beneath the Irish Hills (§3.5). The SRT commentaries on the Bird points given in §2 and §3 are developed into a set of findings and recommendations in §4.

The earthquake magnitudes referenced in this document are assumed to be moment magnitudes, denoted **M**, unless otherwise stated. The seismic moment of an earthquake is defined to be $M_0 = \mu AD$, where μ is the average shear modulus of the faulted rocks, A is the area of faulting, and D is the average displacement (slip) over this area. The U.S. Geological Survey (USGS) defines the moment magnitude to be $\mathbf{M} = \frac{2}{3}(\log M_0 \ - 9.1)$, where M_0 is expressed in Newton-meters (Nm).

In our review comments, we use the term 'reverse fault' to describe an inclined, dipping fault with upward slip of the hangingwall over the footwall. We reserve the term 'thrust fault' to describe a reverse fault with a dip of 45° or less. We note that the Bird documents use the term 'thrust fault' interchangeably with 'reverse fault'.

For the sake of brevity, we refer to the suite of faults bounding the southern margin of Irish Hills as the Southwest Boundary Zone (SWBZ), following the definition established by PG&E. This includes the San Luis Bay fault, Rattlesnake fault and Olson fault in the west, closest to the DCPP, and the Wilmar Avenue fault, Los Berros fault, and Oceano fault in the east, offshore of Pismo Beach. Together, these faults accommodate shortening and uplift of the Irish Hills and San Luis Range, collectively referred to as the San Luis-Pismo Block (SLPB) of the Los Osos domain (Lettis & Hall, 1994). We will refer to the "greater Irish Hills region" to identify the region comprising the GPS stations used in the geodetic analysis, which extends northeastward of the SLPB.

We refer to the observed structure(s) bounding the northern margin of the Irish Hills as the Los Osos trend instead of the Los Osos fault. This terminology reflects the ambiguity of the nature of this boundary, which may be a reverse fault, strike-slip fault, or a fold hinge without significant faulting (PG&E 2014a). Where referring to the PG&E SSC, we refer to the Los Osos fault for consistency with the source model.

The SRT has strived to include realistic uncertainties on the data values and model estimates, usually by treating the random variables as normally distributed and independent. The uncertainties are cited as standard deviations about the mean ($\mu \pm \sigma$) or as 95% confidence intervals ($\mu - 1.96\, \sigma$, $\mu + 1.96\, \sigma$).

2.1. Geological Framework and Hazard Expectations

a. The basement beneath the Irish Hills is formed by rocks of the Franciscan Complex, which developed as an accretionary prism to the California Arc during rapid Farallon plate subduction beneath the North America plate in the interval 80-200 Ma.

b. The Irish Hills and the San Luis Range are a younger dextral-transpressional orogen that has formed since 6 Ma, when the motion of the Pacific plate changed its direction to become more compressional relative to North America.

c. The region is cut by a number of strike-slip and thrust faults.

d. The persistence of a horizontally compressive thrust-faulting stress regime up to the present is shown by the focal mechanisms of local and regional earthquakes, including the 2003 San Simeon (**M**6.6) and 1983 Coalinga (**M**6.2) earthquakes.

e. SSW-NNE directions of most-compressive stress shown by data in the World Stress Map are almost perpendicular to the traces of the regional thrust fault trend.

We accept points 2.1a-e with the understanding that Dr. Bird's use of the term 'thrust fault' here is synonymous with 'reverse fault' of unspecified dip.

f. This strongly suggests that currently these faults are either purely or dominantly thrusts, and that strike-slip is occurring only on the offshore Hosgri and perhaps Shoreline faults.

We do not agree with the inference that the compressive stress direction implies that the faults beneath the Irish Hills are either purely or dominantly thrusts. Earthquakes in the SLPB show the wide variation in focal mechanisms expected for a transpressional fault system (PG&E, 2015, 2024); the geodetic analysis of §3.4 confirms that the strain is transpressional, with a large SAF-parallel shear and a smaller SAF-normal compression. Resolved stress will depend on fault dip as well as strike direction. Under a transpressional regime, shortening in the direction of greatest compressive stress may be accomplished primarily by strike-slip faults that simultaneously lead to elongation in the perpendicular horizontal direction.

g. Given this geologic history and structure, one might expect to read in the SSC15 and SSC24 reports that thrust faulting under the Irish Hills is the major source of seismic hazard to DCPP. However, in the SSC15 report, the seismic hazard contributions (specifically, recurrence rates of PGA over 1 g and spectral accelerations over 2 g) of the Los Osos and San Luis Bay thrust faults add up to less than the hazard from the offshore strike-slip Hosgri fault, and consequently less than half of the total hazard. This imbalance remains uncorrected in the SSC24 report

We do not agree that the geologic history and structure imply that the hazard from the Los Osos fault and SWBZ (San Luis Bay and related faults), added together, should exceed either the Hosgri hazard or half of the total hazard. PG&E computes the DCPP hazard by combining the available information about the possible seismic sources using the methodology of probabilistic seismic hazard assessment

(PSHA), which is well developed, widely accepted, and standardized by the NRC (Budnitz et al., 1997; Baker et al., 2022). Figure 2.1 shows the DCPP mean hazard curves deaggregated by source type for spectral acceleration (SA) at 5 Hz. The relative contributions to the exceedance rate for 5Hz-SA = 2 g are Hosgri 45%, SWBZ 17%, Local Areal Source Zone 15%, Los Osos 15%, Shoreline 4%, other sources 4%. In the PSHA methodology, increasing the frequency of the largest reverse-slip earthquakes on faults beneath the Irish Hills will raise the hazard at high spectral accelerations but will necessarily reduce it at lower spectral accelerations, owing to the constraints on the total slip budget. Alternative low-angle thrust geometries only incrementally increase this budget. Assigning a higher rate of convergence across the Irish Hills would increase this budget further, but, as discussed below, the evidence does not support such an increase.

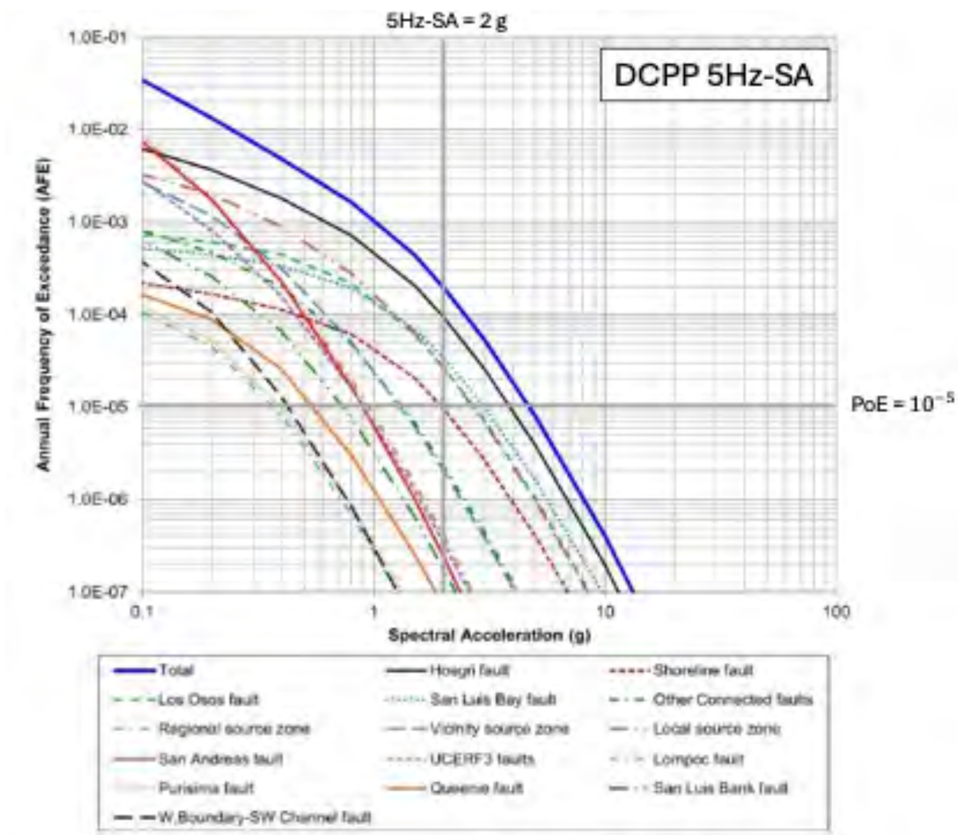

Figure 2.1. DCPP hazard curves for 5Hz-SA from the SSC24 model, deaggregated by source component. At 5Hz-SA = 2 g, the total DCPP exceedance rate is about 2 x 10^{-4} per year, and the relative contributions to the exceedance rate are Hosgri 45%, San Luis Bay 17%, Local Areal Source Zone 15%, Los Osos 15%, Shoreline 4%, other sources 4%. [Source: SSC24 report, fig. 5-14.]

2.2. Four False Assumptions in the Development of SSC15 and SSC24

a. One of the reasons that the SSC15 and SSC24 reports seriously underestimated seismic hazard due to thrust faulting is that they were guided by four assumptions that are actually false.

The assumptions stated by Dr. Bird involve simplifications and generalizations that go beyond the hypotheses that actually guided PG&E in the development of the SSC model.

2.2.1. "The Irish Hills are uplifting as a rigid block, with no internal deformation."

a. PG&E assumed that the Irish Hills are uplifting as a rigid block, with no internal deformation.

While it is true that the fault-based sources used in the SSC are consistent with block uplift of the Irish Hills, it is not correct to say that PG&E assumes that there is no internal deformation. Transpressive internal deformation is modeled by a Local Areal Source Zone that produces 70% strike-slip sources with magnitudes up to 7.0 and dips that range from 90º to 65º, and 30% reverse-slip sources with magnitudes up to 7.1 and dips that range from 70º to 35º (PG&E, 2015, sect. 13.5). The deaggregated hazard curves in Figure 2.1 show that the contribution of the Local Areal Source Zone to the exceedance rate measured at an 5Hz-SA = 1 g is the second largest; only the Hosgri source is larger. At 5Hz-SA = 2 g, Hosgri accounts for 45%, SWBZ for 17%, and the Local Areal Source Zone for 15%, tying with the Los Osos Fault in third place.

b. From this assumption, PG&E concluded that thrust faulting occurs only at the margins (Los Osos thrust, San Luis Bay thrust) with fault throw rates equal to marine terrace uplift rates of ~0.2 mm/year, and that thrust faulting occurs nowhere else.

The statement that thrust faulting occurs nowhere else is not correct, because the Local Areal Source Zone includes widely distributed reverse-slip sources. These sources are consistent with the internal structure of the Irish Hills, where geologic mapping indicates minor inversion of normal faults inherited from an earlier period of crustal extension, producing reverse slip and forced folds above steeply dipping (> 60°) faults. None of these internal structures produces measurable offset of marine terraces or other youthful geomorphic features (Hanson & Lettis, 1994; PG&E, 2014a). Such evidence occurs only at the margins of the Irish Hills along the Los Osos trend and along various onshore and offshore strands of the SWBZ (Lettis & Hall, 1994; Lettis et al., 1994).

c. However, the geologic map of the Irish Hills shows tight folding of Late Miocene sedimentary rocks has occurred since 6 ~ 5 Ma. Therefore, the Irish Hills are not rigid, and additional blind thrust faults are active in the interior.

Tight folds are defined by interlimb angles less than 30°, implying more than 50% shortening. The map-scale folds expressed in the Irish Hills are open folds, with interlimb angles greater than 70° (PG&E, 2014a; Weigers, 2021). Tight folding is present at outcrop-scale, especially within the Monterey formation, and is attributed to shortening as a result of flexural-slip folding. The estimated internal shortening ranges from 3.4% to 8.7% across the axis of the Pismo Syncline (PG&E, 2014a). The uniform elevation of marine-terrace platforms across these fold axes (Figure 2.2) shows that these folds are not presently tightening within the resolution of these reference horizons. Any model to produce the Pismo Syncline via ongoing fault-related folding must account for both the total deformation across the syncline and the ongoing surface deformation evident only at the northern and southern boundary of the Irish Hills (See §3.3). The Local Areal Source Zone is intended to represent the internal deformation of the Irish Hills and the possibility of blind-thrust sources.

d. According to geological mapping, the sedimentary beds in the Pismo have been rotated ~45º. This folding began after deposition of the youngest strata in the core of the fold (Tmpm), and prior to deposition of the Squire Member of the (Pliocene) Pismo Formation (Tpps), probably circa 5 Ma.

This statement is consistent with the geologic map relationships expressed within the Irish Hills and western San Luis Range.

e. This folding implies upper-crustal strains of ~0.8, and mean strain-rates of ~0.8 / 5 Ma = 5×10^{-15} per second, which is ~10× faster than rates of deformation of the modeled faults that are typical in the long-term neotectonics of the western U.S.

The 0.8 / 5 Ma strain estimate is equivalent to 160 nanostrain/yr, which is typical within the plate-boundary deformation zone along the entire length of the San Andreas fault (see Zeng, 2022, fig. 9). In a discussion with Dr. Bird, the SRT clarified that his estimate is a shear strain rate based on the ~40° tilt of the limbs of the Pismo Syncline with respect to horizontal. It should be recognized that the cumulative strain expressed as folding is not identical to the present pattern of strain accumulation evident in geodetic data and patterns of marine-terrace uplift. Reconciling these differences requires a kinematic model of fold growth in relation to underlying fault geometry, and consideration of the differing time frames for each type of measurement (see §3.3). The time-averaged strain rate since 5 Ma is not necessarily the same rate implied by Q2 marine-terrace uplift over the past 124.0 ± 2.5 ka (Marine Isotope Stage 5e highstand age from Simms et al, 2016). The analysis in §3.3 suggests that the 5-Ma rate is greater than the 120-ka rate.

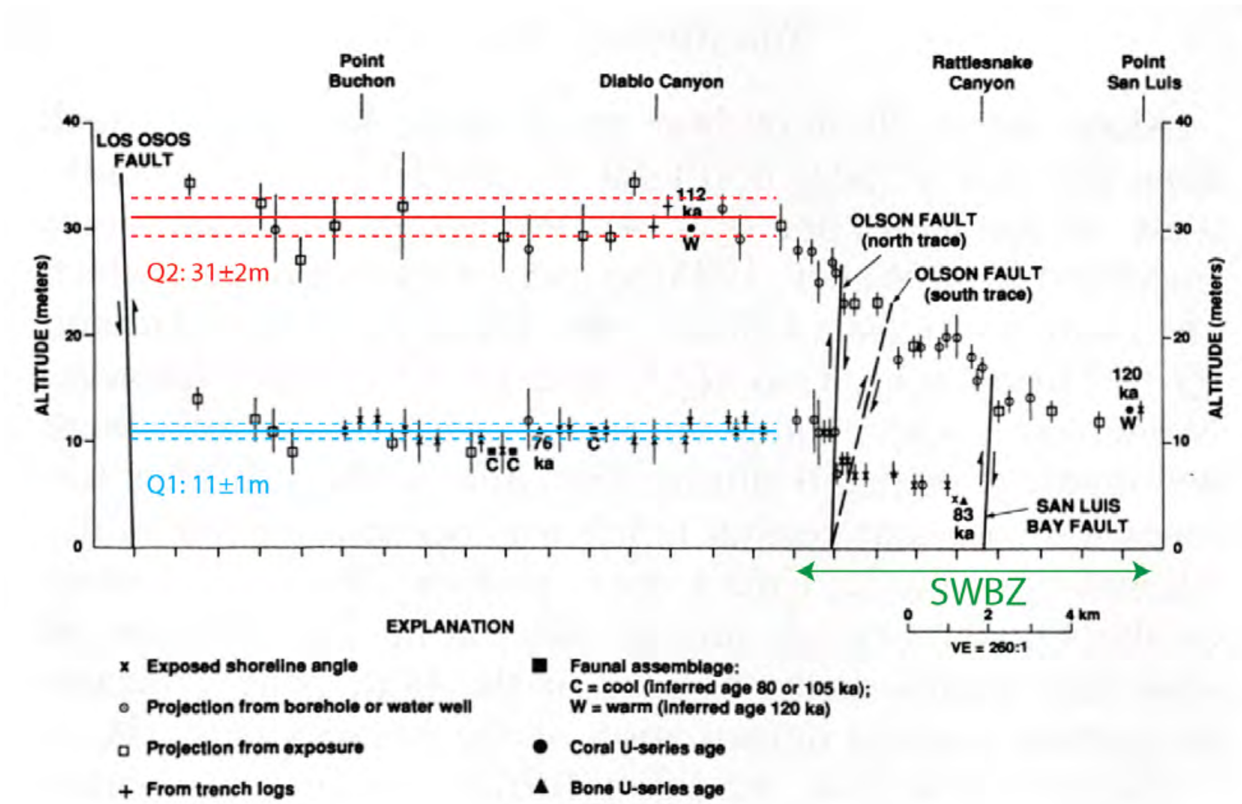

Figure 2.2 Marine terrace elevations plotted as a function of shoreline distance southward and eastward from the Los Osos trend. Block-like uplift of Irish Hills indicated from uniform elevations of Q1 and Q2 terraces north of the SWBZ. Note that the shoreline crosses the SWBZ at a low angle, exaggerating the width of the zone of tilting. [Source: Lettis & Hanson (1992), fig. 3, annotated in color.]

f. This high rate of permanent straining implies a high rate of faulting and of earthquakes, even if the relevant thrust fault traces are not always exposed.

We do not agree that a strain-rate estimate based on cumulative tilting and folding over the past 5 Ma can be used to argue for a high rate of reverse-faulting at present, given that a concrete shorter-term estimate of strain rate exists from marine-terrace uplift data. We agree that active reverse-fault traces are not always exposed. This is indeed the case for the SWBZ, which is associated with a ~2 km-wide zone of tilting down to the south with emergent faults (e.g., San Luis Bay fault at Avila Beach, Los Berros fault offshore) and areas where faults may not be emergent (i.e., the inferred Olson Hill fault, crossing the shoreline approximately 4 km east of the plant site).

g. Rigid-body uplift would not produce crustal thickening. Therefore, if the Irish Hills were a rigid block, they would have a positive isostatic gravity anomaly. However, gravity data show a negative isostatic gravity anomaly, indicating more than simple Airy compensation by crustal roots (more than the typical Airy ratio of 6:1).

Because uplift occurs via slip on one or more dipping faults, it does indeed produce a crustal thickening. This mechanism builds the structure and topography of the range, which has an average elevation of 230 meters above sea level. The net loading rate of the crust is proportional to the rate of surface uplift, which depends on the rate of rock uplift minus the rate of rock removal via erosion and may be zero if the rate of erosion is equal to the rate of rock uplift.

The argument that the crustal thickening rate is underestimated due to isostatic compensation and formation of crustal root is valid only if the Airy compensation mechanism applies to deformation on the horizontal dimensions of the Irish Hills, which are about 15 km wide and 25 km long. A more realistic model is regional compensation, where non-isostatic loads are supported by the flexural rigidity of the lithosphere; this model is parameterized by an elastic plate thickness, which is about 10 km for the Irish Hills (see §3.1). The characteristic bending wavelength for a 10-km elastic plate thickness is about 200 km. For loads with horizontal dimension much greater than this wavelength, the isostatic response corresponds to the Airy model (complete local compensation); for loads of much smaller dimension, the response corresponds to the Bouguer model (no compensation). Owing to the small dimensions of the Irish Hills, the flexural response of the Irish Hills is given by the Bouguer limit, not the Airy limit assumed by Dr. Bird (Figure 3.1).

h. The Irish Hills are being deformed by numerous unmapped and/or blind thrust faults in addition to the two thrust faults modeled by PG&E.

There may be additional active thrust faults that underlie the Irish Hills, but slip on these faults, if significant, should produce an uplift signal in the elevation of marine terraces fringing the range. The marine-terrace record of uplift over the past 124.0 ± 2.5 kyr shows that deformation evident as tilting is concentrated along the Los Osos trend and a suite of faults that make up the SWBZ (Figure 2.2). There are multiple permissible representations of the geometry of these faults at depth, including solutions with multiple strands (see §3.3), but the division of fault slip across multiple strands does not substantively change the net level of hazard.

i. One prominent possibility is the Inferred Coastline thrust fault passing offshore DCPP along the southwest coast of the Irish Hills and dipping under the plant.

The SRT finds that the location of the Inferred Coastline thrust fault corresponds to the SWBZ of the PG&E SSC Southwest-Vergent model. Though the model trace of the SWBZ lies approximately 2 km south of the Inferred Coastline Thrust, both would include DCPP within the near-field zone of strongest shaking.

j. The inferred location of this fault trace is based on:

1. The southwestern front of the Irish Hills is a topographic scarp with a smooth arcuate shape, mirroring the slightly-lower scarp on the northeast which has been formed by slip on the Los Osos thrust fault.

   This topographic scarp broadly corresponds to the SWBZ, and it also corresponds to outcrops of northward-tilted, erosion resistant volcanic rocks of the Obispo formation. The shoreline position is modified by intense shoreline retreat, estimated at ~1 cm/yr from the width of the Holocene wave-cut platform (PG&E 2011). The southwestern front of the Irish Hills is thus both structurally and erosionally controlled.

2. The documented uplift of marine terraces on the northeast side, relative to the continental shelf.

   Mapping of offshore submerged marine platforms indicates that the zone of higher uplift includes the offshore Islay Shelf, west of the Irish Hills, and areas directly south of the DCPP (PG&E, 2011). The zone of southward tilting, corresponding to the SWBZ diverges from the shoreline east of the DCPP and appears to cross the trace of the Shoreline Fault. This information suggests that the Shoreline fault is deformed by distributed deformation within the up-dip projection of the SWBZ.

3. Intense deformation of Miocene rocks in the plant area, which could be due to a forced fold over a blind thrust fault tip.

   Deformation of Miocene strata in the vicinity of the plant area is characteristic of much of the Irish Hills, with small-scale intense folding due to bedding-parallel shear, superposed on map-scale folding of the Pismo Syncline and forced folds over reactivated normal faults (PG&E, 2014a). Thorough investigations prior to construction of DCPP did not encounter evidence for active faulting at the plant site (summarized in PG&E, 2014d).

4. The tectonic implausibility of the San Luis Bay thrust fault simply terminating (just south of DCPP) without a connection to the Hosgri fault. (Actually, PG&E did suggest that the San Luis Bay thrust fault may terminate by merging with the Shoreline fault, but the slip rate of the Shoreline is so low that this is not plausible.)

   The San Luis Bay fault is one member of a set of faults that make up the SWBZ. The SRT agrees that a solution terminating the SWBZ at the Shoreline fault may be tectonically implausible. The SSC Southwest-Vergent model instead continues the SWBZ across the trace of the Shoreline fault to terminate at the Hosgri fault (PG&E, 2015). This solution is consistent with the pattern of uplift from marine abrasion platforms mapped onshore and offshore (PG&E, 2011). At the level in the crust where the SWBZ crosses the Shoreline fault, the pattern of deformation is diffuse and expressed as a network of discontinuous reverse fault strands associated with a ~2 km-wide zone of southward tilting. Individual fault strands do terminate at the Shoreline fault, such as, for example, the mapped trace of San Luis Bay fault near the coastline and the Los Berros thrust further offshore (PG&E, 2014b), but the zone of southward tilting continues west of the Shoreline fault (PG&E, 2011).

k. The crustal "basement" under the folded sedimentary rocks of the Irish Hills is mainly Franciscan Complex, which contains numerous Cretaceous-Paleogene thrust faults available for reactivation. Slip on those thrust faults would not reach the surface because such slip would encounter and fold the layered Neogene sedimentary rocks of the Pismo syncline.

We agree that the basement of Franciscan Complex is structurally complex and likely hosts faults inherited from pre-Cenozoic tectonism. We also agree that fault slip within the basement may be expressed as folding of sedimentary cover strata.

l. Thus, there are an unknown number of "blind" thrust faults active, such as those that produce devastating earthquakes under the Zagros Mountains of Iran, or in Nepal.

Blind thrust fault activity, if significant, should produce a measurable signal as folding of youthful markers such as the extensive marine terraces fringing the Irish Hills (Figure 2.2). Such folding is found along the Los Osos trend, in the north, and in the vicinity of the SWBZ, in the south.

2.2.2. "Active thrust faults may dip at any angle."

a. PG&E assumed active thrust faults may dip at any angle.

b. PG&E assigned alternative model dips of 30°, 50°, and 80° for the Los Osos thrust fault, with a combined weight of 70% to the dips of 50° to 80° in their logic-tree. They also assigned alternative dips of 45° to 75° for the San Luis Bay thrust fault.

Point (b) is an accurate statement of the dip range of reverse faults considered in the SSC24 model but point (a) is an incorrect generalization.

c. Mohr-Coulomb friction theory shows that thrusts never form at dips steeper than 45°, and most commonly dip at ~25° for rock friction coefficient of 0.85.

Here Dr. Bird appeals to a well-established theory of faulting based on the concept of Mohr-Coulomb friction, according to which the shear stress needed for fault sliding is proportional to the normal stress on the fault. Byerlee (1978) showed that the coefficient of proportionality, called the internal friction, lies in the narrow range 0.60-0.85 for most (though not all) rock types. In a compressive stress regime, where the greatest principal stress is horizontal and least principal stress is vertical, the theory predicts that the dip angle of a new fault is a simple function of the internal friction (§3.2). For Byerlee's range of internal friction, new faults should be thrusts with dip angles of 25º to 30º. The Mohr-Coulomb failure criterion for fault initiation assumes the strength of the rock mass is homogeneous and isotropic. Those conditions do not apply to active fault systems within the Los Osos domain, where most of the slip occurs on preexisting fault structures (§3.2).

d. Dips of 50º or 80º are mechanically impossible; such faults would not slip under the present horizontal compressive stress regime. Instead, some new thrust fault would form with dip ~25º.

This statement is mechanically incorrect because it presumes that the cohesive strength, static friction, and pore-pressure conditions on existing reverse faults are the same as those in the surrounding rocks. Geological and geophysical data commonly indicate the presence of high fluid pressures and weak zones of gouge in many exhumed and active faults; both act to reduce the overall strength of faults. Dr. Bird's statement is also contradicted by the observations of active high-angle reverse faulting in central and southern California and in many fault systems worldwide (§3.2).

e. Seismic potency rate varies as $1/\sin^2$(dip) when throw-rate is held constant (as in the SSC15 and SSC24 studies, where it is fixed at the marine terrace uplift rate).

This statement is true. Lowering fault dip will increase the horizontal shortening rate required to produce the observed marine-terrace uplift, and it will increase the down-dip extent of faulting within the seismogenic zone (assuming constant dip). Both factors depend on 1/sin(dip), and, when multiplied together, yield a $1/\sin^2$(dip) dependence of seismic potency.

f. Compared to reasonable estimates (obtained with dip of 25º), an assignment of 50º dip reduces seismic potency rate by a factor of 3.3. An assignment of 80º dip reduces seismic potency rate by factor of 5.4.

These estimates are correct for comparison of the SSC modeled range of fault dip with a 25° dipping thrust fault extending to the same depth. However, outcrop information, seismic imaging, and structural relationships with tilted hangingwall strata all indicate that the mean dip of the SWBZ is 38º ± 3° (§3.3). Compared to a 50° reverse fault, a 38° thrust fault would increase the potency rate by a factor of 1.5, and compared with a 80° reverse fault, the increase in potency rate would be a factor of 2.6.

g. Thus, PG&E underestimated seismic potency of these two thrusts (the only ones they modeled) by large factors.

Lower dip values increase slip rate and fault area and thus increase the potency rate. However, a 25° dip is inconsistent with the structure of the Irish Hills, and a more plausible 38 ± 3° dip yields a lesser amount of potency rate increase, as described above.

2.2.3. "Geologic structures older than ~0.33 Ma are irrelevant to seismic hazard estimation."

a. PG&E assumed that geologic structures older than ~0.33 Ma are irrelevant to seismic hazard estimation.

This statement is not accurate. The PG&E seismic source characterization effort (PG&E, 2014a,b,c) includes extensive mapping of onshore and offshore geology. This mapping contributes to understanding the locations of active faults identified at the Los Osos trend in the north and the SWBZ in the south. The mapping also identifies a number of faults that deform Miocene and Pliocene strata (older than 2.6 Ma) internal to the Irish Hills. The marine terrace record provides a key test for activity of these internal faults. Because there is no deformation evident where these faults project beneath the adjacent marine terraces, it is reasonable to assess them to be inactive (PG&E, 2014a). The distributed source model utilized by PG&E, which contains 30% thrust sources, provides a mechanism to account for the possibility of slip on these faults.

The geological structure of the Irish Hills could be used to more effect in modeling the geometry of the SWBZ at depth. As shown in the fault system analysis of §3.3, the structural model presented by PG&E (2014a, 2015) does not fully account for folding of the Pismo Syncline.

b. PG&E based the throw-rates of the San Luis Bay thrust fault and the Los Osos thrust fault on vertical offsets of marine & fluvial terraces with Upper Pleistocene ages, typically ~0.12 Ma.

This statement is correct.

c. PG&E never attempted to model the uplift and folding of sedimentary rocks in the Irish Hills which occurred since 5 Ma.

The 2014 geological and geophysical studies (PG&E, 2014a,b,c) includes a geometric model of faulting of the Irish Hills. This model, however, does not kinematically reproduce observed folding of the Irish Hills since 5.1 ± 0.4 Ma (§3.3). We recommend the development of an improved structural model (see §4).

d. A detailed statistical analysis of geologic constraints on fault offset rates in the western United States by Bird (2007) found that the probability of "inapplicability" of a dated offset feature to neotectonics (defined in that paper is equally low for all offset features up to 3 Ma (late Pliocene) in age, and almost as low for features of 5-6 Ma (Miocene/Pliocene boundary, or the time at which the Irish Hills began to form). Furthermore, that study concluded that a single offset feature is very rarely enough to make the fault offset rate "well-constrained;" instead, 4 offset features are needed to achieve a 50%-chance that the rate is "well-constrained," and 7 offset features are needed to guarantee it.

These arguments are a generalization from evidence of varying quality on numerous faults throughout the western United States. For the specific case of the Irish Hills, the SRT and Dr. Bird agree that the multiplicity and high quality of the marine-terrace uplift data qualify these data as the strongest constraint on the present-day rate of compressive deformation.

e. PG&E was negligent and unprofessional in failing to consider additional geologic constraints from older offset features, such as the once-planar Obispo Formation beds. PG&E should have created one or more structure models showing how this formation (and overlying sedimentary rocks) came to be bent into the present Pismo syncline and other folds in the center of the Irish Hills. All the structures in the Irish Hills, which formed since 5 Ma, should have been studied and modeled to provide geologic constraints on the rates of thrust-faulting. It is strikingly negligent that they never considered or attempted this.

We recommend the development of a structural model that is kinematically consistent with folding of the Irish Hills and the pattern marine-terrace uplift (§4). Such a model would be a valuable addition to the already extensive SSC effort. The long-term rate of deformation needed to produce folding may not match the shorter-term rate evident from the marine terrace data, in which case the marine-terrace constraint should take precedence.

2.2.4. "GPS geodetic velocities are not useful for site-specific seismic hazard estimation."

a. PG&E assumes that GPS geodetic velocities are not useful for site-specific seismic hazard estimation.

This statement is an overgeneralization. PG&E states, "Whereas geodesy-based model slip rates are interpreted to be unreliable for use as direct inputs in the SSC model for DCPP, they are useful for comparison and to document whether there are large differences between results" (SSC24, p. 116). For example, PG&E performed a comparison of slip-rate estimates from four deformation models prepared for the 2023 National Seismic Hazard Model (SSC24, Table 5-11) and found overall compatibility with the SSC slip rates. A similar comparison was made on previous models in the SSC15 (see SSC15, chapters 8 and 13). PG&E used GPS velocities to test their strike-slip rate range on the Hosgri fault (SSC24, section 5.2.1.2, p. 47), to provide estimates of principal strain axes derived from inversion of GPS velocities (SSC15, fig. 5-10), and evaluated 1D profiles through GPS velocities (SSC15, fig. 5-13). The details of PG&E's analysis and review of geodetic data are provided in sections 4.3.2.5 and 5.1.6 of the SSC15 report.

b. PG&E operated a GPS receiver at DCPP, and SSC15 reported the shortening direction across the Irish Hills as ~N15^{o}E but did not report the shortening rate. The SSC24 update added no new geodetic information, even though an additional 9 years of data should have greatly reduced all uncertainties!

It is true that PG&E reported shortening directions based on inversions of GPS data but did not report the rates (see SSC15, fig. 5-10 and section 5.1.6). It is also true that newer geodetic datasets have less uncertainty than the GPS data reviewed in the SSC15 (i.e., DeMets et al., 2014; Murray-Moraleda et al., 2011). For example, the east and north standard deviations of the DCAN velocity vector are 1.97 and 1.88 mm/yr, respectively, for the Murray-Moraleda et al. (2011) dataset and 0.25 and 0.23 mm/yr, respectively, for the Zeng (2022) dataset—an eightfold reduction of uncertainty.

As Dr. Bird suggests, recent advances in strain rate inversion methods (e.g., Shen et al., 2015; Maurer & Materna, 2023) and the continual accumulation of GPS observations make the production of regional strain rate maps worthwhile. Strain-rate maps inverted from the Zeng (2022) GPS dataset are presented in §3.4. The profile analysis and strain-rate maps are consistent with deformation of the greater Irish Hills region characterized by SAF-parallel shear and SAF-normal contraction. In this transpressional regime, the SAF-parallel motions are several times larger than SAF-normal contraction rates.

c. When questioned on this point at a recent DCISC meeting, the PG&E representative explained that GPS velocity profiles cannot be used to measure fault heave rates unless the profile of GPS stations extends far from the fault on both sides, and that the coastline near DCPP makes this impossible.

GPS velocities can be used even if stations are only available on one side of a fault. For example, onshore GPS is widely used to study offshore subduction zones. Geodetically measured motions can be combined with computational models of faulting to help interpret the data and estimate heave rates, even if the GPS station network does not span both sides of a fault. We have created several 3D simplified kinematic models of the SWBZ with a range of subsurface geometries to calculate strain rates and show that the main zones of strain accumulation should be onshore (see §3.4.6).

d. Seismicity has been successfully forecast using only GPS data (onshore) and plate-tectonic models (offshore), both in southern California and globally.

Bird & Kreemer (2015) applied the SHIFT method to the Global Strain Rate Map (version 2.1) and global seismicity observed through 2004 to obtain global forecasts of shallow-focus seismicity, which they tested against seismicity cataloged from 2005 to 2012. The forecasting ensemble was successful in the sense that, in pseudo-prospective testing, it "performed about as well as one, mature smoothed-seismicity forecast" (that of Kagan & Jackson, 2014). Bird & Kreemer (2015, p.162) were modest in their judgment of its qualifications for PSHA: "Consequently, we do not advocate our tectonic forecast as a replacement for smoothed-seismicity methods of forecasting seismicity, but rather as a supplement." The SRT agrees with this evaluation.

e. Therefore, GPS data are very useful. Any deformation model used in SSC should fit GPS strain-rate constraints (within their uncertainties).

PG&E did use geodetic data in a variety of ways to assess the validity of the SSC15 and SSC24 models (§2.2.4a). The SRT agrees and recommends that PG&E develop 3D kinematic and mechanical models of the entire regional fault system deforming at the SSC24 rates to compare directly with the geodetically observed deformation (§2.2.4b).

f. The problem of unavailable GPS velocities offshore is less serious in the case of thrust faults that dip away from the coast; theoretical models of dislocation patches in elastic half-spaces show that most of the interseismic strain occurs above the hanging wall, which in this case means on-land.

This statement is accurate. We have developed three simplified kinematic dislocation models of the SWBZ to illustrate and quantify this point (see §3.4.6).

g. Even if a GPS velocity profile across the Irish Hills does not record all of the interseismic heave rate, it still provides a useful lower limit on the rate of crustal shortening.

GPS observations can yield both upper and lower limits on the rates of land deformation. The geodetic analysis of §3.4 provides several useful products: velocity profiles across the greater Irish Hills region, regional strain-rate maps, and the results of forward-modeling the strain accumulation due to hypothetical reverse-slip faulting. A summary of GPS results is provided in Tables 3.2-3.4.

h. Models of neotectonic deformation, informed and guided by GPS velocity data, should be used in the estimation of seismic hazard.

We agree that model-informed analyses of the GPS data could provide integral constraints on the deformation useful in the improvement of the DCPP SSC. The geodetic analysis in §3.4, which corrects the velocity data for interseismic deformation on the San Andreas and other well-constrained, fast-slipping faults, is a start towards this goal. The next step is the development of 3D kinematic and mechanical models of the SSC fault sources that can be compared to the integral constraints from GPS.

i. Shen & Bird's (2022) preferred NeoKinema model shows long-term-average convergence of crustal blocks on both sides of the Irish Hills/San Luis Range region at velocities of ~1 mm/yr, for a total of ~2 mm/yr of local horizontal convergence rate.

In §3.4, the SRT concludes that the Zeng (2022) GPS dataset does not support the high convergence rates (~2 mm/yr) inferred by Dr. Bird. Shen & Bird (2022) use the NSHM fault geometry as input to their calculations. This geometry differs from the SSC fault model; hence, the Shen & Bird model is not appropriate for direct use in the SSC.

Looking forward, the SRT recommends that PG&E adopt the NSHM methodology of Field et al. (2023), which uses a suite of deformation models (including NeoKinema) driven by the same inputs, as a way to test the slip rate and fault geometry inputs to hazard models. Because modeling uncertainties remain poorly understood, any single estimate should be compared to other estimates.

2.3. Estimating the Total Rate of Thrust Faulting under the Irish Hills

a. The neotectonic uplift rate of the Irish Hills has been determined by PG&E to be approximately 0.2 mm/year, based on topography and ages of uplifted marine terraces compared to a global sea-level history. This is basic geologic data, and we are willing to stipulate that this uplift rate is approximately correct.

The Irish Hills uplift rate is the most important observational constraint on the SSC rates of deformation, which motivated the SRT to scrutinize its value and uncertainty. Glacio-isostatic modeling by Simms et al. (2016) predicts 13.0 ± 3 m (95% confidence) sea-level highstand elevation for the marine isotope stage (MIS) 5e Q2 terrace, rather than the 6.0 ± 3 m (95% confidence) global eustatic sea level originally used in the study by Hanson et al. (1992). This higher sea-level reference elevation reduces the predicted rate of uplift of the Irish Hills from 0.21 mm/yr to 0.15 mm/yr. We weight these two estimates equally, obtaining an uplift rate of 0.18 ± 0.3 mm/yr (§3.3).

We also considered recently presented results from IRSL (Infrared Stimulated Luminescence) re-dating of marine terraces at Cayucos that suggest correlation to the MIS 3 sea-level highstand rather than MIS 5 (Rivera et al., 2025). If the lowest marine terraces fringing the Irish Hills were to correlate to MIS 3 rather than MIS 5, the uplift rate would increase to ~1 mm/yr. We deem the IRSL results as unreliable, however, for three reasons. First, correlation to the cold-water MIS 3 highstand conflicts with cool- and warm-water faunal characteristics of marine fossils collected from the terraces (Hanson et al., 1992). Second, U-series dating of solitary corals supports the MIS 5 age assignment (Hanson et al., 1992; Hanson and Lettis, 1994). Though the U-series dates cited by these authors were measured using alpha-counting techniques that require multiple corals to produce a measurable signal (Muhs et al., 2017), single-coral dates measured using thermal ionization mass spectrometry also support the MIS age assignments at Cayucos (Stein et al., 1991) and the Irish Hills (D. Muhs, personal communication). Third, the natural IRSL signal may be affected by anomalous fading over time, reducing the apparent age.

b. However, these throw rates (vertical offset rates) for the bounding Los Osos and San Luis Bay thrust faults are compatible with much higher slip-rates if the dips of these faults are shallow.

We agree that lower fault dip requires a higher slip rate to produce the same uplift rate.

c. Also, thrust faulting on additional unmapped blind thrusts (e.g., Inferred Coastline thrust, and other unknown thrust faults within the Franciscan Complex basement) makes additional contributions to hazard.

There are multiple permissible representations of the geometry of faulting at depth beneath the Irish Hills, including solutions with multiple fault strands. We note that the SWBZ encompasses multiple individual fault strands distributed across an approximately 2 km-wide zone of southward tilting (see §3.3). The division of fault slip across multiple faults does not substantively change the net level of hazard. Indeed, adding faults may decrease the hazard, depending on how M_{max} is handled in the PSHA.

d. There are three ways to estimate the total rate of thrust fault slip in the Irish Hills without necessarily knowing the exact positions of each active fault plane.

2.3.1. Method #1: Isostatic

a. The neotectonic uplift rate of the whole Irish Hills region is uniform at 0.2 mm/yr.

We apply a rate 0.18 ± 0.03 mm/yr, based on the elevations of the Q2 marine terrace compiled by Lettis & Hanson (1992) (Figure 2.2). The uplift rate declines to zero or negative values (subsidence) to the north, across the Los Osos trend (Lettis and Hall, 1994). The uplift rate also declines to the south, across a 2 km-wide zone of tilting associated with the SWBZ (Hanson & Lettis, 1994; Lettis et al., 1994; PG&E, 2014a) (Figure 2.2).

b. However, active thrust faulting must explain not only this increase in topography, but also an increase in crustal thickness that is much greater. If a hilly region (like the Irish Hills) has extra mass above sea level relative to adjacent terranes, it must have a compensating mass-deficiency at depth. The most common finding is that elevated regions have "crustal roots," meaning unusually thick crust beneath them. This satisfies isostasy because all crustal rocks are less dense than all mantle rocks.

These descriptions apply only to Airy isostasy in which surface mass loads are compensated by variations in Moho depth. The Airy model is not valid in this situation (§3.1).

c. While there are alternative models (*e.g.*, Pratt isostasy in which variations in mantle lithosphere are important), simple Airy isostasy balances all vertical columns at the depth of the (deepest) Moho.

The alternative model that best agrees with observations is regional compensation, described in §3.1, where non-isostatic loads are supported by the flexural rigidity of the lithosphere parameterized by an elastic plate thickness. The elastic plate thickness in this region is about 10 km, which implies a characteristic bending wavelength that is large (~200 km) compared to the horizontal dimensions of the Irish Hills (15-25 km) (Figure 3.1). Therefore, the flexural response of the Irish Hills is approximated by the Bouguer (thick plate) limit, not the Airy (thin plate) limit assumed by Dr. Bird. The gravity data for central California have been successfully modeled in the Bouguer limit by Langenheim et al. (2012), who show that the gravity anomalies can be explained by density contrasts between Neogene sedimentary rocks and denser Mesozoic basement rocks (Figure 3.2).

d. The isostatic gravity anomaly will be near zero if Airy isostasy applies.

This is true by definition; however, Airy isostasy does not apply on the scale of the Irish Hills.

e. Isostatic gravity anomalies in the western US can be loosely described as 0 ± 50 mGal.

Local compensation by a combination of the Airy and Pratt mechanisms is a good approximation in California on scales of hundreds of kilometers (e.g., Eymold & Jordan, 2018). However, it is a poor approximation when applied to surface loads as small as the Irish Hills (§3.1).

f. A positive value indicates “undercompensation” (deficient crustal roots) and a negative value indicates “overcompensation” (crustal roots thicker than expected).

Dr. Bird interprets the negative isostatic gravity anomaly of the Pismo Syncline as a signal of overcompensation by a deforming and thickening crustal root. Under his interpretation, overcompensation implies a greater rate of faulting than pure Airy compensation. However, the data show that the surface loads in and around the Irish Hills are supported by small regional plate flexures rather than large local variations in Moho depth (§3.1).

g. A simple Airy isostasy implies that the ratio of crustal thickening to topographic rise is about 6. Therefore, a simple isostatic model for the total rate of thrust-fault slip under the Irish Hills is at least: (0.2 mm/yr uplift) × 6 / sin(25º) = 2.8 mm/yr

For small areas such as the Irish Hills, the response to surface loading is Bouguer, not Airy (§3.1). Hence, the factor of six in the above equation reduces to unity, and the slip rate becomes:

(0.2 mm/yr)/sin(25º) = 0.47 mm/yr.

This rate is further reduced if the average SWBZ dip of 38º is used:

(0.2 mm/yr)/sin(38º) = 0.32 mm/yr.

The best estimate of this slip rate derived from the fault system analysis of §3.3 is 0.29 ± 0.07 mm/yr, based on an uplift rate of 0.18 ± 0.03 mm/yr.

h. If this crustal thickening is occurring on a single thrust fault of dip 25°, then its rate of slip should be 2.8 mm/yr. If the crustal thickening is driven by two oppositely-vergent and overlapping thrust faults, each should have a slip-rate of ~1.4 mm/yr.

Geologic mapping (PG&E, 2014a) shows that the structure of the Irish Hills is asymmetrical, with a larger extent of structural tilting of the south limb of the Pismo Syncline, and little to no fault throw associated with the Los Osos trend. The SSC Outward-Vergent model estimates slip rates of both faults based on the rate of uplift determined from marine-terrace elevations. Alternatively, the Los Osos trend acts as a hingeline up-dip of a bend in the SWBZ such that uplift across this trend would not be attributed to an independent source. We derive slip rates for the SWBZ based on a kinematically controlled structural model (§3.3), obtaining 0.5 ± 0.1 mm/yr over 5.1 ± 0.4 Ma, and 0.29 ± 0.7 mm/yr over 124 ± 2.5 ka. The latter rate overlaps the 0.06 to 0.27 mm/yr range (median 0.17 mm/yr) from the SSC24 for the SWBZ derived from the same marine-terrace datum. Our mean estimate is somewhat higher because we model a 38 ± 3° fault dip, which is less than the range of 45º-75º considered in SSC15 and SSC24.

i. More complex models with more thrust faults can be devised, but the implication for total strain and seismicity due to thrust-faulting will remain unchanged.

It is correct that more complex models may be devised to accommodate the rate of convergence across the Irish Hills, so long as these models honor the rate and pattern of uplift evident from the marine-terrace record. Adding more faults may decrease the hazard, however, depending on how M_{max} is handled.

2.3.2. Method #2: Thrust Fault Heave Rate

a. I provide one example: Throw of the Obispo Formation at the San Luis Bay-Inferred Coastline thrust fault is 1.6-2.2 km since 5 Ma, implying throw-rate of 0.32-0.44 mm/yr, and fault slip rate of 0.76-1.04 mm/yr.

The cross-section in Dr. Bird's report shows the SWBZ with a dip of 29° (Figure 2.3), which yields a lower slip rate (0.66-0.91 mm/yr) than Bird's stated estimate based on a stated dip of 25º (0.76-1.04 mm/yr).

Thrust offset is one possible mechanism to explain the offset of the Obispo formation across the SWBZ. There are other possible mechanisms to produce the offset of the Obispo formation, including normal faulting during Miocene extension and lateral juxtaposition of these outcrops via strike-slip along the Shoreline fault. Dr. Bird projects the Obispo Formation southward with uniform dip but overlooks geologic evidence that the Obispo formation is truncated by the San Miguelito fault, a north dipping normal fault within the Irish Hills that was later reactivated with reverse motion (PG&E, 2014a; Weigers, 2021). Thus, the hypothesized offset could also be accomplished, at least in part, by projection of the offshore outcrops of the Obispo formation northward to truncate against the San Miguelito fault. In our fault system analysis (§3.3), we find that the 1.8 ± 0.2 km length of the south limb of the Pismo Syncline provides a robust measure of slip within a kinematically constrained fault model. Using this approach and adding slip that did not contribute to tilting this fold limb, we estimate total slip on the SWBZ of 2.6 ± 0.3 km, which yields a mean slip rate of 0.5 ± 0.1 mm/yr since the onset of folding at 5.1 ± 0.4 Ma.

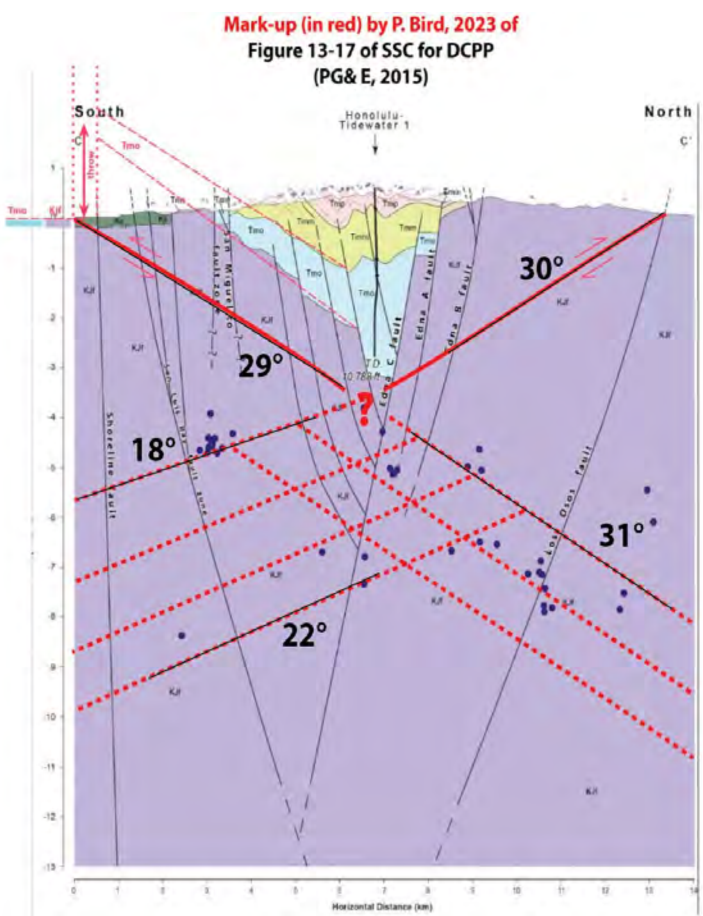

Figure 2.3. Cross-section through the Irish Hills (PG&E, 2015, fig. 13-17) annotated by Bird (fig. 7 of B6) with hypothetical thrust faults (red lines). Bird states that the solid red fault surfaces dip at 25º, but the fault dips measured directly from the figure (black numbers) are 29º and 30°.

b. If thrusting in the Irish Hills has been symmetrical(?), then a minimum total thrust slip-rate by this method would be 1.52-2.08 mm/year.

The cross-section in Dr. Bird’s report shows nearly symmetrical thrust faults dipping 29° and 30°, corresponding to the SWBZ and Los Osos Fault (Figure 2.3). Geologic mapping (PG&E, 2014a; Weigers, 2021) shows that the structure of the Irish Hills is asymmetrical, with a larger extent of structural tilting of the south limb of the Pismo Syncline, and little to no fault throw associated with the Los Osos trend (see §3.3). We find a steeper, 40° dip to be more consistent with structural relationships in the hangingwall of the SWBZ. This dip also matches field observations that average 38° ± 3° (Table 3.1).

c. However, this estimate neglects any internal blind thrusts, so it is only a lower-limit estimate.

In our estimation, based on the strain estimates from PG&E (2014a), internal shortening across the north limb of the Pismo Syncline contributes 260 ± 15 m to the overall shortening across the Irish hills (§3.3). Most of the contraction across the Irish Hills is accommodated by thrusting on SWBZ, including slip on the San Miguelito fault that contributed to tilting of the south limb of the Pismo Syncline.

2.3.3. Method #3: GPS Geodetic Horizontal Shortening Rate

a. Shen & Bird's (2022) NeoKinema model produced estimates of ~2 mm/yr of long-term-average horizontal crustal shortening across the Irish Hills. Therefore, total thrust fault slip rate under the Irish Hills would be (~2 mm/year) / cos(25º) = ~2.2 mm/year.

The methods of Shen & Bird (2022) could potentially be used to create a model appropriate for consideration in a future SSC. The issue is that their model uses the NSHM fault geometry as input, which is significantly different from the SSC15 fault model. Therefore, estimates from the Shen & Bird (2022) model are not appropriate as input to the SSC. We also show that the strain rates implied by the proposed 2 mm/yr are two to five times larger than what strain-rate inversions of the Zeng (2022) GPS data indicate.

b. Another approach is to look directly at the GPS site velocities. This means looking at interseismic relative velocities, not the long-term-average velocities which are provided by modeling. I apply this approach to the geodetic dataset that was used as input to the 2023 update to the National Seismic Hazard Model.

We note that this is the Zeng (2022) GPS dataset used in the geodetic analysis of §3.4.

c. Using these raw GPS velocities, we see that station DCAN (Diablo Canyon) is converging at 0.4 mm/yr with respect to DAPK (Prefumo Cyn., mid-Irish Hills) and converging at 1.1 mm/yr with respect to CHOR (on Hwy 1, NNE of DCAN). Alternatively, site 2110 (slightly NNE of Point San Luis) is converging at 1.7 mm/yr with respect to DAPK (half-way across the Irish Hills), and converging at 2.4 mm/yr with respect to CHOR (across the full width of the Irish Hills). One way to summarize these results is to note that the average of the DCAN-CHOR interseismic shortening rate with the 2110-CHOR interseismic shortening rate is 1.8 mm/yr.

We were unable to reproduce these shortening estimates using the raw Zeng (2022) velocities. Relative to DCAN, station DAPK has a velocity of 0.77 mm/yr at an azimuth of 159°. Relative to station DCAN, CHOR has a velocity of 1.43 mm/yr at an azimuth of 158°. Relative to station 2110, DAPK has a velocity of 1.30 mm/yr at an azimuth of 175°. Given that these velocities are oriented at different azimuths, it is not appropriate to simply sum the velocities. A better alternative for using the GPS station velocities to constrain convergence rates is to first correct the velocities for the interseismic elastic deformation due to known faults peripheral to the greater Irish Hills region and then project the residual velocities onto profiles across the region, as described in §3.4.

d. Allowing for the bias that interseismic rates may underestimate near a coastline, these interseismic rates tend to support the long-term-average shortening rate of 2 mm/yr across the Irish Hills that the Shen & Bird (2022) NeoKinema model predicts.

If we take a conservative approach and apply this suggested convergence over the width of the Los Osos domain (20-25 km), a contractional rate of 2 mm/yr corresponds to a contractional strain rate of 80 to 100 nanostrain/yr. After correcting for strain accumulation on the San Andreas and Hosgri faults, we find that the regional deformation is dominated by apparently strike-slip deformation, most likely due to the strain accumulation from the Rinconada, East/West Huasna, and other regional dextral strike-slip faults (§3.4). Removing the SAF-parallel shear leaves only a small SAF-perpendicular contractional component. The uncertainties are large (± 10 nanostrain/yr), but the contractional strain rate averaged across the Irish Hills (20-40 nanostrain/yr) is significantly lower than Bird's estimate of 80 to 100 nanostrain/yr. Contraction normal to the SWBZ is more difficult to constrain as SAF-parallel shearing contaminates estimates of SWBZ normal shortening (see §3.4).

2.4. A Characteristic Thrust Earthquake

a. Each time a false assumption in the PG&E SSCs was removed, thrust-faulting activity (seismic potency rate) in the Irish Hills went up by a large factor. It is important to estimate how these factors combine, and how high seismic hazard (and seismic core damage frequency, SCDF) may be at DCPP. This could be done with a new SSC study and a new SPRA study, except that we cannot afford years of time and millions of dollars.

The SRT analysis does not support Dr. Bird's claim that the removal of each of four false assumptions increases the estimated seismic potency rate of thrust faulting beneath the Irish Hills above the SSC24 value (§4.1).

b. Instead, we will use a much simpler method to show that the lower limit on seismic hazard (and SCDF risk) due to thrust-faulting alone is much higher than the total hazard claimed by PG&E. We will do this by adopting a characteristic great thrust earthquake for this tectonic setting and then estimating its frequency in the Irish Hills.

The analog-event method used by Dr. Bird requires the identification of a well-documented historical earthquake suitable for serving as a characteristic thrust earthquake in the Irish Hills tectonic setting. A strong criterion for suitability is fault-system (geometric) compatibility: a candidate rupture should be representable as slip on an interconnected system of reverse faults, either known or postulated, with similar overall dimensions. The SRT agrees with Dr. Bird that the most likely candidate for hosting the largest reverse-slip earthquakes beneath the Irish Hills is the SWBZ and its possible reverse-faulting extensions.

c. In SSC and PSHA studies that include fault seismic sources with very incomplete information, it is traditional to assume a periodic characteristic earthquake model. While this is only an approximation of the chaotic earthquake dynamics in the real Earth, it has the advantage of allowing simple arithmetical conversions between the triad of basic parameters: slip per earthquake, long-term geologic slip-rate, and earthquake recurrence interval. For example, to compute the recurrence interval for large characteristic thrust-faulting earthquakes under the Irish Hills, it is sufficient to divide the mean coseismic slip in the characteristic earthquake by the long-term tectonic slip-rate of thrusts under the Irish Hills.

This method for estimating recurrence intervals, here called the 'maximal earthquake model', is an end-member of the characteristic earthquake model (see §3.5). The recurrence interval given by the maximal earthquake model is a lower bound, because the model does not account for the more frequent, smaller earthquakes that can contribute significantly to the slip budget. A more realistic model includes a Gutenberg-Richter (power-law) component of seismicity, which better approximates "the chaotic earthquake dynamics in the real Earth" (see §3.5).

d. The Noto Peninsula on the northwest coast of Japan is tectonically analogous to the Irish Hills:
    1. Both are elliptical blocks of crust now being uplifted from beneath shallow seas between two conjugate intraplate thrust faults.
    2. Both occur within crust that formed in a subduction setting, with significant input of arc-derived graywacke clastic sediments.
    3. Both experienced an extensional phase prior to the present compressional phase. The opening of the Sea of Japan was Miocene, preceding present AM-OK plate convergence. The future Irish Hills

region experienced a brief episode of crustal melting, volcanism, and uplift due to formation of a slab window after the 28 Ma disappearance of the Farallon plate at this latitude. In Late Miocene the region cooled and subsided, and remained tectonically quiet until 6-5 Ma.

4. Both include active thrust faults that were accidentally omitted from their respective national seismic hazard models because they are either blind or under water.

Points 1-3 are valid tectonic analogies, but there are also differences, as identified in responses to the Bird critique by Madugo & Kottke (2024), LCI (2024), and NRC (2025). The SRT summarizes six key differences in §3.5.5. Point 4 is not valid because reverse fault representations of the SWBZ are included in both the National Seismic Hazard Model (NSHM) and SSC24.

e. The primary difference is that horizontal convergence in the Noto Peninsula is faster (~10 mm/yr *vs.* ~2 mm/yr), allowing us a better opportunity to observe its seismicity in our brief historical datasets. Further discussion of these similarities and differences in Appendix B.

According to the earthquake recurrence models of §3.5, the factor-of-five faster rate implies that the Irish Hills recurrence interval for a maximal event should be five times longer than the Noto Peninsula recurrence interval.

f. On 1 January 2024, at 07:10 UTC, a very large earthquake occurred beneath the Noto Peninsula on the northwest coast of Ishikawa Prefecture, Japan. Its magnitude was 7.5 on the moment-magnitude scale used by USGS. This thrust-faulting shock achieved a maximum JMA seismic intensity of Shindo 7 and Modified Mercalli intensity of IX (Violent). These intensities are very high.

g. We learned 2 essential facts from this 2024.01.01 **M**7.5 earthquake:
   1. The finite-fault solution showed maximum slip of 3.7 m under the center of the Noto Peninsula, with a mean slip that I visually estimate as 2.0 m (or 2000 mm) within the seismogenic depth range, under the part of the fault trace that parallels the Noto Peninsula.
   2. Peak ground accelerations at 5 strong-motion seismometers were 1.0-2.3 g as far as 42 km from the rupture.

This characterization of the 2024 Noto Peninsula (Noto Hanto) earthquake (abbreviated Noto24) is correct, except that the average slip is now estimated to have been about 4 m (Xu et al., 2024), rather than 2 m. Noto24 was an unusual earthquake, characterized by high-stress-drop asperities (up to 40 MPa) and a very long rupture. Its along-strike rupture length (150 km) was 7 times larger than its down-dip width (21 km), which is outside the aspect-ratio range of interplate dip-slip events. Owing to its rupture length, Noto24 is not compatible with the SWBZ fault geometry, which is bounded along-strike by the Hosgri fault zone to the west and the Oceanic-West Huasna fault zone to the east (see §3.5).

2.5. Conclusion: Seismic Core Damage Frequency at DCPP

a. The SSC15 and SSC24 studies seriously underestimated the seismic hazard from thrust-faulting under the Irish Hills because they relied on 4 demonstrably false assumptions. Three independent analytic methods give values for the total slip-rate on all shallow-dipping thrust faults under the Irish Hills: 2.8 mm/yr, ~2.0 mm/yr, or 2.2 mm/yr.

The SRT's analysis does not support these high estimates of slip rate (see §4.2). The SRT's best estimate of the present-day slip rate on the SWBZ is 0.29 ± 0.07 mm/yr for a dip of $38 \pm 3°$ (§3.3).

b. Using the 2024.01.01 Noto Peninsula earthquake as a characteristic thrust earthquake (with its 2 m of mean slip) yields recurrence times for great thrust earthquakes under the Irish Hills of 715 years, 1000 years, or 910 years, respectively.

The mean slip of the Noto24 rupture is about 4 m, rather than 2 m (e.g., Xu et al., 2024). The SRT analysis of relative uplifts (§3.5) yields estimates of the recurrence interval for a Noto24-type event involving the Irish Hills that range from 8,300-16,700 yr (maximal earthquake model) to 16,700-33,300 yr (Gutenberg-Richter model). Dr. Bird's stated values (715-1,000 yr) are three times smaller than the several thousand years estimated for the Noto24 fault system (§3.5) and are thus inconsistent with the difference in convergence rates.

c. This raises the question of whether PGA of 1.0-2.3 g will cause seismic core damage (SCD) at Diablo Canyon Units 1 & 2? Answering this question quantitatively becomes technical and difficult, given that spectral accelerations critical to individual component failures are typically twice as large as PGA; that is, perhaps 2.0-4.6 g at vibration frequencies of 5-10 Hz for the Noto Peninsula earthquake analog.

d. The 2018 SPRA (PG&E, 2018) is the most recent available to me. Within this document, Table 5.4-4 (page 65) shows how PG&E's overall SCDF of 2.8×10-5 /yr was obtained. In principle, it should be possible to use this information to estimate the probability of SCD at each level of shaking. My interpretation of the table is that the probability of SCD is ~6% at 2 g, rising to ~73% at 3 g and to >98% at 4 g. The problem is that the acceleration levels quoted in this table are not clearly identified; are they PGAs or (more likely) spectral accelerations? The context in this SPRA report suggests that they are spectral accelerations: the introductory section "3.1.3 Seismic Hazard Analysis Results and Insights" only discusses 5 Hz spectral accelerations, and the primary graphs that it refers to ("Figure 3-1 -

Reference Rock Hazard by Source for 5 Hz Spectral Acceleration" and "Figure 3-4 - 5 Hz Control Point Mean and Fractiles Horizontal Hazard") are plots of 5 Hz spectral acceleration.

e. Therefore, my interpretation of this report is that a PGA event of 1.0 g would produce 5 Hz spectral accelerations of ~2 g, and incur ~6% chance of SCD. However, a PGA event of 1.5 g would produce 5 Hz spectral accelerations of ~3 g, and incur a ~73% chance of SCD. And the peak Noto-earthquake observation of PGA of 2.3 g would produce spectral accelerations of ~4.6 g, and incur >98% chance of SCD at DCPP.
f. It will probably be controversial exactly which of the Noto Peninsula seismograms give the median and worst-case forecasts of shaking at DCPP. The paragraph above shows that this is a critical point. Clearly these questions need to be resolved by independent experts, preferably in a revised SSC study followed by a revised SPRA study. In the meantime, for purposes of evaluating the acceptability of PG&E's two SSCs, it is sufficient to assume that the levels of shaking seen in the Noto Peninsula earthquake will cause seismic core damage at DCPP if and when they occur in the Irish Hills of California.
g. Assuming that such a great thrusting earthquake would cause seismic core damage at DCPP, its seismic core damage frequency (SCDF) is at least
h. 1.4×10-3 /yr, or 1.0×10-3 /yr, or 1.1×10-3 /year, respectively.
i. This is before the hazard contributions from strike-slip faults like the Hosgri and Shoreline are added.

Because the SRT members are not experts in seismic risks to nuclear power plants, the SCD issues raised by Dr. Bird in §2.5c-i are not evaluated in this report.

2.6. Appendix A: Missing Procedural Steps in the SSCs by PG&E (2015, 2024)

a. Another fundamental problem with PG&E's (2015, 2024) seismic risk analyses (besides logic guided by false assumptions) is the subjective (i.e., committee-based, not algorithm-based) creation of "fault geometry" models to support the 2015 and 2024 SSCs. These kinematically incomplete models also biased PG&E's (2018) SPRA.

All fault system representations are incomplete and uncertain and use both expert judgment and committee-based consensus (e.g., the NSHM fault geometry model used by Shen and Bird, 2022). The PG&E SSC considers two hypotheses to explain the origin of faulting responsible for uplift of the Irish Hills: northeast-southwest-oriented crustal shortening, and transpressional right-shear. The transpressional right-shear model favors the presence of steeply dipping, oblique-slip faults reactivated (inverted) from an earlier transtensional deformation phase. All of the SSC reverse-fault models are restricted in their down-dip dimension by the 10 to 15 km across-strike width of the Irish Hills. Our fault-system analysis (see §3.3) shows that a kinematically constrained fault model may extend to the north of the Irish Hills at depth via slip on a horizontal detachment linked to the SWBZ within the seismogenic upper crust.

b. Their fault geometry models do not meet basic scientific standards for objectivity and reliability because they are not geometrically self-consistent, nor are they consistent with GPS and regional stress directions.

Cross-section representations (PG&E, 2014a) of reverse faults beneath the Irish Hills meet the standard of geometric self-consistency, in that fault throw and bedding cut-off angles are consistent with inferred directions of fault slip, including inversion of normal faults with reverse slip. The faults strike perpendicular to the regional shortening direction, consistent with observed reverse slip and associated folding. The SSC fault representations are arguably not kinematically consistent with folding of the Pismo Syncline. The SRT notes, however, that fault-related fold theory permits a variety of interpretations within unlayered basement rocks (Narr & Suppe, 1994), such that steeply dipping, kinematically constrained fault models may be constructed similar to the geometric models presented in the SSC, in addition to the moderately dipping ramp-flat model presented in §3.3. The SRT recommends that kinematically constrained fault-related fold theory be applied to produce an updated set of fault representations (§4).

c. They did not take account of, or make use of, then-published and available scientific developments in:

1. Measurement of crustal motion by permanent and campaign Global Positioning System (GPS) receivers

PG&E did use the GPS data, as documented in §2.2.4e. The SRT agrees that additional geodetic data analysis is warranted, including the use of improved strain-rate inversion methods (e.g., Shen et al., 2016; Maurer & Materna, 2023) and the construction of a 3D kinematic and mechanical model to compare to the GPS velocities. The SRT's contributions to this analysis are described in §3.4.

2. Computer modeling (including kinematic finite-element models) of such data, in combination with geologic and stress data, to compute long-term crustal strain rates and fault slip rates; e.g., use of program NeoKinema (Bird, 2009).

The SRT recommends the creation of 3D kinematic and/or mechanical models of the SSC fault sources to be compared to the existing geodetic and geologic slip rate data (§4). We note that, because the sources of uncertainty in models are not yet fully understood (e.g., Johnson et al. 2024), careful analysis of a suite of capable models and sufficiently dense geodetic observations will be needed before geodetic-based models can be qualified for direct use in future versions of the SSC.

3. Recent initiatives in seismic hazard estimation which do not assume that a complete inventory of active faults is available, but instead compute the expected seismicity across the map area from crustal long-term (permanent, not elastic) strain rates and fault slip rates (if and where available) using a calibration of global shallow seismicity categorized by plate-tectonics (Bird & Kagan, 2004; Bird & Liu, 2007; Bird et al., 2009; Bird et al., 2010).

   Issues associated with the use of the SHIFT methodology are summarized in §2.2.4d. As Bird & Liu (2007) point out, "California continuum seismicity is small compared with fault seismicity." The SHIFT method uses Neokinema to determine inelastic strain rates and computes seismicity from that component. The calculation is compromised by the small scale of the Irish Hills and the overwhelming influence of the SAF and related strike-slip faults on the strain in the DCPP area (§3.4).

d. In particular, PG&E (2015; 2024) should have used the globally-calibrated strainrate-to-seismicity conversion to obtain the seismic moment rate for their Local Area Source component. By using a seismic moment based on microseismicity in a few quiet decades between seismic crises, they seriously underestimated it.

Loading of the San Andreas fault and its transition to the creeping section are the principal contributors to the strain rate across the Irish Hills (§3.4). Assessing strain rate that contributes to the Local Areal Source component requires correcting for San Andreas and other known sources, such as the Hosgri fault and the SWBZ. The results are highly uncertain given the underlying uncertainties associated with modeling these sources. The hazard contribution from the Local Areal Source Zone, as currently formulated, rivals that of SWBZ and Los Osos fault source models (Figure 2.1).

2.7. Appendix B: Dismissal of PG&E's Objection to the Noto Peninsula Earthquake Model

a. The principal subject of the LCI (2024) Report was the 2024.01.01 Noto Peninsula earthquake, and whether this could be accepted as a model characteristic thrust earthquake for the setting of the Irish Hills in California (as I have suggested). Here I will quote some of their concerns in italic type, followed by my responses. Points of agreement or common knowledge will not be included. For example, LCI agrees that the Noto Peninsula is an inverted fault-bounded basin that has been uplifted between oppositely-vergent thrust faults, and that the start of its compressional phase was 4-3 Ma, similar to the 5 Ma initiation of the Irish Hills.

The SRT agrees with the statements in the last sentence.

b. LCI Report: *"The San Luis-Pismo Block [in the Irish Hills] is interpreted to have been uplifted as a rigid block during the late Quaternary by reverse slip on both the Los Osos fault and Southwestern Boundary zone faults."*

Response: LCI acknowledges that this idea of a rigid block is copied from PG&E (2015). I have refuted it in previous sections of this report.

Dr. Bird's refutation is based on two assertions. (a) The folding which created the Pismo Syncline since 5.1 ± 0.4 Ma continues today. However, as discussed in §2.2.1, the strain-rate estimate based on cumulative tilting and folding since the early Pliocene is not consistent with the shorter-term estimate of strain rate from marine-terrace uplift data. (b) Rigid-body uplift would not produce the crustal thickening needed to maintain Airy isostatic compensation. However, as demonstrated in §3.1, Airy isostasy does not apply to the Irish Hills, where the compensation is regional.

c. LCI Report: *"The Q1 terrace [in the Irish Hills] is almost flat, with a relatively gentle shoreline slope, which along the southwestern coastline of the Irish Hills is locally steeper, possibly reflecting increased colluvial and/or alluvial cover (AMEC, 2011a)."*

Response: This increased slope could also be interpreted as due to continuing forced folding of the hanging-wall of the blind Inferred Coastline thrust (my term).

The phrase quoted from the LCI report describes the expression of the Q1 marine terrace in the landscape. Uplift and deformation are measured from the elevation of marine-terrace shoreline angle (Figure 2.2), not from the topographic surface of the terrace. The shoreline angle marks the innermost position of wave erosion against the paleo sea-cliff that forms close to the mean high tide. These elevations are surveyed from below the marine, colluvial, and alluvial terrace cover. The Q1 and Q2 shoreline angle elevations are uniform across most of the Irish Hills. These elevations decline due to folding and faulting associated with the SWBZ with steps located at the Olson fault and San Luis Bay fault (Hanson & Lettis, 1994).

d. LCI Report: *"Compared to the Noto Peninsula faults that are readily identifiable from their acute geomorphic expression on the seafloor, the relative lack of expression of the Irish Hills bounding faults indicates that despite exhaustive investigation from detailed topographic, bathymetric, geologic, and geophysical investigations onshore and offshore, these faults are not directly analogous to those generating uplift along the Noto Peninsula (sect. 4.2.1)."*

Response: This difference in fault-scarp expression is expected based on the fact that horizontal shortening in the Noto Peninsula is about 5× faster than in the Irish Hills (~10 mm/a vs. ~2 mm/a), whereas the initiation ages are similar (4-3 Ma vs. 5 Ma). The Noto Peninsula thrusts have slipped further, and are currently slipping faster, so they have more prominent scarps. This is not an important distinction.

This distinction is important because emergent thrust faulting at Dr. Bird's proposed ~2 mm/yr rate should produce prominent topographic scarps flanking the Irish Hills. A 25° dipping thrust fault slipping at 2 mm/y would produce a 100 meter-high scarp in the span of 120 kyr since formation of the Q2 marine terrace. Similarly, multiplying Dr. Bird's proposed 1.6 to 2.2 km of cumulative fault throw (Figure 2.3) by the ratio of 0.12 My / 5 My yields a scarp height of 38 to 53 m. No such dramatic scarps are evident onshore or offshore. The height of the Q2 marine terrace is only 18 to 25 meters above the elevation at which it was formed (Hanson et al., 1992; Simms et al., 2016), and marine abrasion platforms preserved offshore do not show evidence of appreciable subsidence (PG&E, 2011).

It is instructive to compare the SWBZ with the Casmalia Hills thrust fault, located approximately 25 km to the south. This fault exhibits uplift rates ranging from 0.9 to 2.6 mm/yr recorded as folding of the Orcutt Formation, an extensive non-marine deposit with age dating and stratigraphic correspondence to MIS 5e (MacGregor and Onderdonk, 2021). The base of the Orcutt formation is commonly uplifted over 200 meters, with up to 20° of tilt, over the blind thrust-tip of the Casmalia Hills fault. The Irish Hills and San Luis range uplift the comparably aged Q2 marine terrace and corresponding non-marine deposits inland but without the same degree of uplift and tilting. Uplift rate based on the Q2 marine terrace are an order of magnitude lower, 0.18 ± 0.03 mm/yr.

2.8. Statements from Other Documents of the Bird Critique

B6 summarizes almost all of the key points that Dr. Bird had made in his five earlier reports (B1-B5), but there are a few aspects of the Bird critique that were emphasized in those submissions but were not highlighted in B6. This section gives an annotated summary of four.

- SSC15 Local Areal Source Zone (from B1)

1. The Local Areal Source Zone is the second most important source of acceleration (after the Hosgri fault) in the critical part of the hazard recurrence curve around (1 g, 1E-4/year). This part of the source model is based on three errors, all of which combine to underestimate the hazard. First, PG&E estimated the long-term seismic moment rate of the Local Source Region by using moment rates from the instrumental seismic catalog, instead of moment rates from a tectonic deformation model. This

resulted in very low assigned slip-rates of 0.01~0.14 mm/a for the virtual thrust faults. But, because seismicity has a power-law frequency/magnitude distribution and is clustered on all scales in space and time, this method is known to have a high probability of yielding a serious underestimate.

This is a correct statement. Estimates of long-term seismicity rates from catalogs of short duration are often biased by the strong spatiotemporal clustering of seismicity.

2. Faulting in the Local Source Region was modeled as 70% strike-slip and 30% thrusting, but there is no geologic reason to expect anything but pure horizontally-compressional thrusting and folding within the Irish Hills.

The 1D profiles through GPS data in §3.4 indicate a transpressional environment. Even after removing deformation due to the San Andreas fault, we still estimate significantly more apparent residual strike-slip deformation compared to contraction. Moreover, the focal mechanisms of individual earthquakes, as well as composite mechanisms (SSC15 report, figs. 5-23 and 5-24; SSC24 report, fig. 5-27), display a mix of reverse and strike-slip events.

3. The maximum magnitude in the Local Source Region was arbitrarily set at 6.6~7.1; however, Bird & Kagan (2004) showed that the corner magnitude (a similar measure) in Continental Convergent Boundaries is 8.46, with a likely range from 8.07 to 8.67.

The high corner magnitudes quoted here were obtained by fitting an exponentially tapered Gutenberg-Richter distribution fit to a global earthquake catalog where the seismicity was partitioned into seven tectonic types. This method of estimating maximum earthquake magnitude over broad regions does not pertain to the maximum magnitude assigned to the Local Areal Source Zone component of the SSC model. The maximum magnitude in the SSC24 model is **M**8.5, within the Bird & Kagan (2004) range.

- SHIFT Model (from B1).

4. Kinematic F-E models of regional neotectonics [Shen & Bird, 2022] prepared for use in the NSHM and seismicity models based on their kinematics plus global calibrations [Bird & Kagan, 2004; Bird et al., 2009; Bird & Kreemer, 2015] suggest that seismicity due to distributed compression may be roughly equal (and additive) to that caused by strike-slip on named, mapped faults. Specifically, in my publications I have advocated a seismicity model known as Seismic Hazard Inferred From Tectonics (SHIFT), with two basic principles: (i) The long-term seismic moment rate of any tectonic fault, or any large volume of permanently deforming lithosphere, is approximately that computed using the coupled seismogenic thickness of the most comparable class of plate boundary. (ii) The long-term rate

of earthquakes generated along any tectonic fault, or within any large volume of permanently deforming lithosphere, is approximately that computed from its SHIFT moment rate using the frequency–magnitude distribution of the most comparable class of plate boundary.

SHIFT is one method for estimating the seismicity rates associated with inelastic off-fault deformation. As noted by Dr. Bird, it produces rates that average over large volumes of permanently deforming lithosphere. PG&E (2024, section 6.2.3) outlines the reasons why the SHIFT method was not used in the SSC development. In particular, it makes the strong assumption that the spatial variations in seismicity across broad regions of similar tectonics can be used to construct MFDs for a particular tectonic domain (an ergodic assumption), which is not considered appropriate for site-specific PSHA. The USGS investigated, but did not use, such methods in the deformation modeling of the western United States for the 2023 NSHM update (Johnson et al., 2024). The SRT agrees with PG&E that the SHIFT methodology is unqualified for use in the DCPP SSC.

- Hangingwall Effect (from B2).

5. A necessary step in every seismic source characterization probabilistic seismic hazard assessment study is the use of ground-motion prediction equations (GMPEs) to estimate shaking from earthquake magnitude, distance, and other geometric factors. One of the most respected sources of GMPEs in the "next-generation" literature is Campbell & Bozorgnia (2014). This ground motion model recognizes the special hazard in the hanging-wall of a thrust. Thus, modern practice provides ways to estimate the hanging-wall effect, although these were apparently not used in the 2015 SSC study.

PG&E participated in the development of the NGA-West2 ground motion models (the current standard) and funded the hangingwall part of that study. The SSC15 and SSC24 logic trees include five alternative representations of the hangingwall term (Madugo & Kottke, 2024).

- High-Angle Reverse Faulting (from B3). In response to PG&E evidence that reverse faults may have steep dips when they are reactivated normal faults from older extension, Dr. Bird states:

6. Yes, there are documented cases (in other places) of normal faults that later reversed their slip and become thrusts. However, these all occurred in cratons (areas of ancient, highgrade-metamorphic continental crust) where there are very few brittle faults available for reactivation. In the Irish Hills, however, there is little high-grade metamorphic basement (just small blobs within the Franciscan Formation) and a multitude of Cretaceous-Paleogene thrust faults available for reactivation. Frictional mechanics dictates that the ones that will be reactivated first are those with dips ~25º.

The SRT analysis of §3.2 describes the mechanical feasibility of high-angle reverse faulting. It includes a published study (Smith et al., 2017) of high-angle reverse faulting in the Moonlight Fault Zone, an inverted basin-bounding system on the South Island of New Zealand. This region is tectonically more similar to the Los Osos domain than to a craton. There are many other examples of high-angle faulting in inverted basins of tectonically active regions, including the well-documented Oak Ridge reverse fault in the nearby Ventura basin (Yeats et al., 1988).

3. Technical Analyses

This section provides technical analyses of five problems raised in the Bird critique:

§3.1 Gravimetric data and models

§3.2 Fault reactivation conditions

§3.3 Fault system geometry and kinematics

§3.4 Geodetic data and models

§3.5 2024 Noto Peninsula earthquake as an analog for thrust faulting beneath the Irish Hills

3.1. Gravimetric Analysis

Dr. Bird asserts that active thrust faulting must explain not only the 0.2 mm/yr uplift rate of the Irish Hills but also a crustal thickening rate that is about six times larger. His calculation and inferences from gravity anomalies assume that the mass compensation mechanism is Airy isostasy, where the local topographic height is balanced by the local Moho depth. This section discusses Airy compensation as a limiting case of regional compensation. From the gravimetric analysis, the SRT concludes that (a) Airy isostasy cannot be applied to the compensation of loads of as small as the Irish Hills, and (b) the gravity anomalies associated with the Pismo Syncline and Irish Hills can be successfully explained by plausible models based on Bouguer (rigid plate) compensation without Moho variations.

3.1.1. Regional Compensation

The most realistic and widely applied model of crustal isostasy is *regional compensation*, where non-isostatic loads are supported by the flexural rigidity of the lithosphere (Watts, 2023). This type of compensation can be parameterized by an elastic plate thickness T_e related to the flexural rigidity and the characteristic bending wavelength of the lithosphere. The Airy model corresponds to the limiting case of zero flexural rigidity ($T_e \rightarrow 0$). The observed values of T_e in the western U.S., where the mantle lithosphere is relatively weak, can be approximated by the thickness of the seismogenic zone (Maggi et al., 2000; Hyndman et al., 2009). This correlation gives $T_e \approx 10$ km for the Irish Hills. The characteristic bending wavelength λ_c for a 10-km elastic plate thickness is about 200 km. The extreme limits, 5 km < T_e < 25 km, yield the range 130 km < λ_c < 450 km (Figure 3.1). For loads of large horizontal dimension, $d \gg \lambda_c$, the isostatic response corresponds to the Airy model (complete local compensation); for loads of small dimension, $d \ll \lambda_c$ the response corresponds to the Bouguer model (no compensation). The horizontal dimensions of the Irish Hills ($d \approx$ 15-25 km), shown by the gray band in Figure 3.1, are much smaller than $\lambda_c \approx$ 200 km. Therefore, the flexural response of the Irish Hills is approximated by the Bouguer limit ($T_e \rightarrow \infty$), not the Airy limit ($T_e \rightarrow 0$) as assumed by Dr. Bird.

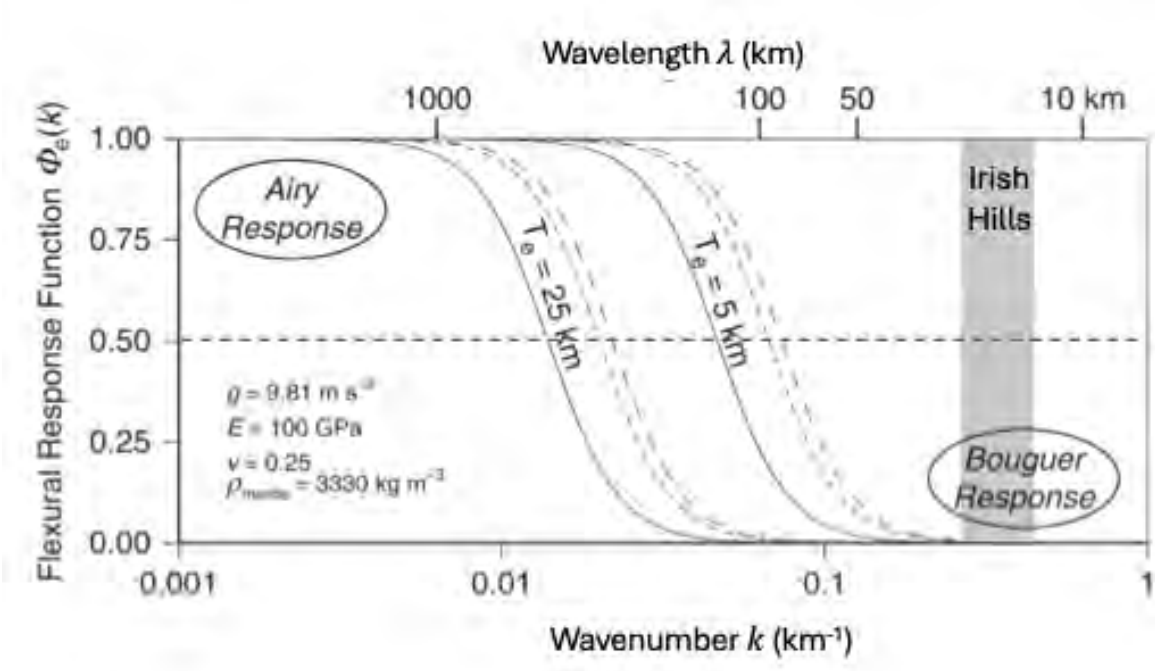

Figure 3.1. Elastic flexural response Φ_e as a function of the bending wavelength λ (top scale) or wavenumber $k = 2\pi/\lambda$ (bottom scale) for the two extreme values of the elastic plate thickness, T_e = 5 km and 25 km. Dashed lines correspond to different infill densities. The characteristic bending wavelength λ_c for a fixed value of T_e corresponds to Φ_e = ½ (dashed line). This plate model yields bending wavelengths of 130 and 450 km for T_e = 5 and 25 km, respectively. For loads of large horizontal dimension, $d \gg \lambda_c$, the response corresponds to the Airy model (complete local compensation); for loads of small dimension, $d \ll \lambda_c$, the response corresponds to the Bouguer model (no compensation). The dimensions of the Irish Hills, 15 km × 25 km, shown by the gray band. The flexural response of the Irish Hills corresponds to the Bouguer limit. [Source: Watts (2023), fig. 5.2 (annotated).]

3.1.2. Interpretation of Gravity Anomalies

The gravity data for central California have been successfully modeled in the Bouguer limit by Langenheim et al. (2012). Figure 3.2 shows their gravity and magnetic model along a profile that extends from offshore of the DCPP northeastward for 65 km (F-F' in their fig. 10). The 20-mgal negative gravity anomaly in the red oval of Figure 3.2 has been interpreted by Dr. Bird as indicating thicker crustal roots than predicted by Airy compensation (§2.2.1f). However, this negative anomaly is well modeled by the low-density sediments in the axis of the Pismo Syncline; no Moho variation is required, and, given the small horizontal scale lengths, not much is expected. More generally, Langenheim et al. (2012) observe, "Isostatic residual gravity anomalies reflect density variations in the upper 10-15 km with one of the most prominent density contrasts being that between low-density Neogene sedimentary rocks and dense Mesozoic basement rock types.” The SRT notes that both the gravity and magnetic data are well fit by an imbricated structure with identifiable geologic units separated by near-vertical faults.

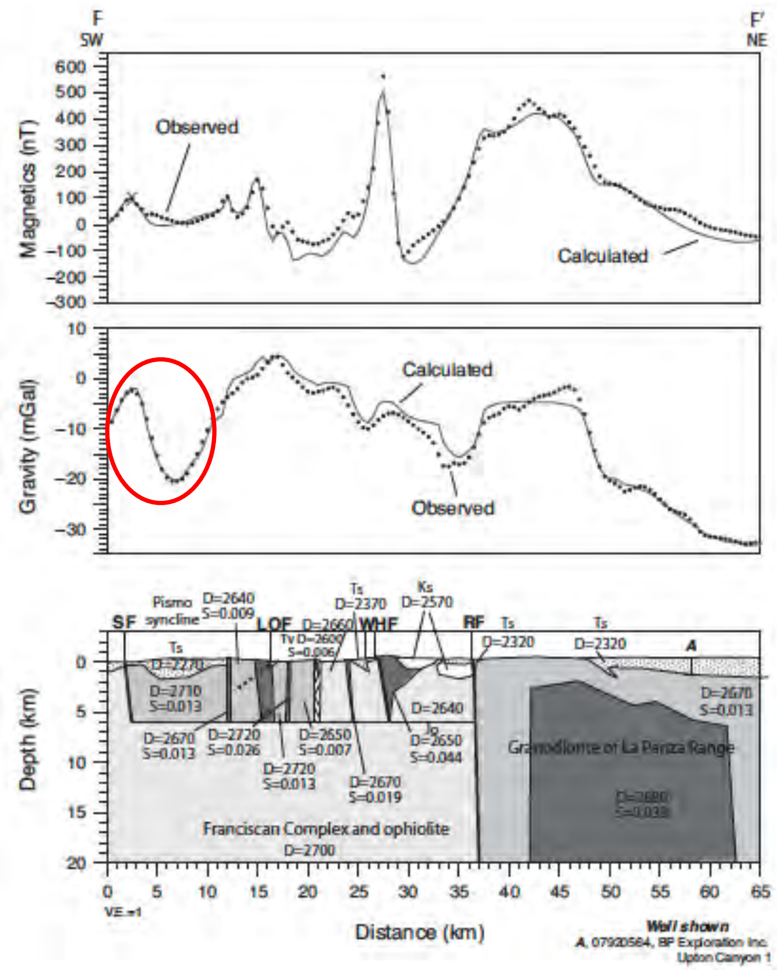

Figure 3.2. Gravity and magnetic model across a 65-km profile F-F′ of Langenheim et al. (2012). D and S are density and magnetic susceptibility in kg/m^3 and SI units, respectively. If no value for S is given, S equals zero. Bodies west of the Rinconada fault consist of undivided Franciscan Complex and ophiolite (unless otherwise labeled). These bodies are set to a depth of 6 km. Unit labels: Jo—Jurassic ophiolite; Ks—Cretaceous sedimentary rocks; Ts—Tertiary sedimentary rocks; Tv—volcanic rocks of the Morro Rock–Islay Hill volcanic complex. LOF—Los Osos fault; RF—Rinconada fault; SF—Shoreline fault; WHF—West Huasna fault. V.E.—Vertical exaggeration. Red oval contains the 20-mgal gravitational anomaly associated with the Pismo Syncline. [Source: Langenheim et al. (2012), fig. 10 (annotated).]

3.2. Fault Reactivation Analysis

Dr. Bird has questioned whether the high-angle reverse faulting in the SSC24 model is mechanically feasible, asserting that faults with dips of 50º-80º are mechanically impossible in the present horizontal compressive stress regime. This section summarizes the mechanics of fault initiation and reactivation (Sibson, 1989; Scholz, 2002; Smith et al., 2017). The SRT concludes that high-angle reverse faulting is (a) mechanically feasible in the transpressional regime of the Los Osos domain and (b) widely observed in inverted basin-bounding fault systems around the world. The theoretical summary adheres to Sibson’s (1989) mathematical notation.

3.2.1. Fault Initiation

The well-established Mohr-Coulomb theory, cited by Dr. Bird, characterizes the strength and failure of a homogeneous, isotropic rock mass by assuming that the shear stress τ across a potential plane of failure is linearly related to the effective normal stress σ_n' perpendicular to the plane (Scholz, 2002). The effective normal stress is the elastic normal stress σ_n reduced by the fluid pressure P_f within the rock mass, $\sigma_n' = (\sigma_n - P_f)$. The Mohr-Coulomb failure criterion is

$$\tau = C + \mu_i(\sigma_n - P_f)$$

The two parameters are C, the intact cohesive strength of the rock mass, and μ_i, the coefficient of internal friction. In a triaxial compressive stress regime ($\sigma_1 > \sigma_2 > \sigma_3 > 0$) where the least principal stress σ_3 is vertical, failure will initiate as thrust faults with a strike normal to the σ_1 direction and a dip angle given by

$$\theta_i = \frac{1}{2}\arctan(1/\mu_i)$$

Byerlee (1978) showed that, for most rock types (fault gouge is an exception), μ_i lies in the narrow range 0.60-0.85, and this range predicts new faults will be thrust faults with dips of 30º-25º, as noted by Dr. Bird. The dip angle increases as μ_i decreases, approaching 45º as $\mu_i \to 0$. The initial orientation of a new fault by Mohr-Coulomb failure is independent of the intermediate principal stress σ_2, the cohesive strength C, and the fluid pressure P_f.

3.2.2. Fault Reactivation

The Mohr-Coulomb failure criterion for fault initiation assumes the strength of the rock mass is homogeneous and isotropic. Those conditions do not apply to active fault systems, where most of the slip occurs on preexisting fault structures. Once a fault is formed, its cohesive strength drops to nearly zero, and the failure criterion becomes $\tau = \mu_s(\sigma_n - P_f)$, where μ_s is the static coefficient of fault friction. Owing to the drop in strength, faults are zones of weakness that can be reactivated in stress fields that are not optimally oriented.

Fault reactivation is more complicated than fault initiation because it is sensitive to pore pressure. The pore-fluid factor is defined to be the ratio of fluid pressure to overburden pressure, $\lambda_v = P_f/\rho g z$, where ρ is the rock density, g is the gravitational acceleration, and z is the depth. An expression for the differential stress required for frictional reactivation of a fault with dip θ_r at a depth z was derived by Sibson (1989):

$$\sigma_1 - \sigma_3 = \mu_s\left(\frac{\tan\theta_r + \cot\theta_r}{1 - \mu_s\theta_r}\right)\rho g z(1 - \lambda_v)$$

Figure 3.3, taken from Smith et al. (2017), illustrates the differential stress $\sigma_1 - \sigma_3$ required for frictional reactivation of cohesionless faults at a depth of 5 km and a dip angle θ_r to the maximum principal stress, parameterized by the pore fluid factor λ_v using Sibson's (1989) reactivation model. In the case where $\mu_s = 0.6$ (Byerlee friction), the optimum angle θ_r^* that minimizes $\sigma_1 - \sigma_3$ is 30º, about the same as θ_i, but there is a wide range of dips for which preexisting faults will fail before the intact rock mass initiates thrust faulting (Figure 3.3a). The dip angle in this reshear field can be as large as 48º if fluid pressure is hydrostatic ($\lambda_v \approx 0.4$), and it approaches the lock-up angle $2\theta_r^* \approx 60$º as the fluid pressure rises to lithostatic ($\lambda_v \to 1$).

Fault reactivation at even higher dip angles is commonly observed in inverted sedimentary basins around the world (Turner & Williams, 2004; Reilly et al., 2017). A relevant example is the Moonlight Fault Zone, a basin-bounding normal fault zone on the South Island of New Zealand that was reactivated as a high-angle reverse fault with dips of 60°–75°. Smith et al. (2017) measured the static friction of phyllosilicate-rich fault gouge exhumed from the fault core and obtained very low friction coefficients ($0.19 < \mu_s < 0.25$). Figure 3.3b shows the reactivation diagram for $\mu_s = 0.2$. In this case, the maximum dip angle in the reshear field is about 76º if fluid pressure is hydrostatic, and it increases to the lock-up angle $2\theta_r^* \approx 80$º as the fluid pressure approaches lithostatic.

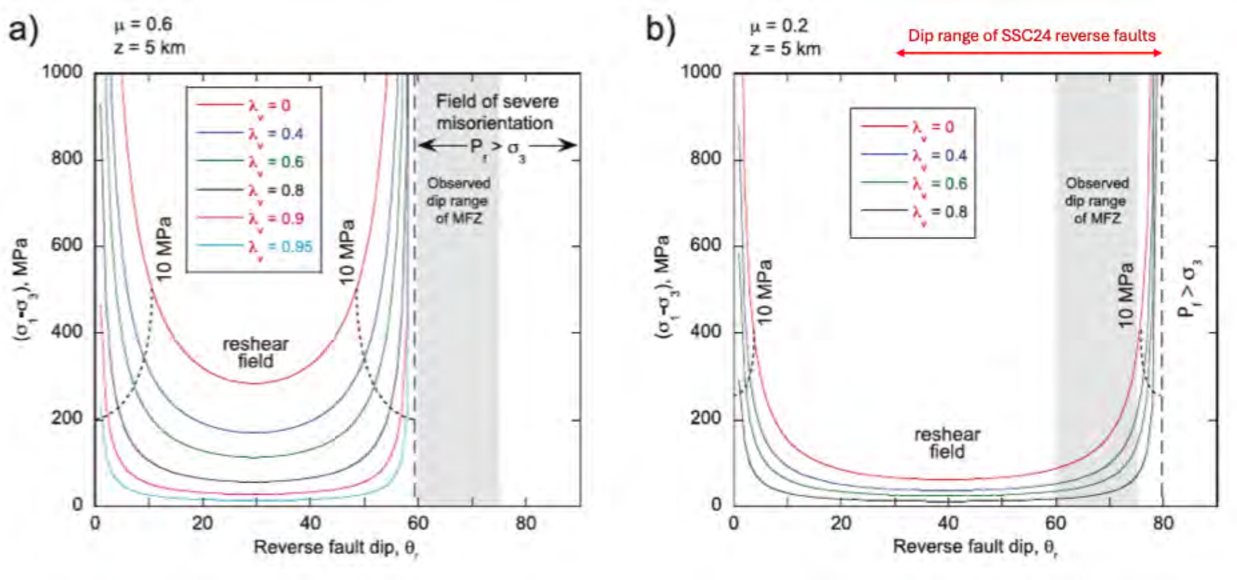

Figure 3.3. Plots of differential stress (σ_1- σ_3) required for frictional reactivation of cohesionless faults at a depth of 5 km and an angle θ_r to the maximum principal stress, parameterized by the pore fluid factor λ_v using Sibson's (1989) reactivation model. Dashed lines approximate the shear strength of intact rock with a tensile strength of 10 MPa. The reshear field bounded by these dashed lines represents the region in which reactivation of a preexisting fault will occur in preference to shear failure of intact rock. Grey shaded region is the observed dip range of the Moonlight Fault Zone (MFZ) studied by Smith et al. (2017). Results are shown for **(a)** a Byerlee friction coefficient of 0.6, and **(b)** a representative friction coefficient of 0.2 from the laboratory measurements of Smith et al. (2017). Red arrow shows the 30º-80º range of dip angles in SSC24. [Source: Smith et al. (2017), fig. 6 (annotated).]

A combination of low static friction and high fluid pressure can thus account for the reactivation of the steeply dipping reverse faults featured in the SSC24 model. Low friction is not necessary, however. A high-angle inverted fault with a Byerlee frictional coefficient can be reactivated if the fluid pressure exceeds the overburden pressure ($\lambda_v > 1$). For example, if $\lambda_v = 1.05$, a fault with $\mu_s = 0.6$ and $\theta_r = 70$º will fail at a differential stress of only 30 MPa (Sibson, 1989). Values of λ_v higher than unity cannot be sustained over the long term, because higher pressures will initiate hydraulic extension fracturing, causing the fluid to drain and the fluid pressure to drop. However, there is abundant field evidence that supralithostatic pressures can build up and discharge episodically in concert with seismogenic fault slip (Sibson, 2020). In their study of mesothermal gold-quartz deposits, Sibson et al. (1988) concluded, “Friction theory and field relations suggest that the high-angle reverse faults acted as *valves*, promoting cyclic fluctuations in fluid pressure from supralithostatic to hydrostatic values. Because of their unfavorable orientation in the prevailing stress field, reactivation of the faults could only occur when fluid pressure exceeded the lithostatic load.”

The above analysis of fault reactivation assumes compressional conditions, where the fault strike is perpendicular to the maximum principal stress σ_1. A combination of strike-slip and shortening occurs under transpressional conditions typical of coastal California (Minster & Jordan, 1987). The zero shear stress condition at the surface disfavors the initiation of oblique-reverse faults (Anderson, 1905). However, a reactivated dip-slip fault will generally exhibit oblique slip (Angelier, 1979; Gephardt, 1990) unless optimally aligned with a strike parallel to the intermediate σ_2 stress axis or if energy conditions favor slip partitioning with an adjacent strike-slip fault (Michael, 1990). Slip-tendency analysis from Morris et al. (1996) shows that for oblique slip under transpression, where σ_2 and σ_3 are similar in magnitude, the most favorable dip and the lock-up dip increase as fault strike rotates away from the optimal orientation, further facilitating slip at high dip angles.

3.3. Fault System Analysis

Dr. Bird hypothesizes that faults responsible for uplift of the Irish Hills should dip at a low angle of 25°, rather than the range of 45° to 80° dips considered in the PG&E SSC. He further claims that the total thrust heave on the San Luis Bay-Inferred Coastline thrust (collectively within the SWBZ) indicates a fault throw of 1.6 to 2.2 km and thus a slip rate of 0.76-1.04 mm/yr averaged since 5 Ma. Dr. Bird suggests that one or more structural models should have been developed that show how the sedimentary rocks exposed within the Irish Hills came to be folded into the Pismo Syncline. In this section, we address the issue of reverse fault geometry beneath the Irish Hills in the context of fault activity expressed in the pattern of uplift, folding, and tilting evident from marine terrace elevations, and we discuss how relating this record to pattern of deformation evident from folding may be used to test the range of plausible fault dip on the SWBZ.

3.3.1 Active Structures Uplifting the Irish Hills

The PG&E SSC identifies the Los Osos fault and the Southwest Boundary Zone (SWBZ) as two principal structures responsible for uplift of Irish Hills. In the SSC15 report they use the San Luis Bay fault trace as representative of the SWBZ nearest to DCPP. Three fault geometry models are proposed to explain the configuration of faulting at depth. The Northeast-Vergent model (least favored, with 20% weight) places a moderate dip of 50° on the Los Osos fault beneath the Irish Hills. At approximately the position of San Luis Obispo Creek, convergence transfers from the Los Osos fault to the SWBZ for the remaining, eastward continuation of the San Luis Range. The Southwest-Vergent model (40% weight) places a moderate dip of 45° to 50° on SWBZ and extends this fault to root within a horizontal detachment horizon at the base of the seismogenic zone at 12 km depth. The Los Osos trend is modeled as an active fold hinge developed as slip is transferred from detachment to the SWBZ (PG&E, 2015) with some secondary faulting within the hinge zone to explain minor, and somewhat contradictory, faulting observed in trenching studies of the Los Osos trend (Lettis & Hall, 1994). We note that in the SSC15 report, the position and 80° inclination of the Los Osos hingeline does not bisect the angle between the SWBZ and the horizontal detachment, and thus the Southwest-Vergent model is not a kinematically correct fold solution. The Outward-Vergent model (40% weight) places steep dips on both the Los Osos fault (60°) and SWBZ (75°) and ascribes uplift of the Irish Hills to both structures.

The SWBZ consists of a number of discontinuous, parallel active northeast-dipping fault strands that offset Late Quaternary marine deposits onshore and offshore (Lettis et al., 1994; Weigers, 2011; PG&E, 2014a). Onshore outcrop observations of the dip of the SWBZ (Table 3.1) range between 25° and 52-56°. The mean of these from 9 observations is 38°, and the standard error in the mean is ± 3°. These moderate dip values conflict with interpreted dips of 65°-85° (average 72°) from onshore seismic reflection imaging across the San Luis Bay fault (PG&E, 2014c). The steepest dip observed on an active SWBZ fault strand occurs on the Wilmar Avenue fault at Pismo Beach, where the main strand dips 65°, but with evidence for antithetic, bedding-plane slip within an overturned syncline in the footwall. Summing the observed offsets of the capping marine terrace (Lettis & Hall, 1994; Nitchman & Slemmons, 1994) reduces the net fault dip here to between 52° and 56°. In the offshore region, seismic imaging suggests a moderate dip for the Los Berros fault (PG&E, 2014b), which we estimate to be 40° (Table 3.1).

The Los Osos trend defines the boundary between the uplifting Irish Hills and the low-lying Los Osos valley and Morro Bay. Three hypotheses are proposed (PG&E, 2014a) to explain this trend: a southwest-dipping reverse fault, a strike-slip fault, or a fold hinge related to uplift above the SWBZ. Observations that support uplift to the south of the Los Osos trend include elevated marine terraces along the western edge of the Irish Hills (Hanson et al., 1992), incised antecedent channels of San Luis Obispo Creek and Pismo Creek that form water gaps across the Irish Hills and San Luis Range, and northeast-tilted alluvial fans and stream terraces with subtle, northeast-facing scarps and northeasterly derived sediments (Lettis & Hall, 1994).

Table 3.1. Summary of SWBZ fault dip observations

San Luis Bay Fault		
Mapping west of Avila Beach	30°, 25°, 34°, 33°, 43°, 46°, and 37°	Lettis et al. (1994)
Outcrop log of San Luis Obispo Creek	38 ± 5°, decreasing up-dip.	Lettis et al. (1994)
Wilmar Avenue Fault		
Sea cliff at Pismo Beach	65° dip, with bedding-parallel slip on antithetic vertical faults in footwall	Nitchman and Slemmons (1994)
	Shears dipping between 45° and 70°	Lettis et al.(1994)
	52-56° from summation of primary and antithetic fault slip	This report
Los Berros Fault		
San Luis Obispo Bay, Line 86-3	Shallow dip suggests a thrust fault	PG&E (1994)
	40° from seismic line rescaled 1:1	This report
Los Osos Fault		
Ellsworth Site	75° (NE dipping backthrust?)	Lettis and Hall (1994)
Cuesta Site	46°, 72°, 45°, 47° (all NE dipping)	Lettis and Hall (1994)
	15°SW	Lettis and Hall (1994)
Ingley Site	22° SW and 80°NE (backthrust?)	Lettis and Hall (1994)
Sycamore Canyon Creek Exposure	44° NE and evidence of strike-slip	Lettis and Hall (1994)
Glick Site	36°	Lettis and Hall (1994)

Enigmatically, paleoseismic trenching by Lettis & Hall (1994) revealed the northeast-facing scarps to be underlain by northeast dipping faults, rather than the expected strands of a southwest-dipping Los Osos reverse fault. These faults must bend sharply at shallow depth to produce the observed scarps in their hangingwall, suggesting that these faults may be shallow features related to tilting. Detailed geologic and geophysical surveys by PG&E (2014a,b) also failed to find definitive evidence for a throughgoing southwest-dipping reverse fault, and indeed they found geologic evidence for contiguous rock outcrops across the Los Osos trend that argue against significant fault offset. Moreover, except for localized subsidence at Morro Bay, no basin has formed in the footwall of the proposed Los Osos reverse fault. Taken together, these lines of evidence suggest that the reverse-fault interpretation of the Los Osos trend may be incorrect; they instead favor interpretating this trend as a hinge zone related to the geometry of the SWBZ at depth, perhaps with some superposed strike-slip faulting.

3.3.2 Kinematically Constrained Fault Models

Fault-related fold theory (Suppe, 1983; Suppe & Medwedeff, 1990; Narr & Suppe, 1994) provides a framework to quantitatively relate fold shape and history to the geometry of underlying faults. The principal fold structure of the Irish Hills is the Pismo Syncline, which has a fold axis that strikes parallel to both the SWBZ and the Los Osos trend. The cross-section reconstructions of the Irish Hills by PG&E (2014a) do not employ fault-related fold theory to relate the Pismo Syncline to the geometry of the underlying fault system. Such reconstructions, though non-unique, would provide additional insight into the geometry and slip rate of faulting beneath the Irish Hills. The range of permissible models may be narrowed by considering geometry of overlapping strata and patterns of active uplift (Medwedeff, 1989; 1992; Suppe and Medwedeff, 1990). Two such constraints from the Irish Hills are the block-like pattern of uplift evident from marine terraces, and the angular unconformity at the base of the Upper Pismo formation.

The Upper Pismo Formation (Gragg, Bellview, and Squire members) is conformable upon older strata within the core of the Pismo Syncline, but this contact becomes an angular and buttress unconformity across the southern limb of the fold (Weigers, 2011, 2021; PG&E, 2014a). Here, the base of the Upper Pismo Formation cross-cuts all older units on the south limb along an eroded, irregular contact that declines in elevation southward to near sea level (Figure 3.4). The Upper Pismo Formation is a shallow marine sandstone that appears to have been emplaced as the south limb of the syncline began to tilt and emerge above sea level, but before the core of the syncline had begun to fold. The position of this feature on the south limb of the Pismo Syncline supports that fault-related folding initiated with slip on the SWBZ. Furthermore, the preservation of this feature in the mapped geology indicates a limited amount of overthrusting and erosion of the hangingwall of the SWBZ. This contradicts Dr. Bird's assertion of ~4 to 5 km of overthrusting to produce 1.6 – 2.2 km of throw of the Obispo formation in the hanginwall of the SWBZ.

Over the last 124.0 ± 2.5 kyr of deformation recorded since the formation of Q2 marine terrace, the core of the Irish Hills have uplifted in a block-like manner (Lettis et al., 1994). This pattern of uplift is consistent with translation of the Irish Hills above a north-northeast-dipping fault ramp corresponding to the SWBZ. The Los Osos trend, which forms the northern boundary of this uplifting block, may thus be interpreted as an active fold hinge that accommodates the translation of material onto this ramp from a horizontal detachment surface (flat). To maintain cross-sectional area, the hingeline should bisect the angle between the ramp and flat fault segments.

Figure 3.5 shows a permissible type of fault-related fold model that honors the above constraints. The SWBZ includes a moderately dipping San Luis Bay fault, consistent with observed dips from outcrop data (Table 3.1). Folding of the south limb of the Pismo Syncline is hypothesized to have occurred as reverse slip on the SWBZ transferred to the steeply dipping San Miguelito fault, a Miocene basin-bounding normal fault reactivated with reverse slip but presently inactive (PG&E, 2014a). Because the active San Luis Bay fault does not bend at shallow depth, the syncline translates upward in the hangingwall, consistent with evidence from marine terraces (Figure 2.2). The shorter north limb of the Pismo Syncline is hypothesized to have formed by buckling induced by slip along reactivated strands of the Edna fault, consistent with the structures modeled by PG&E (2014a). A significantly steeper dip for the SWBZ does not provide a suitable geometry to form the south limb of the Pismo Syncline through an upward steepening of fault dip. A significantly gentler fault dip of 25° for the SWBZ, as advocated by Dr. Bird, would require the fault surface to cut up-section to the north, which would result in an unlikely initial thrust-fault geometry and also intersect well control.

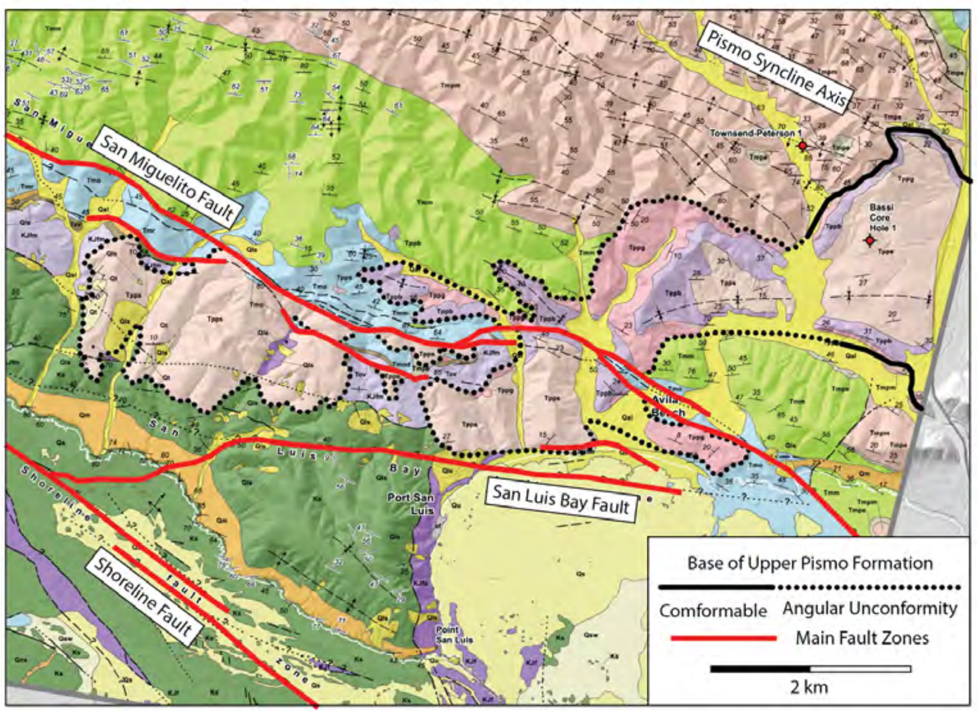

Figure 3.4. Excerpt of geologic map compilation (PG&E, 2014a), annotated to highlight the relationship of the Upper Pismo Formation to underlying strata and major faults of the SWBZ. Upper Pismo Formation is comfortable upon older strata near the axis of the Pismo syncline but exhibits angular unconformity with older strata across its south limb. The San Miguelito fault originated as a north-dipping normal fault that created accommodation space for Monterey formation (light green) and Lower Pismo formation (light tan). The San Miguelito fault was later reactivated as a reverse fault in the hangingwall of the SWBZ, leading to uplift and tilting of the south limb of the Pismo Syncline. The San Luis Bay fault, located structurally below the San Miguelito fault, is the active strand of the SWBZ at this locality.

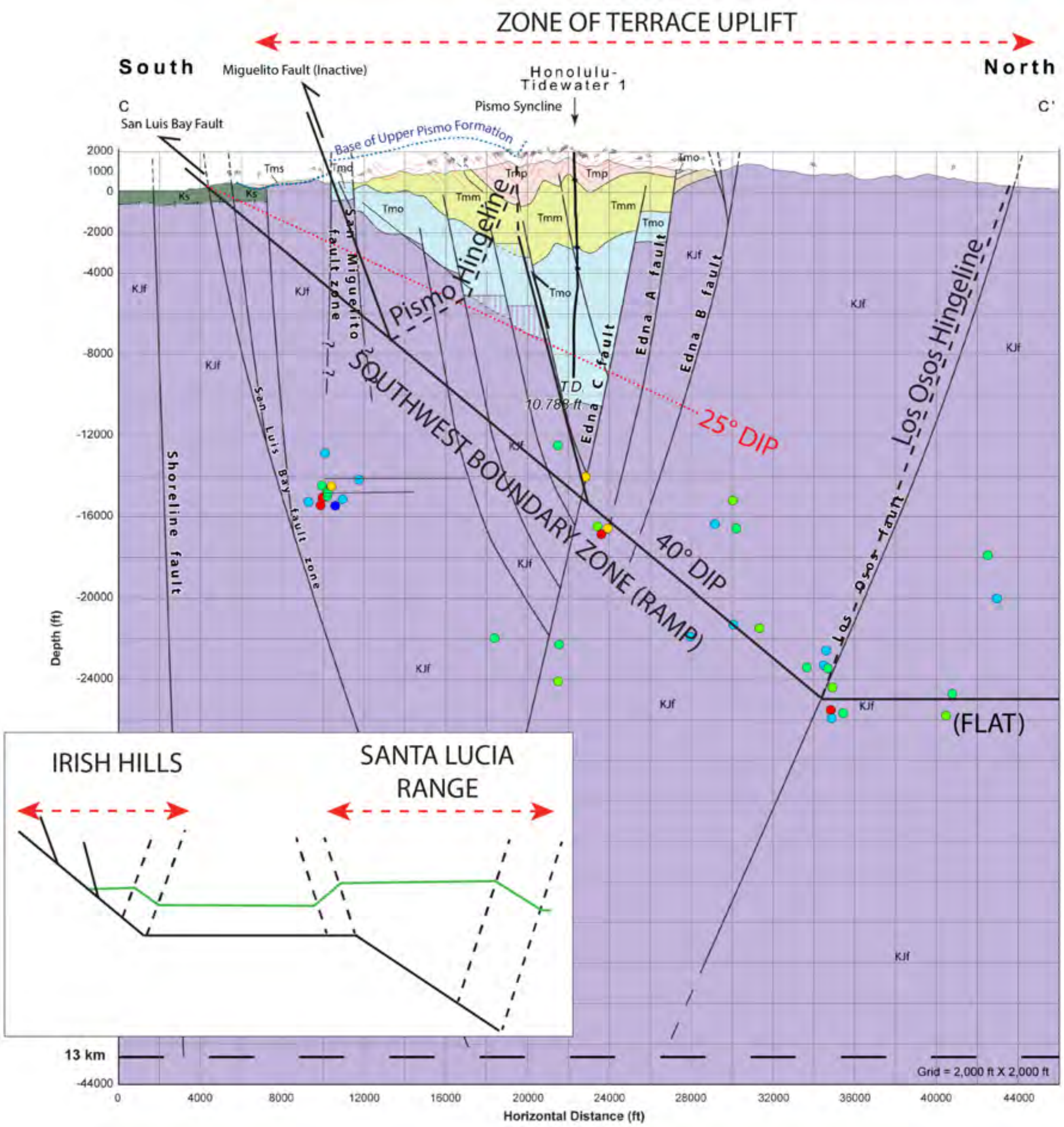

Figure 3.5. Cross-section C-C' from PG&E (2014), annotated with fault-bend fold model for the SWBZ. Tilting of the south limb of Pismo Syncline occurred due to slip transfer from SWBZ ramp to the Miguelito fault, an inverted normal fault that formed the southern margin of the Pismo basin. Hingeline of the Pismo Syncline refracts upwards to accommodate bedding-parallel shear of layered sedimentary rocks overlying Franciscan basement. Note patterned areas showing revised layer positions beneath syncline axis. Base of Upper Pismo Formation in the hangingwall of the Miguelito fault projected into section from east. Red dotted line depicts a hypothetical San Luis Bay fault with 25° dip (compare to Figure 2.3). This fault configuration would intersect the Obispo formation and the Tidewater-Honolulu oil well. Diagram at lower left shows a ramp-flat-ramp model that extends the SWBZ northward to root beneath the southern Santa Lucia range. Zones of marine-terrace uplift correspond to fault ramps.

The hinge position at the Los Osos trend constrains the SWBZ to intersect a detachment horizon (flat) at about 8 km depth, which is well within the seismogenic zone and significantly shallower than modeled by PG&E (2014a). The inferred horizontal dip of this detachment horizon is necessary to explain the lack of elevated marine terraces immediately north of the Los Osos trend. This detachment may ultimately root into a deeper ramp beneath the southern Santa Lucia mountains, consistent with marine terrace uplift along the coastline at Cayucos, north of Morro Bay (Figure 3.5 inset).

Other kinematically constrained fault configurations are possible beneath the Irish Hills. For example, multiple gently dipping thrust fault strands could produce the south limb of the Pismo Syncline via an antiformal stacking mechanism; see Suppe (1983) for an example. A wedge-thrust type geometry (Narr and Suppe, 1994) with the SBFZ forming as a backthrust above deep, south-dipping ramp, could also produce the observed terrace-uplift pattern.

To summarize, kinematically constrained fault-related fold models provide a way to test hypothesized fault geometries and reveal possible source models outside of the present range considered by the PG&E SSC. Both the dip of the south limb of the Pismo Syncline and the field observations of fault dips within the SWBZ support a moderately dipping (~40°) thrust faulting solution, which is below the range presently modeled by SSC24 (45º-50º in the SW-Vergent FGM). A dip of 25°, as proposed by Dr. Bird, would require unlikely geometric conditions or a more complex model to produce the observed structure of the Irish Hills.

3.3.3 Slip-rate Analysis

We can estimate the slip rate of a kinematically constrained fault model from the folded geometry of marker horizons, together with timing information from strata deposited across a growth-related angular unconformity, or landforms uplifted by the latest increment of folding. The unconformity at the base of the Upper Pismo Formation (Figure 3.4) constrains the initiation of folding to between 4.2 Ma (PG&E 2014a) and the 6.0 Ma age of the uppermost Lower Pismo Formation (Keller and Barron, 1993). If the south limb of the syncline has grown by fault slip-transfer through a bend from the SWBZ to the San Miguelito fault, as shown in Figure 3.5, then the total slip is approximately the length of the folded limb, which we estimate to be 1.8 ± 0.2 km from this model. There is additional slip on the San Luis Bay thrust that bypasses the intersection with the San Miguelito fault. The extent of shallow-marine Squire Member of the Pismo Formation, together with evidence from uplifted marine terrace platforms in the footwall of the San Miguelito fault, indicate 200-400 m additional uplift via thrusting on the San Luis Bay fault. There is also additional deep slip on the SWBZ that contributed to buckling of the north limb of the Pismo Syncline. PG&E (2014a) estimated 7.3%–8.7% shortening spanning 3 km in this area, which corresponds to 260 ± 15 m of contraction. Together, these add 0.8 ± 0.1 km to the net slip of the SWBZ for a total of 2.6 ± 0.3 km. For an estimated 5.1 ± 0.4 Ma age of initiation, this yields a long-term slip rate of 0.5 ± 0.1 mm/yr.

Under the same modeling assumptions, we can use the uplifted marine-terraces fringing the Irish Hills to determine a slip rate averaged over the past 124.0 ± 2.5 ka. As described in §2.3, uplift of the Q2 marine terrace yields a rate of 0.18 ± 0.03 mm/yr relative to present sea level. For a thrust fault with a mean dip 38

± 3°, this rate of uplift corresponds to a slip rate of 0.29 ± 0.07 mm/yr. This rate is somewhat slower than the long-term rate of 0.5 ± 0.1 mm/yr averaged since the initiation of folding at 5.1 ± 0.4 Ma. One possible explanation for this discrepancy is that the footwall of the SWBZ is subsiding relative to present sea level. However, evidence from submerged marine abrasion platforms south of the SWBZ does not support significant footwall subsidence (PG&E, 2011).

Alternatively, the slip rate of the SWBZ has slowed over time, which is not surprising when multiple structures are available to absorb crustal shortening. For example, the Casmalia Hills fault, located approximately 25 km south of the Irish Hills, exhibits about 1500 m of total uplift since the late Miocene, of which 238-400 meters has occurred over the past 120 kyr (McGregor & Onderdonk, 2021). Growth strata relationships indicate folding related to slip on the Casmalia Hills fault since early Pliocene, ca. 4-5 Ma. This implies at least a five-fold increased rate of slip over the past 120 kyr relative to the long-term average for the Casmalia Hills fault. It is conceivable that this increased rate of slip on the Casmalia Hills fault corresponds to a decreased rate of slip for the SWBZ beneath the Irish Hills, as both faults accommodate shortening of the Santa Maria basin and may share a common mid-crustal detachment horizon (Namson & Davis, 1990).

3.4. Geodetic Analysis

Dr. Bird suggests a shortening rate of 2 mm/yr across the Irish Hills obtained by the Shen & Bird (2022) NeoKinema model and selected GPS station velocities. His geodetic analysis uses the relative velocity of GPS station CHOR relative to station DCAN at DCPP, which are separated by 17 km. If we take a conservative approach and apply this 2 mm/yr shortening over the 20-25 km wide Los Osos domain, this yields a contractional strain rate of –100 to –80 nanostrain/yr. In this section, Bird's hypothesis is tested against a regional GPS dataset, and we find that the contractional strain across the Irish Hills is two to five times smaller than his estimate.

Because the geodetic analyses described in the SSC15 and SSC24 reports are limited in scope and are based mainly on data published over a decade ago (DeMets et al., 2014; Murray-Moraleda, 2011), we present an analysis of an updated and expanded GPS dataset developed by Zeng (2022). We also analyzed data from Murray-Moraleda et al. (2011), which was available at the time of the SSC15 report. The newer geodetic data have significantly less uncertainty. For example, DCAN, the GPS station closest to DCPP, has east and north standard deviations of 1.97 and 1.88 mm/yr, respectively, in the Murray-Moraleda et al. (2011) data and 0.25 and 0.23 mm/yr, respectively, in the Zeng (2022) data—approximately eight times less uncertainty. Zeng (2022) compiled only horizontal motion estimates, while the Murray-Moraleda et al. (2011) dataset contains both horizontal and vertical motions. Our analysis found the vertical motions reported by Murray-

Moraleda et al. (2011) to have large uncertainties and spatially incoherent patterns, as is typical for vertical-component GPS data, so they do not usefully constrain the uplift rates.

Interferometric Synthetic Aperture Radar (InSAR) is available for the region and can be used to measure current deformation rates, typically at the cm/yr scale. Unfortunately, InSAR decorrelates in regions with significant vegetation (e.g., Marshall et al., 2013, Jiang and Lohman, 2021), and deformation rates on the mm/yr scale are likely too small for detection by InSAR data. For these reasons, we focus our analysis here on the Zeng (2022) horizontal GPS data.

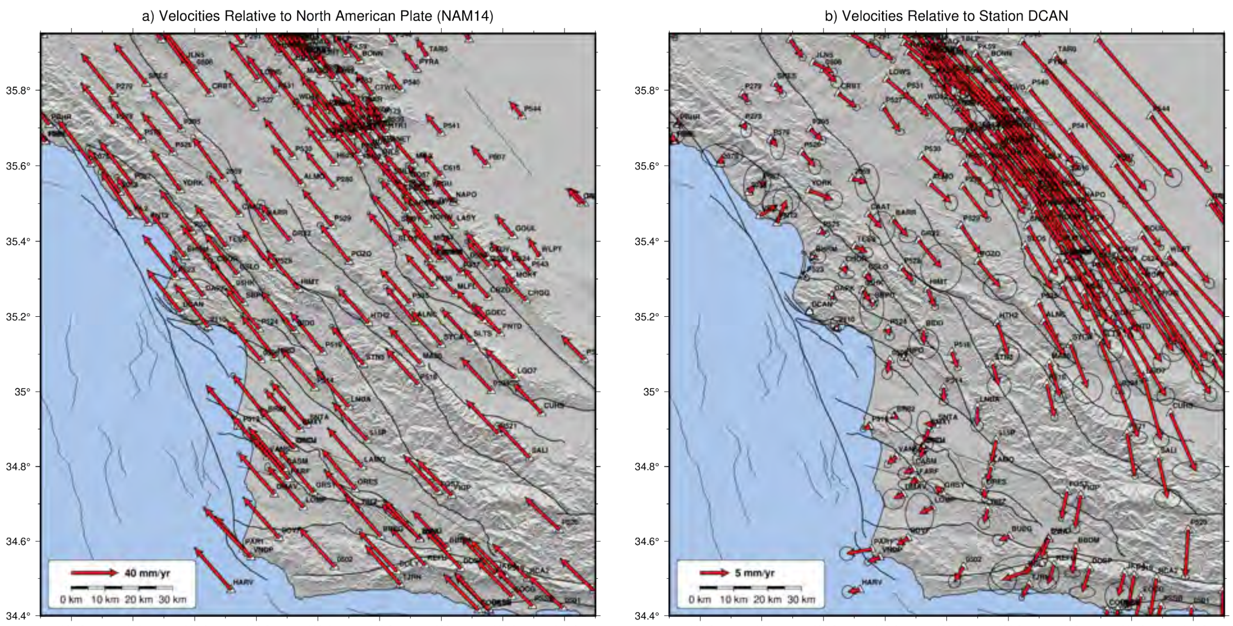

Figure 3.6. GPS velocities from Zeng (2022) **(a)** relative to the North American Plate (NAM14) and **(b)** relative to DCAN, the GPS station closest to DCPP. Note the different velocity scales. Error ellipses show the 95% confidence regions. Lines show fault traces from the Statewide California Earthquake Center (SCEC) Community Fault Model (CFM) version 7.0. Blind faults are indicated with dashed lines.

3.4.1. GPS Velocities

Zeng (2022) provided a dataset of estimates of motion at 4979 GPS stations throughout the western United States, all realized in the same reference frame relative to the North American plate (NAM14). Within the area of the geodetic analysis, which we refer to as the greater Irish Hills region (Figure 3.6), we select 253 stations, excluding data from three stations (CATF, KNGR, and MDDF) that have anomalous velocities and are closely located to other stations with smaller uncertainties. In the NAM14 reference frame, the velocities are high throughout the region due to the rapid motion of the Pacific plate (Figure 3.5a). To visualize the local deformation patterns, we shift the velocities to a local reference frame defined by station DCAN, which is a continuously recording station with relatively low uncertainties located on a hill just behind DCPP. The velocities in this local reference frame show both right-lateral shear related to the San Andreas fault and clockwise rotation (Figure 3.5b). The inverted strain rates are insensitive to the rotation, but the rotation does introduce scatter in the profile shortening rates. We experimented with removing a rotational component from the local reference frame, but in all cases, this also removed a significant portion of the San Andreas motion—an undesirable result.

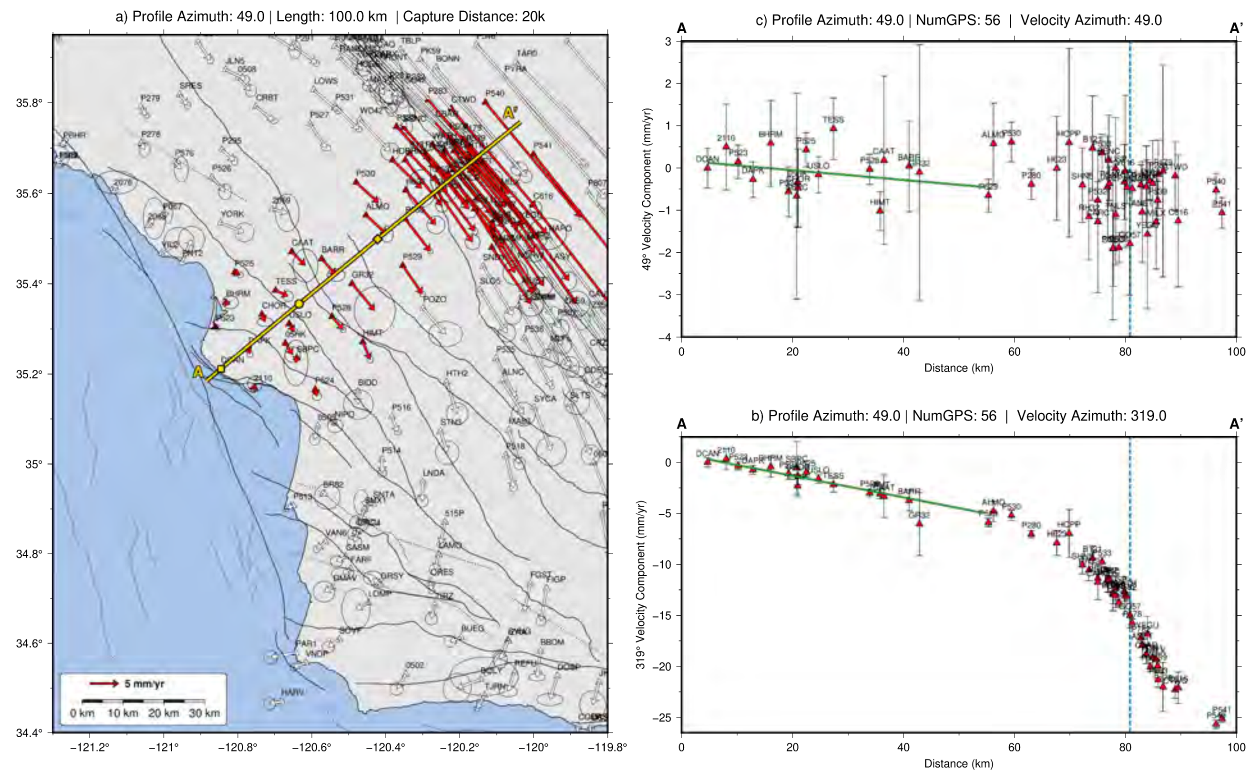

Figure 3.7. (a) Map showing the raw Zeng GPS velocities relative to station DCAN (arrows); ellipses are 95% confidence regions. Gold line is the profile A-A' normal to the San Andreas Fault (SAF). The location of station DCAN (square), a point 25 km from DCAN (circle), and a point 50 km from DCAN (diamond) are plotted on the profile. Red arrows show velocities at stations within 20 km of the profile. **(b)** Components of the red station velocities projected parallel to the SAF plotted at the distance along the profile. **(c)** Components of the red station velocities projected perpendicular to the SAF. Error bars are 95% confidence intervals. Green lines on **(b)** and **(c)** are weighted least-squares fits to the red stations within 50 km of DCAN (Table 3.2). Vertical dashed blue lines in **(b)** and **(c)** mark the profile location of the SAF. Fault traces plotted on the map are from the SCEC CFM 7.0.

3.4.2. Two GPS Velocity Profiles

To identify patterns of deformation from the GPS velocity vectors, we follow DeMets et al. (2014) in examining the velocity variations along fault-normal profiles. Two profiles at different fault-normal orientations are used in our analysis. Profile A-A' extends 100 km from DCAN to the SAF at an azimuth of 49º, perpendicular to the strike of the SAF (Figure 3.7a). Profile B-B' extends 80 km from DCAN at an azimuth of 25º, perpendicular to the strike of the SWBZ (Figure 3.8a). We refer to these profiles as the SAF-normal and SWBZ-normal, respectively. For each profile, we select GPS stations within a corridor extending

± 20 km on either side (red arrows on the maps), and we resolve the velocity vectors into profile-parallel (fault-normal) and profile-normal (fault-parallel) components, which are plotted in panels (b) and (c) of Figures 3.7 and 3.8.

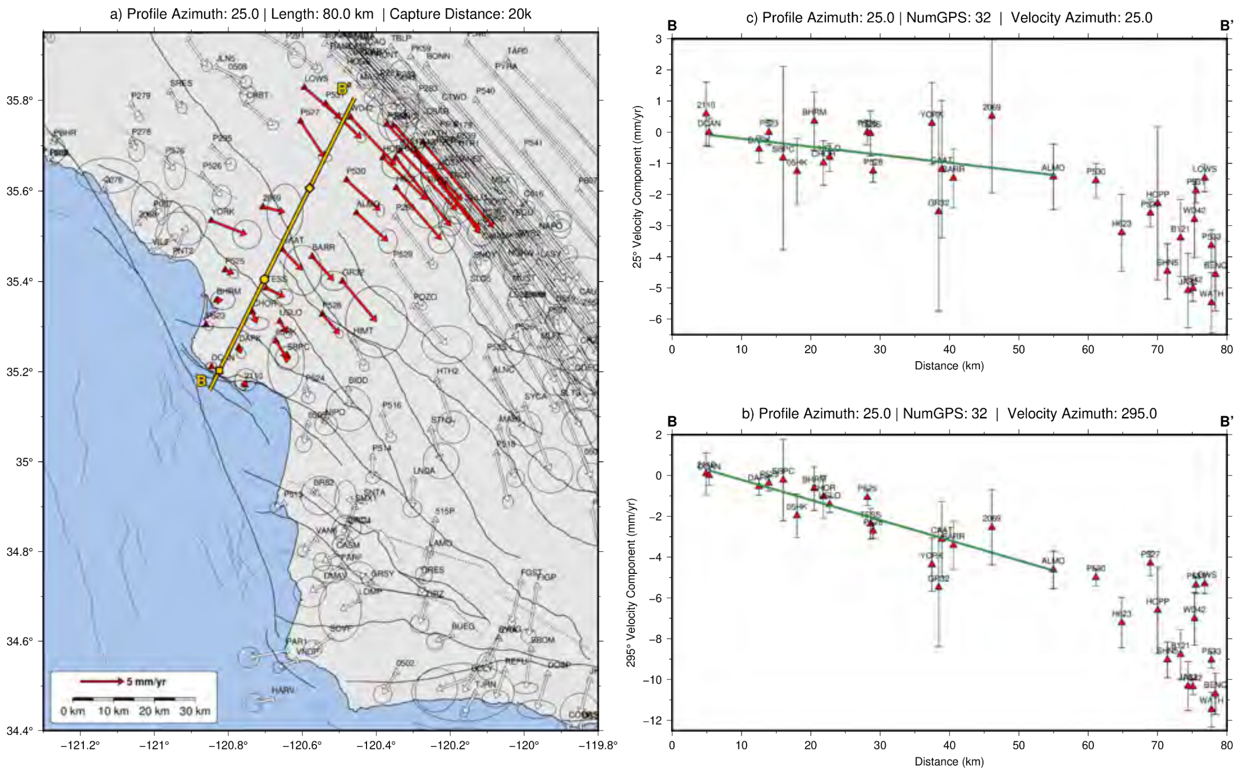

Figure 3.8. (a) Map showing the raw Zeng GPS velocities relative to station DCAN (arrows). Gold line is the profile B-B' normal to the Southwest Boundary Zone (SWBZ). **(b)** Components of the red station velocities projected parallel to the SWBZ plotted at the distance along the profile. **(c)** Components of the red station velocities projected perpendicular to the SWBZ. Green lines on **(b)** and **(c)** are weighted least-squares fits to the red stations within 50 km of DCAN (Table 3.2). Plot conventions are the same as in Figure 3.7.

Between DCAN and the SAF, profile A-A' shows about –15 mm/yr of SAF-parallel motion (Figure 3.8b). The negative value indicates right-lateral motion, which is consistent with SAF slip rates of 22-36 mm/yr measured in this region (Loveless & Meade, 2011). The deformation signal decays away from the SAF, but the dextral shear parallel to the SAF persists all the way to DCAN. The SAF-normal velocity components are much smaller, most within ±1 mm/yr of DCAN, indicating little shortening or extension along the SAF-normal profile A-A'.

Apparent linear strain rates along the A-A' profiles are estimated by weighted least-squares fitting of straight lines to the data subsets within 25 km and 50 km of DCAN. Fault-related deformation typically follows an arctangent pattern in 1D profiles, but the deformation of several closely spaced faults can produce nearly linear changes in velocity. Given the significant uncertainty in the data and no clear arctangent pattern in the 25-km and 50-km baselines, we use the linear fits to estimate deformation rates. The long-baseline fits, shown by the green lines in the profile plots, yield 50-km velocity differences of –5.30 ± 0.35 mm/yr for SAF-parallel motion and –0.58 ± 0.35 mm/yr for SAF-normal motion (Table 3.2). These velocity gradients correspond to apparent linear strain rates of –106 ± 7 nanostrain/yr and –12 ± 7 nanostrain/yr (Table 3.3). The strain-rate estimates for the 25-km baseline, –81 ± 12 nanostrain/yr and 8 ± 12 nanostrain/yr, have larger uncertainties but are consistent with the 50-km rates. The A-A' shortening rate is not significantly different from zero.

Repeating this analysis for stations along the SWBZ-normal profile B-B' shows a large fault-parallel dextral shear with 25- and 50-km strain rates of –94 ± 10 and –99 ± 7 nanostrain/yr. In this case, the fault-normal estimates, –27 ± 10 and –26 ± 8 nanostrain/yr, imply a small but significant contractional strain rate along the profile.

Table 3.2. Velocity differences across 25-km and 50-km baselines of the DCAN profiles

Profile	GPS Dataset	Projection Azimuth	25 km ΔRate (mm/yr)	50 km ΔRate (mm/yr)	Projection Azimuth	25 km ΔRate (mm/yr)	50 km ΔRate (mm/yr)
A-A′	Raw	49°	0.19 ± 0.29	-0.58 ± 0.35	319°	-2.03 ± 0.29	-5.30 ± 0.35
A-A′	Corrected	49°	-0.56 ± 0.29	-2.12 ± 0.35	319°	-2.23 ± 0.29	-5.62 ± 0.35
B-B′	Raw	25°	-0.67 ± 0.24	-1.29 ± 0.38	295°	-2.36 ± 0.24	-4.94 ± 0.37
B-B′	Corrected	25°	-1.48 ± 0.24	-3.25 ± 0.38	295°	-2.21 ± 0.24	-4.36 ± 0.37
B-B′	Raw	49°	0.35 ± 0.24	0.87 ± 0.37	319°	-2.40 ± 0.24	-5.03 ± 0.37
B-B′	Corrected	49°	-0.47 ± 0.24	-1.18 ± 0.37	319°	-2.59 ± 0.24	-5.33 ± 0.37

Table 3.3. Apparent linear strain rates averaged over 25-km and 50-km baselines of the DCAN profiles*

Profile	GPS Dataset	Projection Azimuth	25 km Strain Rate (10^{-9}/yr)	50 km Strain Rate (10^{-9}/yr)	Projection Azimuth	25 km Strain Rate (10^{-9}/yr)	50 km Strain Rate (10^{-9}/yr)
A-A′	Raw	49°	8 ± 12	-12 ± 7	319°	-81 ± 12	-106 ± 7
A-A′	Corrected	49°	-22 ± 12	-42 ± 7	319°	-89 ± 12	-112 ± 7
B-B′	Raw	25°	-27 ± 10	-26 ± 8	295°	-94 ± 10	-99 ± 7
B-B′	Corrected	25°	-59 ± 10	-65 ± 8	295°	-88 ± 10	-87 ± 7
B-B′	Raw	49°	14 ± 10	17 ± 7	319°	-96 ± 10	-101 ± 7
B-B′	Corrected	49°	-19 ± 10	-24 ± 7	319°	-104 ± 10	-107 ± 7

* Strain rates calculated from Table 3.2 by dividing the baseline velocity by the baseline length.

3.4.3. Removal of Deformation Associated with the San Andreas Fault

The strain rates derived from the raw GPS data cannot be interpreted in terms of faulting in the Los Osos domain because the signal is dominated by the SAF and related strike-slip faults outside that domain. However, the geometries, slip rates, and locking depths of the SAF and the other plate-boundary faults are relatively well known, so it is possible to remove, at least to first-order, the interseismic deformation associated with these faults. For this purpose, we predict the SAF deformation by applying the polygonal dislocation code, *poly3D* (Thomas, 1993), to a simplified block model of the SAF system developed by Loveless & Meade (2011). The block model parameters, shown in Figure 3.9, includes the Hosgri, Garlock, and San Jacinto faults, although their contributions have a negligible effect on the results. We subtract the predicted velocities from the raw Zeng GPS data and refer to the residual as the ‘corrected velocities’ (Figure 3.10).

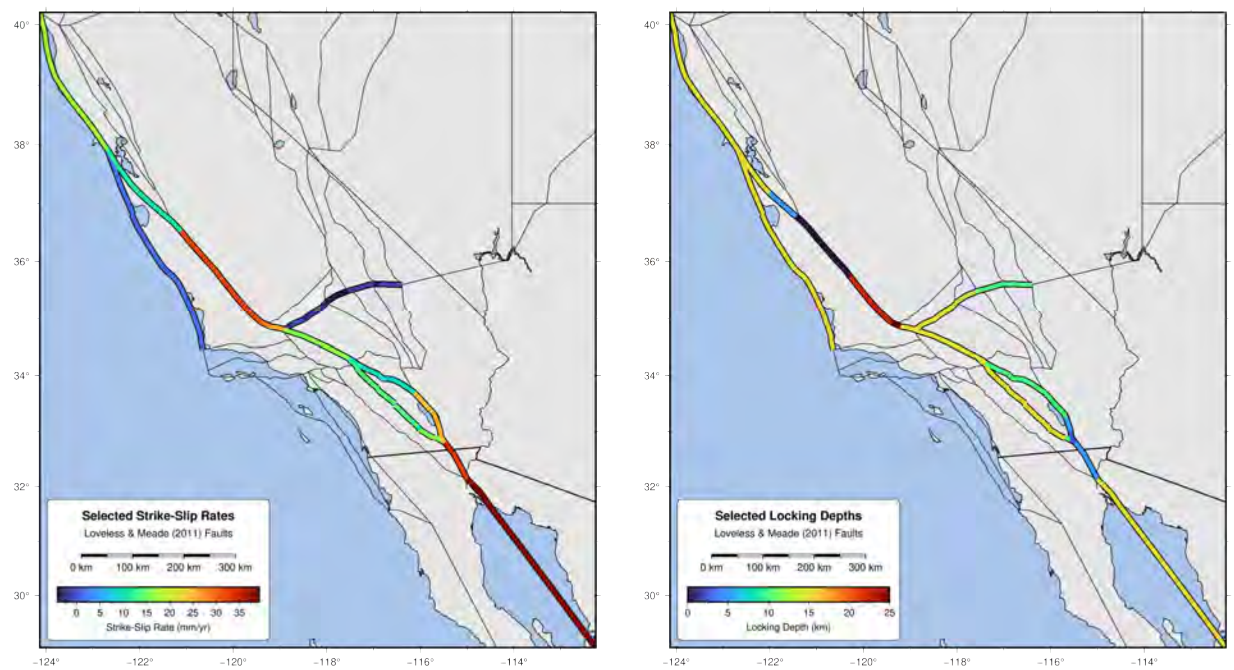

Figure 3.9. Fault geometry, slip rates, and locking depths from the Loveless-Meade block model used to remove interseismic strain from the Zeng GPS data. All Loveless-Meade faults are shown with thin black lines; the ones used in the elastic dislocation model are colored by slip rate (left panel) and locking depth (right panel). The slip rate of the Hosgri fault was reduced from the Loveless-Meade value of 6.0 mm/yr to 1.7 mm/yr for consistency with SSC24, although this choice has little effect on the results. All modeled faults extend to essentially infinite depth (10^6 km) to avoid edge effects of the lower fault tiplines.

The predicted regional fault model velocities (Figure 3.10b) show the expected NW-SE shear and clockwise rotation but also a pattern of NE-SW extension in the region of the DCAN profiles. The extension reflects the interseismic deformation related to an abrupt transition from the creeping section northwest of Parkfield to the locked fault segments to the southeast, an effect that has been described and modeled by Titus et al. (2011). The termination of the creeping section produces two large lobes of dilatational strain with a contractional region to the northeast of the SAF and an extensional region to the southwest (Figure 3.11). The GPS strain rate inversion (Figure 3.11a) of Titus et al. (2011) shows a smaller lobe of extension compared to an elastic model (Figure 3.11b), but this may be due to limited resolution of the non-uniform and sparse spacing of the GPS stations.

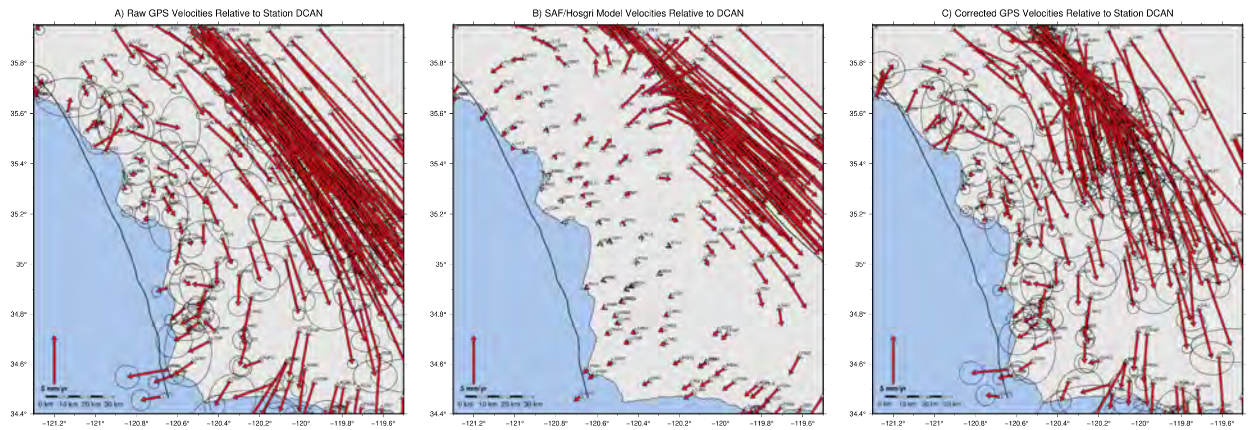

Figure 3.10. GPS velocities before and after removal of deformation related to the San Andreas, Hosgri, and other regional faults (shown with black lines). **(a)** Raw GPS velocities relative to station DCAN. **(b)** Elastic dislocation model predicted interseismic velocities based on the Loveless-Meade block model. **(c)** The final "corrected" GPS velocities that have deformation due to the San Andreas, Hosgri and other regional faults previously discussed removed. Note that the dislocation model shown in **(b)** removes extension normal to the plate boundary northeast of station DCAN as expected.

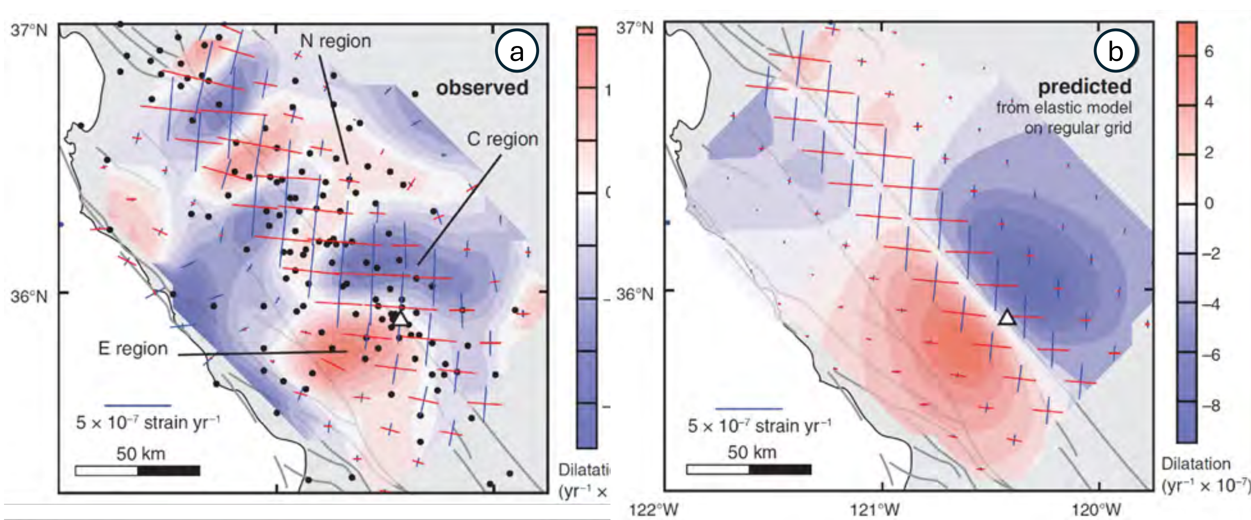

Figure 3.11. Dilatational strain rate patterns **(a)** from inversions of GPS data and **(b)** from the Titus et al. (2011) elastic model of the SAF. This interseismic strain signature is related to the abrupt transition from the locked to creeping sections of the San Andreas fault near Parkfield, CA (triangle). DCPP is just south of the map area, but the interseismic extension extends into the Irish Hills region, as seen in Figure 3.9b. [Source: Titus et al. (2011), fig. 7 (annotated).]

The effects of the SAF correction are evident in the residual velocities projected onto profiles A-A' (Figure 3.12) and B-B' (Figure 3.13). The correction removes the high gradient of the SAF-parallel motion across the SAF itself, but the apparent shear observed on the 50-km DCAN baseline (–112 ± 7 nanostrain/yr) is not reduced from the uncorrected value (–106 ± 7 nanostrain/yr) (Table 3.3). This residual SAF-parallel deformation can be partitioned into two disjunct components, shear due to the SWBZ, Los Osos, and related SLPB faults and shear due to strike-slip faults northeast of the Los Osos domain (e.g., the Rinconada, East/West Huasna). Our principal interest is in the former, but the latter are thought to have higher (though uncertain) cumulative slip rates and are probably larger than the uncertainties in the SAF corrections used in the SRT analysis. Assessing the deformation caused by the SLPB fault system using GPS data will require refined regional fault models with better constraints on the slip rates of the Rinconada, Huasna, and other active faults.

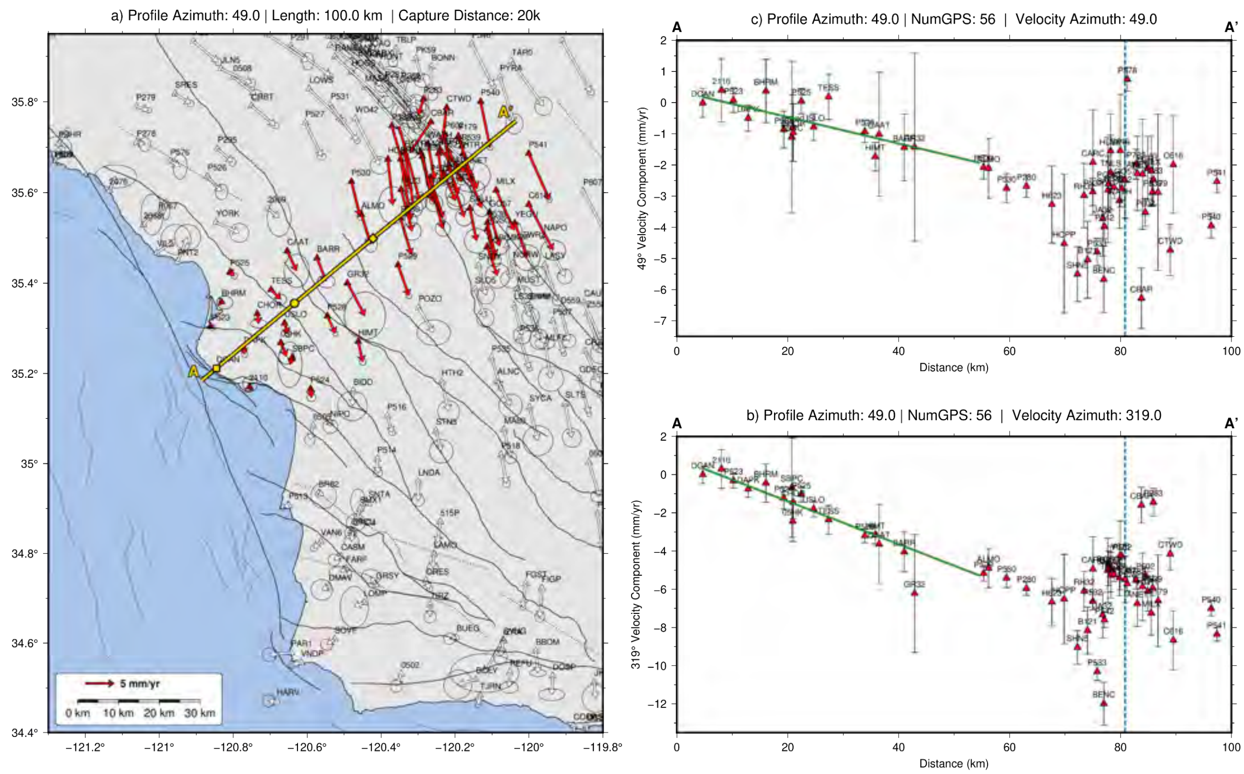

Figure 3.12. (a) Map showing the corrected Zeng GPS velocities relative to station DCAN (arrows). Gold line is the profile A-A' normal to the SAF. **(b)** Components of the red station velocities projected parallel to the SAF plotted at the distance along the profile. **(c)** Components of the red station velocities projected perpendicular to the SAF. Green lines on **(b)** and **(c)** are weighted least-squares fits to the red stations within 50 km of DCAN (Table 3.2). Plot conventions are the same as in Figure 3.7.

The regional model removes the interseismic deformation associated with the Hosgri-San Gregorio fault (Figure 3.9), but we used the SSC24 average slip rate for the Hosgri fault of 1.7 mm/yr along its entire length; therefore, some portion of the residual deformation could reflect unmodeled deformation along the Hosgri fault. The regional model has a simplified geometry, so the Hosgri-San Gregorio fault does not have the detail to include the fault stepovers observed in the geologic mapping and other local modeling studies (e.g., O'Connell et al. 2023). We performed a sensitivity analysis using the regional kinematic model with slip rates within the SSC24 Hosgri slip rate range of 0.6-3.0 mm/yr and found little impact on the final corrected GPS velocity field.

The SAF-normal projection of the corrected Zeng GPS data also looks notably different from the raw data (Figure 3.12c). Whereas the raw data indicate very little potential SAF-normal motion, the corrected data shows SAF-normal apparent contraction rate of –22 ± 12 nanostrain/yr over the 25-km baseline and –42 ± 7 nanostrain/yr over the 50-km baseline. Within this zone of apparent contraction, it is not possible to identify any clear zones of faulting because of the uncertainties in the data, the sparse GPS station spacing, and a regional contraction that is diffuse and likely distributed across many different faults with slow rates.

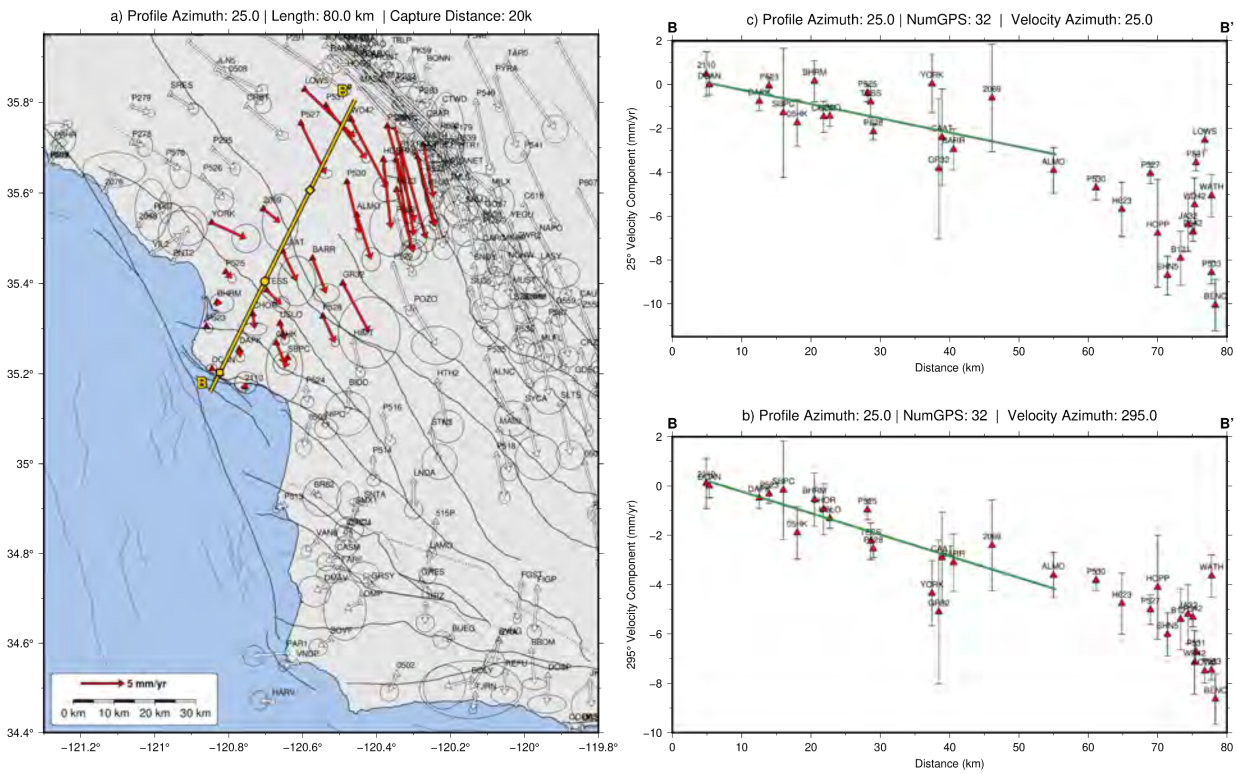

Figure 3.13. (a) Map showing the corrected Zeng GPS velocities relative to station DCAN (arrows). Gold line is the profile B-B' normal to the Southwest Boundary Zone (SWBZ). **(b)** Components of the red station velocities projected parallel to the SWBZ plotted at the distance along the profile. **(c)** Components of the red station velocities projected perpendicular to the SWBZ. Green lines on **(b)** and **(c)** are weighted least-squares fits to the red stations within 50 km of DCAN (Table 3.2). Plot conventions are the same as in Figure 3.7.

The SWBZ-normal profiles for the corrected GPS data (Figure 3.13 & 3.14) show higher SAF-normal strain rates, –59 ± 10 and –65 ± 8 nanostrain/yr averaged over the 25- and 50-km baselines. However, much of this contraction rate can be attributed to the 24º misalignment of the SWBZ profile with SAF-parallel shear, which projects the shear onto the linear contraction rate. For example, the misalignment projects an SAF-normal shearing rate of –100 nanostrain/yr onto a B-B' linear contraction rate of –40 nanostrain/yr (Figure B1).

We admit that any SWBZ-parallel contraction cannot be separated from SAF-parallel shearing using 1D profiles and therefore focus on the apparent contraction of the SAF-normal component averaged over the SWBZ-normal profile (Figure 3.14). Fitting the corrected SAF-normal velocities gives –19 ± 10 and –24 ± 7 nanostrain/yr averaged over the 25- and 50-km baselines (Table 3.3). In comparison, the same numbers derived from the uncorrected velocities yield a small but positive extension rate: +14 ± 10 and +17 ± 7 nanostrain/yr. Most of this difference comes from the extensional field imposed by the abrupt termination of the SAF creeping section, as described by the Titus et al. (2011) model of Figure 3.11.

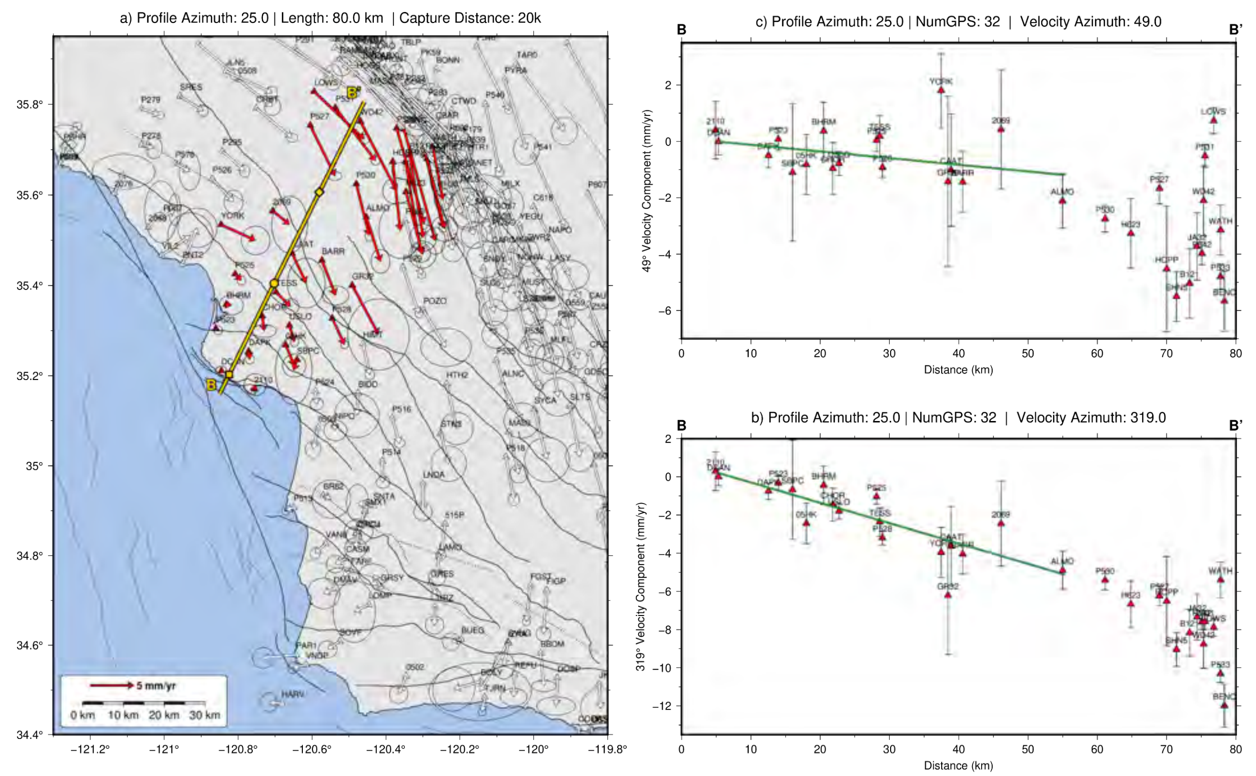

Figure 3.14. (a) Map showing the corrected Zeng GPS velocities relative to station DCAN (arrows). Gold line is the profile B-B' normal to the Southwest Boundary Zone (SWBZ). **(b)** Components of the red station velocities projected parallel to the SAF plotted at the distance along the profile. **(c)** Components of the red station velocities projected perpendicular to the SAF. Green lines on **(b)** and **(c)** are weighted least-squares fits to the red stations within 50 km of DCAN (Table 3.2). Plot conventions are the same as in Figure 3.7.

The residual contraction rates across the greater Irish Hills region thus depend strongly on the model of the San Andreas and other faults that are used to correct the data. The regional model used here to correct the data is a highly simplified representation of the plate-boundary fault system, and future efforts should aim to improve its accuracy.

Not all of the observed contraction reported here need be due to reverse faults. Strike-slip faults can also produce regional contraction when the slip and geometric characteristics are favorable. Unfortunately, the 1D profiles cannot directly resolve the fault slip rates on the regional faults due to a combination of the uncertainties being too large, station spacing being too sparse, and the deformation being distributed amongst several faults with relatively slow slip rates that all sum to produce the overall regional shortening. Block models of the region (e.g., Murray-Moraleda et al. 2011) were unsuccessful at resolving the details of slip rates on many of the faults of the greater Irish Hills region, likely because these faults are generally short, disconnected, have complex geometry and are therefore not easily represented by a block model. Future work could potentially use geodetic data to resolve regional slip rates if coupled with a detailed 3D kinematic or mechanical model of all regional faults using a geologically constrained fault geometry.

3.4.4. Strain Rate Inversion Method

During the interseismic period, active faults are expected to produce strains localized above their upper tip lines at the locking depth (e.g., Savage, 1983; Savage and Burford, 1970; 1973); therefore, mapping the distribution of strain in a region can be useful for identifying zones of deformation that could be related to active faulting (e.g., Zeng, 2022; Maurer & Materna, 2023). Here, we apply the strain rate inversion method of Marshall et al. (2013), which closely follows Allmendinger et al. (2007, 2009). Our inversion method provides a weighted least-squares fit to all data from stations in a specified region, and it weights each station velocity by its distance from the current grid point. This has the advantage of smoothing the resultant strain rate predictions, which can often be noisy.

Because strain rate is a tensor quantity, it is often preferable (especially for visualization purposes) to decompose the 2D (surface) strain rate tensor $\dot{e}_{ij}$ into so-called invariants that are scalars and are independent of the coordinate system. Here we focus here on two invariants that reveal key aspects of the strain rate patterns. The first invariant of the strain rate tensor,

$$I_1 = \dot{e}_{11} + \dot{e}_{22} \,,$$

quantifies the intensity of dilatation, or rate of change in area (i.e., zones of areal contraction vs. extension). Another invariant is the Euclidean norm, which quantifies the total strain,

$$\left\|\dot{e}_{ij}\right\| = \sqrt{\dot{e}_{11}^2 + \dot{e}_{22}^2 + 2\dot{e}_{12}^2} \,,$$

All inversions are performed on a regular grid with 2-km spacing. To minimize smoothing and show the local details, we utilize a smoothing length of 7 km, which is the smallest value that does not result in rank-deficiency errors during the inversion. The mathematical and mechanical limitations of strain inversion methods are discussed by Allmendinger et al. (2007) and Maurer & Materna (2023).

3.4.5. Regional Strain Rate Maps

Strain rate inversions of the raw and corrected GPS data show considerable spatial variability due to velocity uncertainties and non-elastic motions, which makes them difficult to interpret. The strain-rate maps from these inversions are given in Appendix B (Figures B.2-B.3). The strain-rate variations are rather noisy, although their strain rates averaged over profiles A-A' and B-B' are generally consistent with those from the gridded and smoothed strain-rate maps discussed below (Table 3.4).

Table 3.4. Strain rates from geodetic inversions averaged over the DCAN baselines.

Profile	GPS Dataset	25 km Dilatation Rate (10^{-9}/yr)	50 km Dilatation Rate (10^{-9}/yr)	25 km Total Strain Rate (10^{-9}/yr)	50 km Total Strain Rate (10^{-9}/yr)
A-A’	Raw	5 ± 27	35 ± 41	60 ± 8	80 ± 23
A-A’	Raw Gridded	17 ± 1	20 ± 4	77 ± 9	78 ± 8
A-A’	Corrected	-26 ± 22	-15 ± 23	72 ± 10	89 ± 22
A-A’	Corrected Gridded	-26 ± 3	-33 ± 8	66 ± 7	74 ± 10
B-B’	Raw	16 ± 36	37 ± 37	61 ± 10	69 ± 12
B-B’	Raw Gridded	18 ± 1	18 ± 1	75 ± 8	73 ± 8
B-B’	Corrected	-16 ± 31	-15 ± 29	72 ± 12	85 ± 17
B-B’	Corrected Gridded	-25 ± 3	-34 ± 10	65 ± 5	72 ± 9

A powerful method to improve strain rate inversions was proposed and implemented by Sandwell and Wessel (2016), which utilizes mathematical constraints from elasticity to interpolate GPS velocities onto a regular grid before inversion. Because the interpolation uses a 2D thin elastic plate approximation, the smoothing has a physical basis and can be effective at filtering out non-elastic motions, which are likely non-tectonic in origin. To grid the GPS data, we utilize *gpsgridder* (Sandwell and Wessel, 2016), implemented in the Generic Mapping Tools package, version 6 (Wessel et al., 2019) with a grid spacing of 0.05° × 0.05º. The gridded corrected GPS velocities have a smoother spatial pattern compared to the corrected station velocities (see Figure B.3). We then invert the gridded uncorrected and corrected velocities for strain rates using the same methodology and parameters as previously described.

The inversion of gridded uncorrected GPS velocities shows extensional dilatation throughout the greater Irish Hills region and much larger values of total strain associated with the SAF (Figure 3.15). This regional extension is similar to the SAF interseismic deformation that was shown by Titus et al. (2011), but here we show that this SAF-related extension extends to DCPP and significantly affects geodetic measurements throughout the greater Irish Hills region. There is an increase in total strain near the 2003 San Simeon earthquake, suggesting that Zeng (2022) may not have removed all postseismic effects due to this event. The rates of dilatation and total strain are listed in Table 3.4 for all strain rate inversions averaged along the SAF-normal and SWBZ-normal profiles. In all cases, the along-profile total strain rates are significantly larger than dilatation rates.

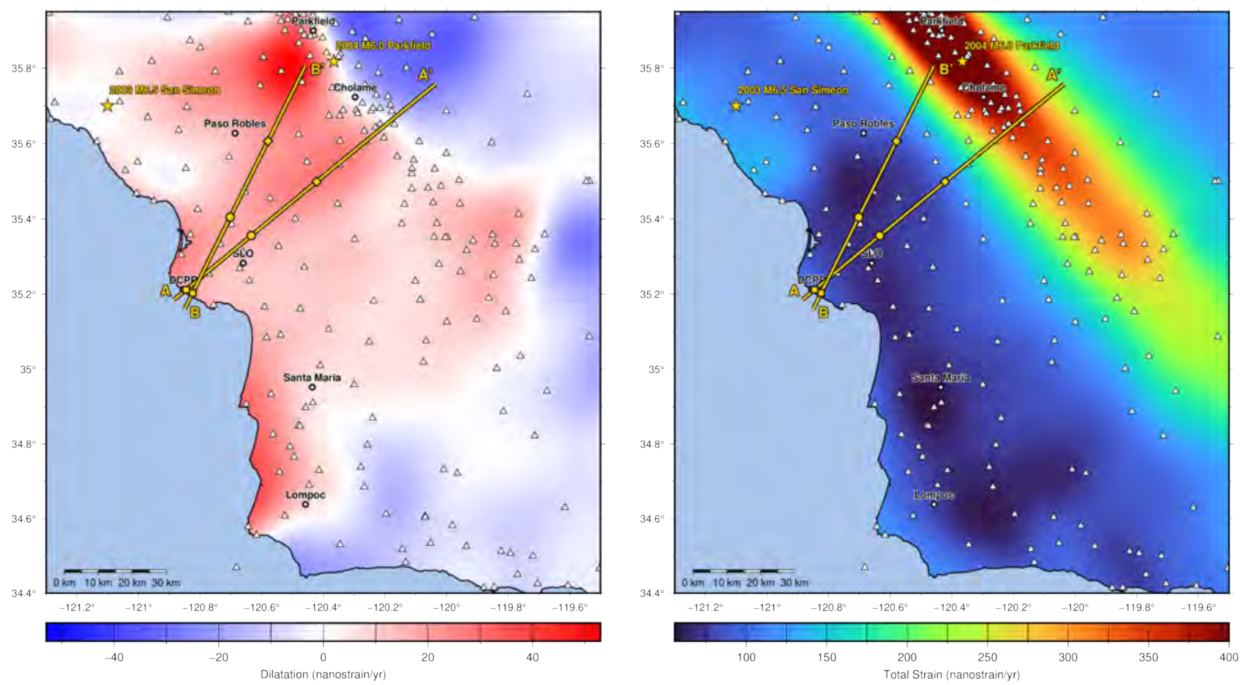

Figure 3.15. Strain rate inversion of the gridded raw Zeng GPS velocities plotted as dilatational and total strain rate components. The color scale for the total strain colors saturates at 400 nanostrain/yr, although the values exceed 600 nanostrain/yr near Parkfield. The SAF-normal and SWBZ-normal profiles are shown with along-profile locations of station DCAN (square) and 25 km (circle) and 50 km (diamond) away to the northeast. The overall pattern of dilatation is extensional throughout the greater Irish Hills region.

Inversion of the gridded corrected GPS velocities shows significantly different patterns of dilatation and total strain rate (Figure 3.16). While most of the deformation related to the SAF has been removed, we still see significant strain rate concentrations near Parkfield and near the San Simeon event. The data now consistently indicates contractional dilatation rates from Cholame to DCPP. The faster rates near Cholame are likely due to unmodeled San Andreas slip or postseismic effects from the 2004 Parkfield earthquake. The inversions of the gridded corrected GPS data suggest several regions of total strain of approximately 100 nanostrain/yr (green zones in Figure 3.16). These zones appear to more closely follow known regional strike-slip faults, and these zones are more south-trending than we would expect to be associated with a single reverse fault.

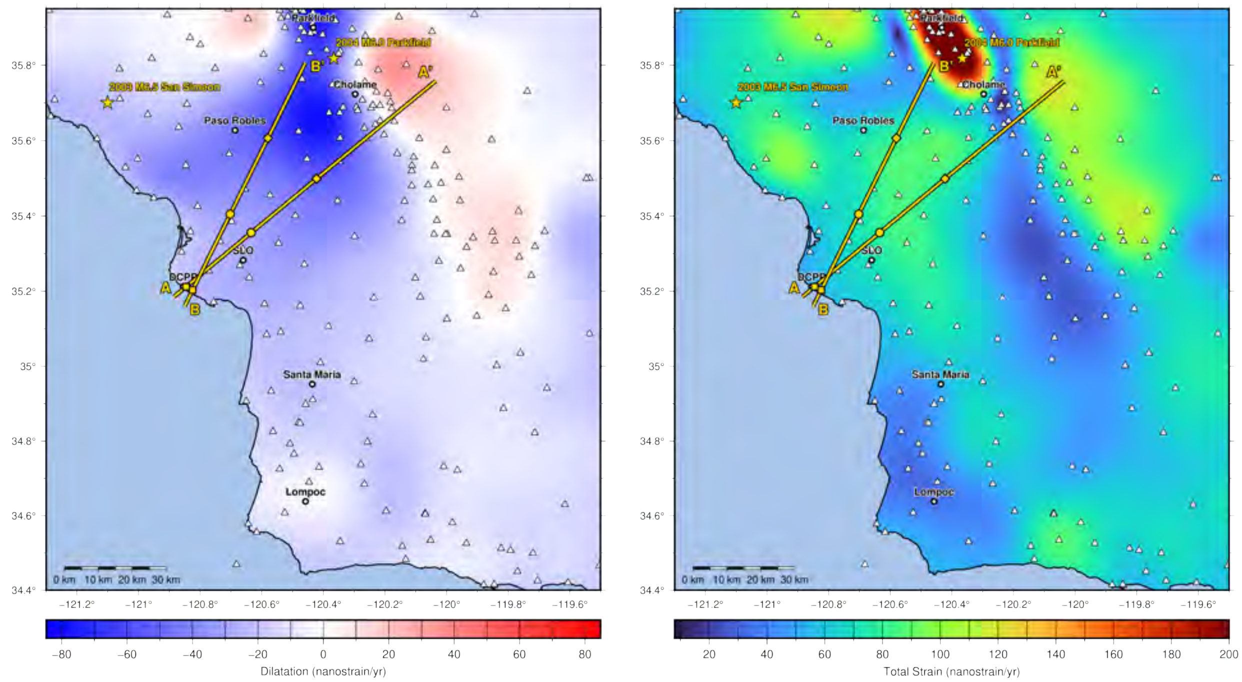

Figure 3.16. Strain rate inversion of the gridded corrected Zeng GPS velocities plotted as dilatational and total strain rate components. The color scale for the total strain colors saturates at 200 nanostrain/yr, although total strain exceeds 260 nanostrain/yr near Parkfield. After removal of the SAF and other regional faults, the data now show contractional dilatation throughout the greater Irish Hills region. Labeled features are the same as in Figure 3.15.

3.4.6. Strain Predicted by Kinematic Dislocation Models

To evaluate whether any of the observed strain rate patterns can be potentially associated with SWBZ faults in the SSC, as well as a 25° dipping fault similar to that proposed by Dr. Bird, we run several simplified kinematic dislocation models with different subsurface fault geometries, all using a Poisson's ratio of 0.25. These models are 3D, and the surface strain rates are calculated analytically using the polygonal dislocation modeling code, *poly3D* (Thomas 1993). Modeled fault traces are all planar and identical, but they have different subsurface geometries. We test three models. The first is similar to the shallow dipping model proposed by Dr. Bird with a constant subsurface dip of 25°. The second model dips at a constant 40°, which is our best estimate for SWBZ near-surface dip. The third model is a ramp-flat-ramp model that was discussed in §3.3.2 and has an upper ramp dipping at 40°, a flat, horizontal section at 8.4 km depth, and a lower ramp dipping at 30° (Figure 3.5). This ramp-flat-ramp geometry is simplified, but generally kinematically consistent with the first order fold structure of the Pismo Syncline and zones of uplifted marine terraces (see §3.3.2 for details). We use the model-calculated strain rate tensor components to calculate dilatational and total strain rate components. In all models, we apply a slip rate of 2.5 mm/yr to simulate a rate near the upper bound of Dr. Bird's suggested fault slip rates for potential thrust faulting beneath the Irish Hills, but we note that changing the slip rate will not change the patterns of deformation, only the rates. Because strain rates are linearly related to slip rate, model results can be easily adapted for other slip rates.

We simulate both 12 and 15 km locking depths, consistent with the SSC15 and SSC24. All models produce similar geometric patterns of strain, so we focus our discussion on the 25° dipping model with a 15 km locking depth, which most directly addresses the Bird's hypotheses. Shallower locking depths increase the strain rate magnitudes, localize the deformation over a smaller area, and shift the deformation a few km to the southwest. The model-predicted strain rates for a 15 km locking depth are shown in Appendix B.

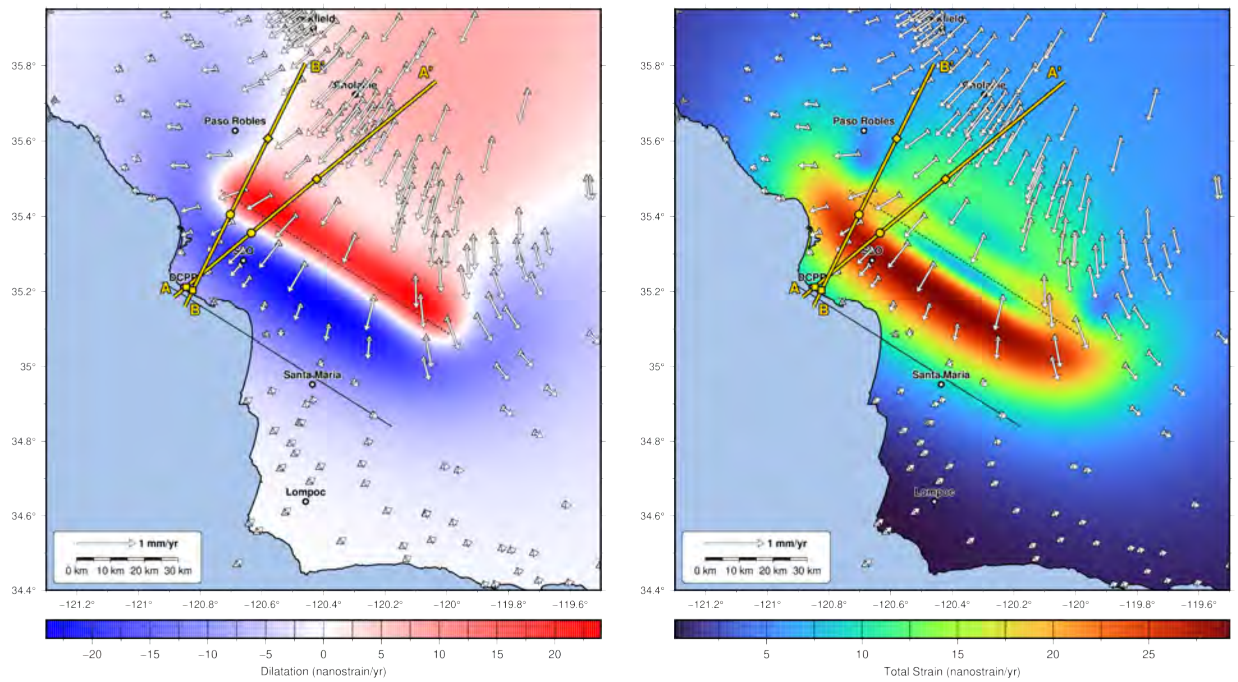

Figure 3.17. (a) Dilatational and **(b)** total strain rates from a 3D kinematic dislocation model utilizing a 15 km locking depth and a 25° dipping fault with 2.5 mm/yr of slip similar to the shallow-dipping fault proposed by Dr. Bird. Model results have been cropped to only show onshore strain rates. Solid black line is the surface trace of the modeled fault; dashed line shows the fault location at the locking depth. Zones of fastest strain rate are northeast of the fault trace at a distance that depends on fault dip and locking depth. White arrows show the model-predicted velocities at the GPS stations. The model-predicted velocity gradients are small compared to the GPS velocity uncertainties. The SAF-normal (A-A') and SWBZ-normal (B-B') profiles are shown with a gold line with the along-profile locations of station DCAN (square), 25 km from DCAN (circle), and 50 km from DCAN (diamond).

The 25° dipping model produces a zone of strain that is offset from the fault trace due to the dip of the fault (Figure 3.17). Directly to the northeast of the fault location at the locking depth (the dashed line on Figure 3.17) there is a zone of extension, while to the southwest there is a zone of contraction. The total strain is mostly focused to the northeast of the fault trace with some minor strain to the northeast of the fault's projection at the locking depth. The zones of localized strain for the 25° dipping model cover a portion of the Irish Hills, but are most focused to the northeast, including near the San Luis Obispo. For the steeper (40°) dipping model (Appendix B, Figure B.6), the strain rate patterns are similar to the 25° dipping model, but generally narrower or more localized in the northeast-southwest direction and are shifted to the southwest due to the steeper fault dip. Although the ramp-flat-ramp model has a more complex subsurface fault surface geometry, below the 12 and 15 km locking depths, the fault is planar and dips at 30°, resulting in similar predicted interseismic strain rate patterns, but they offset to the northeast compared to the other models (Appendix B, Figure B.7).

In comparing the predicted strain rates, we see that all models generally produce dilatational and total strains near the fault at the locking depth with magnitudes of 20-35 nanostrain/yr. The strain rate inversions of the GPS data involve a sparse spacing and noise that may hide a such a strain signal. The inversion of the gridded, corrected GPS data shows a region of contraction northeast of the Irish Hills, but we do not see a zone of reduction in dilatation predicted by the models. To determine if the current GPS network has adequate spatial resolution to resolve the model-predicted patterns, we invert the model predictions at the locations of the GPS stations (Figure 3.18). The inversion reproduces the spatial pattern, albeit with lower strain rate magnitudes (as expected for any strain-rate inversion), indicating that the current GPS network has sufficient spatial coverage to be able to resolve the SWBZ faulting, but that reduced uncertainties will be needed to detect active faulting. The model-predicted velocities plotted along the SAF-normal profile are small compared to the GPS velocity gradients and uncertainties (Appendix B, Figure B.8).

3.4.7. Conclusions Regarding Regional Strain Rates

Table 3.3 summarizes the velocity gradients for the two 1D profiles averaged over DCAN baselines of 25 km and 50 km. The uncertainties are large (~10 nanostrain/yr), but the four SAF-normal estimates from the corrected Zeng data are negative (contractional) and span the range from –19 to –42 nanostrain/yr (average = –27 nanostrain/yr). For comparison, Table 3.4 lists the dilatational and total strain rates from the 2D inversion models averaged over the same 1D baselines. The estimates with the smallest uncertainties come from the corrected gridded inversions, which are also all negative (contractional) and have values from –25 to –34 nanostrain/yr (average = –30 nanostrain/yr). The consistency of the velocity-profile estimates with the strain-rate inversions suggests that (a) the SAF-normal contraction rates are reliable and (b) the dominant deformation in the SAF-parallel direction is simple plate-boundary shear. Overall, the profile analysis and strain-rate maps show that the deformation of the greater Irish Hills region is characterized by SAF-parallel shear and a smaller SAF-normal contraction, in general agreement with the 70% strike-slip and 30% reverse faulting assumed by PG&E in the Local Areal Source Zone of the SSC.

We note there are situations where active faulting does not produce detectable geodetic signals. For example, Marshall et al. (2013) discuss several reverse faults in the western Transverse Ranges of southern California that do not extend to sufficient depth to produce interseismic deformation. Similar faults within the Irish Hills, should they exist, would not be detectable even with much improved geodetic data.

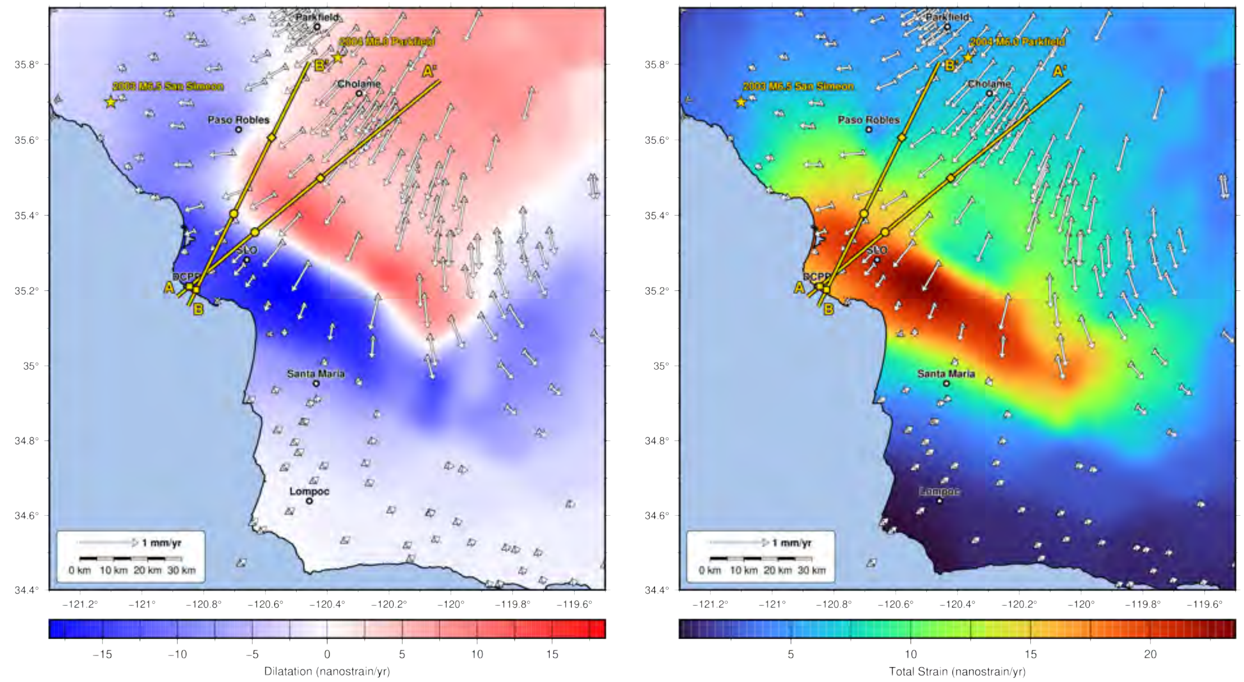

Figure 3.18. (a) Dilatational and **(b)** total strain rates inverted from predictions of velocity only at the GPS stations (white arrows) from the 25° dipping model with a 15 km locking depth. While these inverted strain rates are smaller than the exact analytical model predictions, the overall spatial pattern of strain is well-reproduced.

3.5. Analysis of the 2024 Noto Peninsula Earthquake

Dr. Bird has nominated the January 1, 2024, Noto Peninsula (Japan) earthquake (**M**7.5), abbreviated Noto24, as the characteristic event in a time-independent recurrence model of the DCPP hazards from thrust earthquakes beneath the Irish Hills. He combines the mean Noto24 slip, taken to be 2 m, with his estimates of thrust-fault slip rates beneath the Irish Hills, which range from 2.0 to 2.8 mm/yr, to obtain a recurrence interval (return period) of 715-1000 yr for what he calls "great thrust earthquakes under the Irish Hills."

3.5.1. Earthquake Characteristics

The Noto24 earthquake was caused by reverse faulting (and a minor component of strike-slip), which nucleated near the northern end of the Noto Peninsula and ruptured bilaterally for 150 km across multiple fault segments parallel to the coastline (Figure 3.19). The dip angles of the segments varied from ~60º in the northeast to ~40º in the southwest, averaging about 45º (Fukushima et al., 2024). The slip was confined to the seismogenic layer above 15 km depth, resulting in a total fault area of approximately 3180 km^2.

Noto24 was an unusual earthquake in two notable respects. First, its rupture length (150 km) was seven times larger than its rupture width (15 km ÷ sin 45º = 21 km). A fault aspect ratio of 7 lies outside the range observed for interplate dip-slip earthquakes of this width, which have an average aspect ratio of about 2 (Figure 3.20). Second, Noto24 was a high stress drop earthquake with an average slip of about 4 m, twice that typical for interplate dip-slip earthquakes of similar magnitude (Xu et al., 2024) and twice the slip assumed by Dr. Bird. Stress drops across the largest asperity were as high as 40 MPa, about four times that for typical asperities in Japanese crustal earthquakes (Xu et al., 2024; Ma et al., 2024). Xu et al. (2024) conclude that the elongated Noto24 rupture was driven by the energy released during the breaking of large, highly stressed asperities. The high stress drop also generated very strong ground motions (intensity 7 on the Japanese scale) with peak ground velocities as high as 145 cm/s and peak ground accelerations over 2.6 g (Chen et al., 2025).

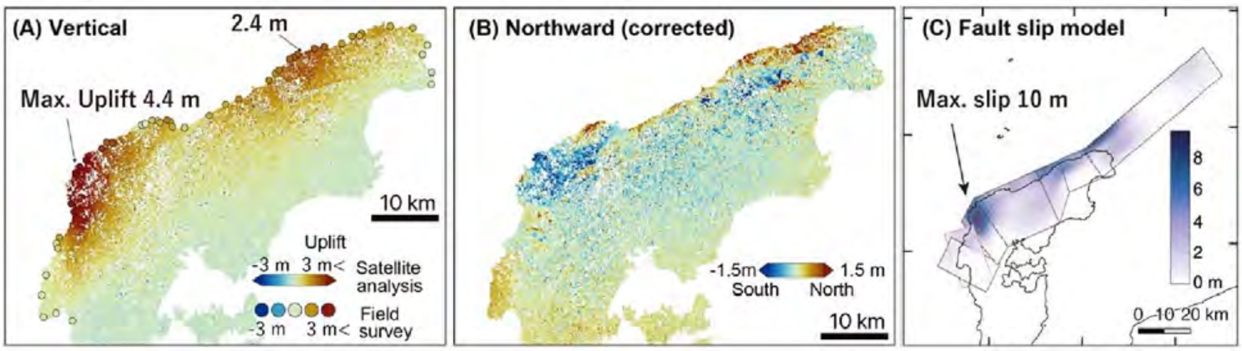

Figure 3.19. Maps of the Noto Peninsula showing (A) vertical component of deformation from synthetic aperture radar (SAR) image analysis (colored pixels) and coastal field survey (filled circles), (B) North-south component of deformation from SAR image analysis. (C) Fault-slip model from a joint inversion of GNSS data and SAR pixel offset data. [Source: Fukushima et al. (2024), fig. 2.]

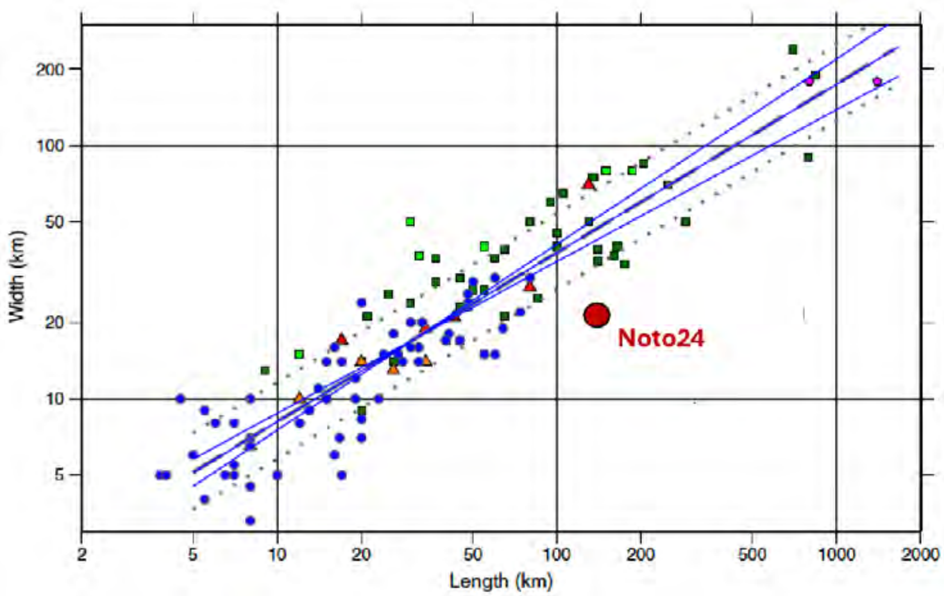

Figure 3.20. Width versus length for normal and reverse dip-slip interplate faults compiled by Leonard (2010); lines are from his scaling analysis. The least-squares estimate (dashed line) has a slope of 0.668. Points with different symbols and colors are from different published catalogs (see Leonard, 2010, fig. 1 for key). The Noto24 rupture (large red dot) has a very high aspect ratio (~7), which has been attributed to the energetic rupturing of multiple strong asperities. [Source: Leonard (2010), fig. 1.]

The Noto24 fault displacements resulted in large co-seismic uplifts that are well documented by synthetic aperture radar (SAR) imaging and field studies (Figures 3.19a and 3.21). The uplift along the northern coastline of the peninsula averaged about 2 m, and it peaked at 4.4 m on the southwestern end, near the maxima fault slip of ~10 m obtained from the finite source inversions (Fukushima et al., 2024; Xu et al., 2024; Ma et al., 2024). The strong correlation between fault slip and uplift (Figure 3.19) supports the hypothesis that uplift can be used as a proxy for fault displacement.

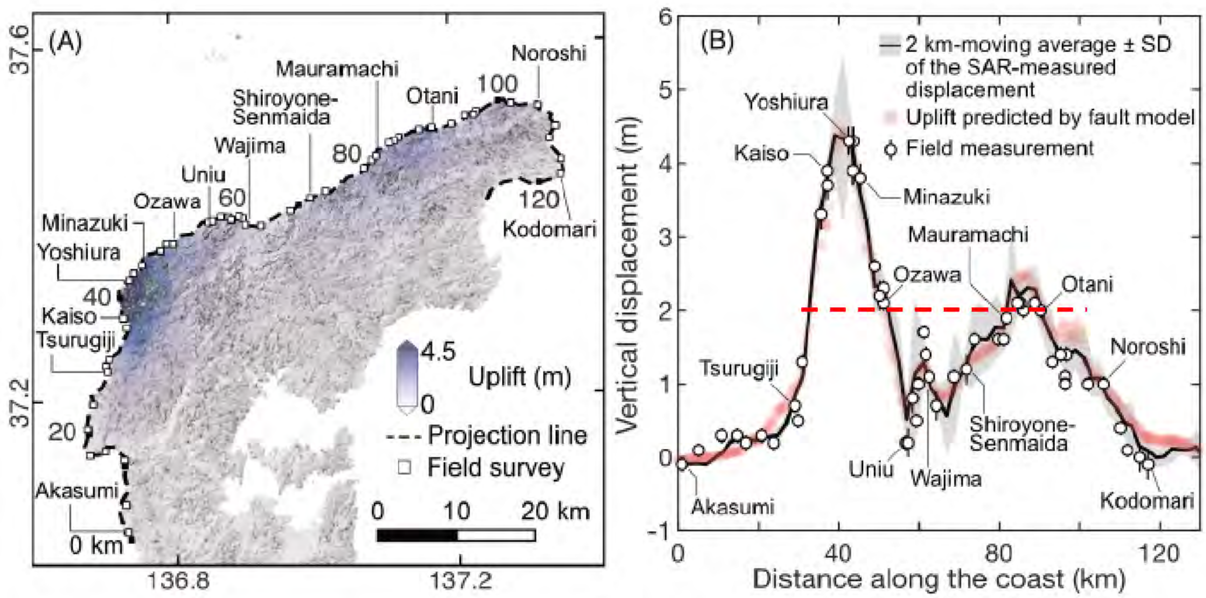

Figure 3.21. Comparison of vertical displacements of SAR and field measurements along the coastline of the Noto Peninsula. (A) Vertical displacement derived from the SAR pixel offset analysis and sites of a field survey. (B) Vertical displacement along the coastline. The numbers in (A) indicate the distance along the coastline used in the projection (B). Red dashed line shows an uplift of 2 m, which approximates the average observed between the towns of Tsurugiji and Noroshi. [Source: Fukushima et al. (2024), fig. S14 (annotated).]

3.5.2. Uplift and Tilting of the Noto Peninsula

The mapping of Holocene marine terraces and other shoreline features indicates that faulting beneath the Noto Peninsula is uplifting the northern coastline at a rate of 0.9-1.5 mm/yr (Shishikura et al., 2009, 2020). The uncertainty range for this rate is primarily due to the lack of age control on all but the lowest emergent shoreline features, each corresponding to < 1 m uplift events. Elevations of the MIS 5e terrace over this same span of coastline range from 85 to 124 m (Koike & Machida, 2001), yielding a coastal uplift rate of 0.7-1.0 mm/yr. We adopt the latter for recurrence interval calculations because it is more directly comparable to the uplift rate for the Irish Hills, which was derived from the same MIS 5e terrace.

The uplift decreases across the peninsula, resulting in the long-term tilting of the Noto block to the south-southwest. This tilting is evident in the LCI topographic profile (Figure 3.22a) and consistent with the Noto24 co-seismic uplift (Figure 3.19a). The consistency indicates that repeated ruptures of the Noto24 fault system are responsible for the uplift and tilting of the Noto Peninsula over the past hundred thousand years (Masuda et al., 2024; LCI, 2024). A similar tilting is not as evident in the Irish Hills, where the LCI topographic profile is more symmetric about its peak (Figure 3.22b). This may indicate different fault configurations—a single ramp or listric fault beneath Noto Peninsula (Liu et al., 2024, fig. 10) vs. fault ramp bending to flat fault at intermediate seismogenic depths (7-8 km) beneath Irish Hills (Figure 3.5).

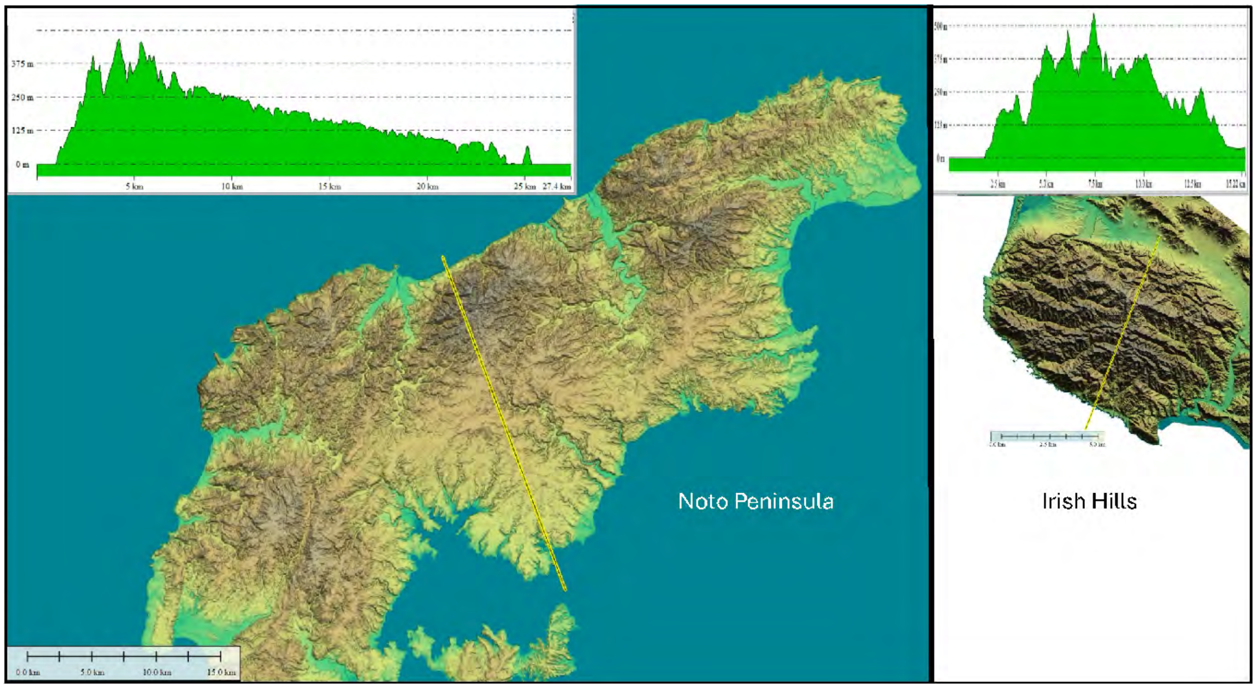

Figure 3.22. Topographic expressions of uplift of the Noto Peninsula (left) and the Irish Hills (right). Cross sections (yellow lines) are oriented perpendicular to the strike of the offshore reverse faults. The horizontal and vertical scales of the two maps are the same. [Source: LCI (2024), fig. 12 (rescaled).]

3.5.3. Maximal Earthquake Recurrence Model

The USGS moment magnitude of Noto24, $\mathbf{M}_{\text{Noto24}} = 7.5$, corresponds to a moment release of $M_0^{Noto24} = 2.24 \times 10^{20}$ Newton-meters (Nm). The simplest method for estimating recurrence rates of earthquakes that fully rupture a system of faults is to apply the *maximal earthquake recurrence model*, which assumes that all slip on the causative faults is due to the recurrence of Noto24-type events. The SSC15 report refers to this assumption as "the simplified maximum magnitude" model, and it is the same model used in Bird's recurrence rate calculations. The recurrence model is maximal because it stipulates that no larger events can occur within the fault system and it completely ignores the smaller events. The maximal earthquake model thus represents an extreme version of Youngs & Coppersmith's (1985) characteristic earthquake model.

For the model to be useful in seismic hazard analysis, the characteristics for identifying a Noto24-type event need to be specified. The SRT defines a 'Noto24-type event' to be a **M**7.5 earthquake that ruptures a 'similar' system of reverse faults; i.e., a set of faults of similar overall length (~150 km), width (~21 km), rake (~90º), and dip (~45º).

Under the assumption that uplift rate is proportional to the fault displacement rate, the maximal earthquake model calculates the recurrence interval of Noto24 by dividing the average Noto24 uplift by the Noto Peninsula uplift rate. Using 2 m for the former (Figure 3.20) and the rate range given by Shishikura et al. (2020) for the later yields,

Noto24 recurrence interval (Noto Peninsula) = 2 m ÷ (0.7-1.0) mm/yr = 2,000-2,900 yr

Dr. Bird proposes Noto24 as the maximal earthquake appropriate for estimating the recurrence interval of large thrust faulting beneath the Irish Hills. The Irish Hills uplift rate is nearly ten times smaller than the Noto Peninsula rate. Assuming the uplift ratio is proportional to the slip-rate ratio for the two regions, the maximal earthquake model gives:

Noto24 recurrence interval (Irish Hills) = 2 m ÷ (0.12-0.24) mm/yr = 8,300-16,700 yr

This range, based on the observed uplift rate of 0.18 ± 0.03 mm/yr, is an order of magnitude greater than the range of 715-1,000 yr calculated by Dr. Bird from his slip rates (Table 3.4).

3.5.4. Characteristic Earthquake Model

The recurrence interval given by the maximal earthquake model is a lower bound, because the model ignores the uplift from smaller earthquakes in the magnitude-frequency distribution (MFD). The Noto Peninsula displays a high rate of historical seismicity with many documented events in the magnitude interval $M6.0 - 7.0$. Large earthquakes occurred on February 7, 1993 (M_{JMA} 6.6)[4] near the northeastern end of the Noto Peninsula of the 2024 event and on March 25, 2007 (M_{JMA} 6.9) near the southwestern end. The later event generated vertical deformation up to 50 mm, similar to two earlier coastal emergence events in this area (Shishikura et al., 2009). On May 5, 2023, a M_{JMA} 6.5 earthquake occurred as part of a precursory swarm at the north end of the peninsula. Additional seismicity includes a M_{JMA} 6.4 earthquake on December 9, 1892, and two M_{JMA} ~ 6.9 earthquakes in 1729 and 1815. Because these smaller earthquakes happen much more frequently than Noto24-type events, they add significantly to net coastal uplift, and a valid recurrence model must account for their contribution.

For this purpose, the SRT adopts the Youngs & Coppersmith (1985) characteristic earthquake model, illustrated in Figure 3.23. The MFD has two components, a Gutenberg-Richter (GR) distribution with a *b*-

[4] M_{JMA} is the magnitude scale used by the Japanese Meteorological Agency. The JMA magnitude for Noto24 is 7.6.

value of unity truncated at a characteristic (also maximum) magnitude $\mathbf{M}_C$. This truncated GR distribution is uniquely specified by the rate of the maximum-magnitude event, denoted λ_{GR}. Integrating the seismic moment over the distribution gives the total moment rate

$$\dot{M}_0^{GR} = 2\lambda_{GR} M_0^C$$

Hence, the rate of moment release by a GR distribution truncated at $\mathbf{M}_C$ (solid line in Figure 3.23) is twice the rate due to the recurrence of the maximum earthquake (open circle in Figure 3.23). Superposed on this cumulative GR distribution is a step distribution (Heaviside function) of size $(\lambda_C - \lambda_{GR})$ at $\mathbf{M}_C$, which raises the rate of the characteristic events to λ_C (closed circle in Figure 3.23),

$$\dot{M}_0^C = \lambda_C M_0^C$$

Combining the two yields a total moment release rate of

$$\dot{M}_0^T = (\lambda_C + \lambda_{GR}) M_0^C$$

This characteristic recurrence model has two parameters, λ_{GR} and λ_C, and their ratio measures the relative size of the characteristic peak in the incremental MFD. The maximal earthquake recurrence model corresponds to the limit $\lambda_{GR}/\lambda_C \to 0$. The opposing limit is the truncated GR model, where $\lambda_{GR}/\lambda_C \to 1$.

The SRT has not done a formal seismicity analysis, but the high rate of events appears to be consistent with the hypotheses that Noto Peninsula earthquakes follow a truncated GR MFD with a *b*-value near unity. A GR distribution with $b = 1$ implies that there should be, on average, 10 events in the magnitude range $6.5 - 7.5$ during one Noto24 recurrence interval, which is 2000 yr or more. At least six events of this size have been documented for the last 200 years. Hence, the extrapolation of the GR MFD to a **M**7.5 rate is consistent with the Noto24 recurrence interval, which implies $\lambda_{GR}/\lambda_C \approx 1$, and $\dot{M}_0^T = 2\lambda_C M_0^C$. The GR model doubles the uplift and the recurrence interval:

Noto24 recurrence interval (Noto Peninsula) = 4 m ÷ (0.7-1.0) mm/yr = 4,000-5,700 yr

This estimate agrees with Masuda et al. (2024), who concluded that "tectonic geomorphology investigations on uplifted marine terraces along the northern Noto Peninsula suggest that the 2024 earthquake was a rare event occurring once every several thousand years."

Employing Noto24 as the characteristic earthquake ($\mathbf{M}_C = \mathbf{M}_{Noto24}$) and applying the GR recurrence model to the Irish Hills also doubles the recurrence interval:

Noto24 recurrence interval (Irish Hills) = 4 m ÷ (0.12-0.24) mm/yr = 16,700-33,300 yr

The recurrence interval estimates are summarized in Table 3.4, which also includes the estimates for the intermediate value, $\lambda_{GR}/\lambda_C = 0.5$. Given the seismicity evidence, the SRT judges that the GR model ($\lambda_{GR}/\lambda_C = 1$) provides the best estimate of the recurrence interval for Noto24-type earthquakes beneath the Noto Peninsula. If it is presumed that Noto24-type earthquakes can also occur beneath the Irish Hills, then the uplift data constrain the recurrence interval to be 16,700-33,300 yr, which is about 20 times greater than the range obtained by Dr. Bird. However, the presumption that a Noto24-type earthquake could occur in this region is questionable.

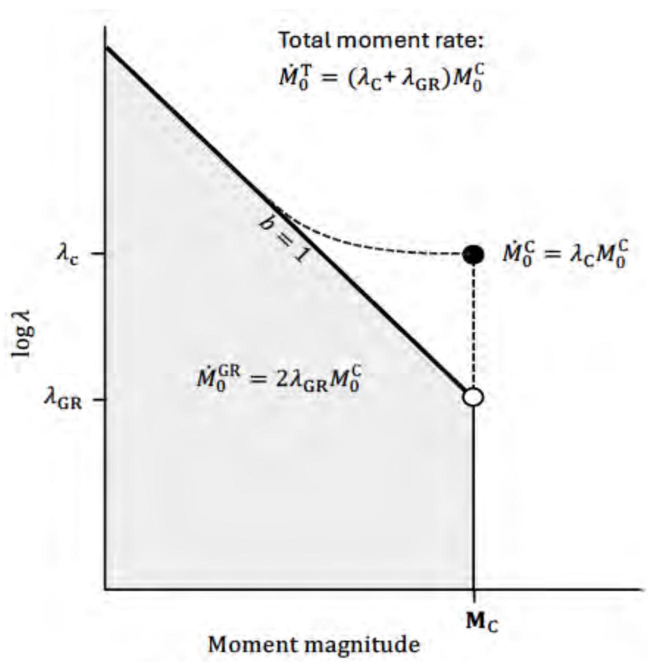

Figure 3.23. Characteristic earthquake model used in the recurrence analysis showing the cumulative distributions for the truncated GR component (solid line) and the total MFD (dashed line). This is the Youngs & Coppersmith (1985) model in the limit where all characteristic earthquakes have the same magnitude $\mathbf{M}_C$ and the characteristic peak in the incremental distribution is a delta function of strength $\lambda_C - \lambda_{GR}$. The open circle shows the characteristic part of the GR component, and the solid circle shows the total characteristic component. The integrated moment rate of the GR component is twice the GR characteristic part, and the total moment rate equals the sum of two characteristic parts.

Table 3.5. Estimates of Noto24 recurrence intervals based on uplift data

Recurrence model	λ_{GR}/λ_C	Noto Peninsula (yr)	Irish Hills (yr)
Bird (2024)	0	–	715-1,000
Maximal earthquake	0	2,000-2,900	8,300-16,700**
Characteristic earthquake	0.5	3,000-4,290	12,500-25,000**
Gutenberg-Richter*	1	4,000-5,700	16,700-33,300**

*Preferred model **95% CI

3.5.5. Tectonic Similarities and Differences

Dr. Bird bases his case for Noto24 on the tectonic similarities between the Noto Peninsula and the Irish Hills (§2.4d). Several studies of the Bird critique have pointed out the tectonic differences (Madugo & Kottke, 2024; LCI, 2024; NRC, 2025). The main features identified in these reports and the SRT analysis can be summarized as follows:

(a) The uplift rate of the Noto Peninsula is five times faster than that of the Irish Hills.

(b) Historical rate of large earthquakes ($M \geq 6$) is much greater in the Noto region than in the SLPB region (NRC, 2025).

(c) Tectonic deformation of the Noto Peninsula is compressional with little shear, whereas SLPB deformation is transpressional with a significant component of shear, as indicated by earthquake focal mechanisms and geodetic analysis (§3.4).

(d) The length of the Noto Peninsula fault system is about twice that of the SWBZ (Figure 3.24).

(e) The tilting of the Noto Peninsula occurs on a larger scale than the Irish Hills (Figure 3.22), suggesting a single, large fault ramp or listric fault underlies the Noto Peninsula. Block-like uplift of the Irish Hills is more restricted, suggesting a fault ramp that bends to flat at an intermediate depth within the seismogenic zone (§3.3)

(f) Large, prominent fault scarps have been mapped offshore of the Noto Peninsula; no prominent scarps are seen offshore of the Irish Hills (§3.3).

Bird's Noto24 analogy posits that a Noto24-type event on a reverse fault system comprising the Irish Hills has an exceedance probability worth considering—it is a "plausible rupture". One strong criterion is geometric compatibility: the Noto24-type rupture must be representable as slip distributed on an interconnected system of reverse faults, either known or postulated, with similar overall dimensions as Noto24. The most likely fault system for hosting the largest reverse-slip earthquakes in the vicinity of DCPP is the SWBZ, which has a similar dip and projected width. However, the along-strike length of the SWBZ is only about 65 km, less than half the length of the Noto24 rupture (Figure 3.24). Increasing the length requires crossing the faster-slipping Hosgri fault zone to the west or the Oceanic-West Huasna fault zone to the east. It is unlikely that a single rupture plane would cross the Hosgri fault, which truncates the SWBZ and its associated zone of folding and uplift. The rupture plane could plausibly extend 50 km further to the southeast, beneath the Rafael Range (as in the **M**7.4 SW-07 rupture of SSC24), but even this added fault length falls well short of the Noto24-type rupture extent.

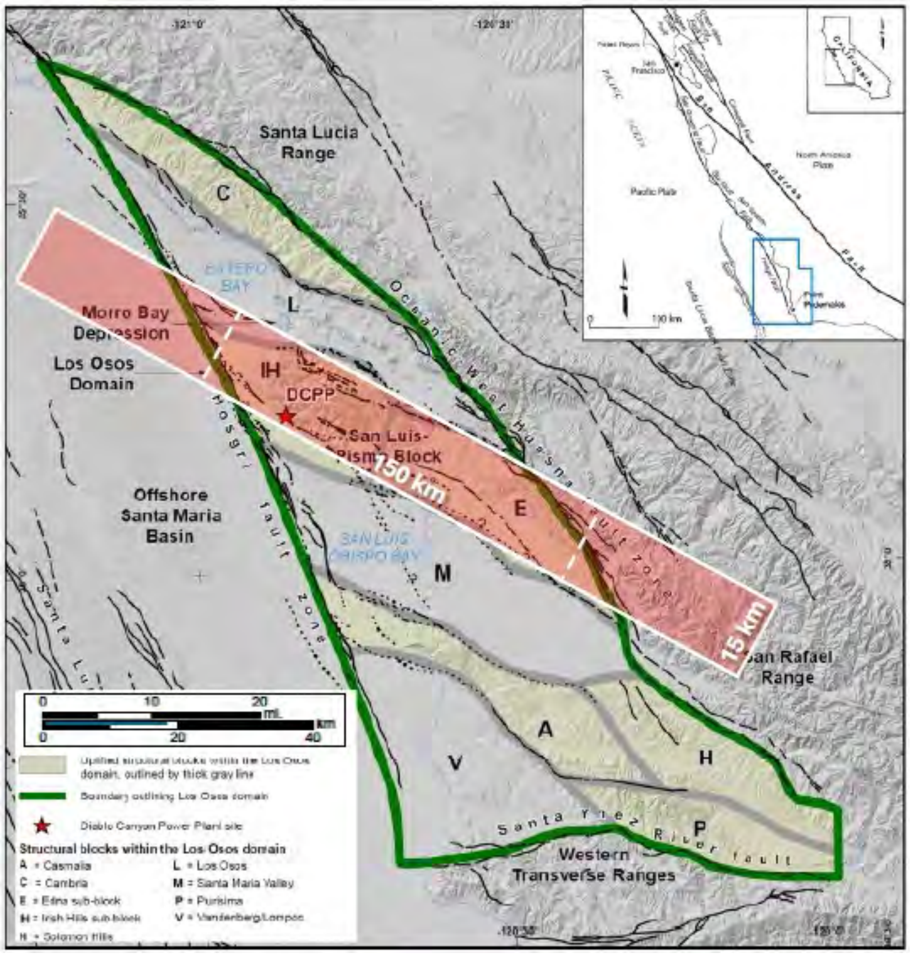

Figure 3.24. PG&E map of the Los Osos domain superposed with a rectangular area (red) that has the same dimensions as the surface projection of the Noto24 rupture (150 km × 15 km). The rectangle has been positioned to maximally include the uplifted San Luis-Pismo Block. The total area of the SLPB is ~1200 km^2, about half of the Noto24 surface projection (2250 km^2). [Source: SSC24 report, fig. 22 (annotated).]

4. Findings and Recommendations

In his critique, Dr. Bird has focused on the magnitudes and rates of thrust earthquakes beneath the Irish Hills, which he argues are underestimated in the SSC24 model. He has called into question the PG&E assumptions about fault dip, and he has applied a shallow-thrust model to estimate fault slip rates of 2.0-2.8 mm/yr. Using these rates, he has obtained recurrence intervals of 715-1,000 yr for a **M**7.5 Noto24-type earthquake beneath the Irish Hills.

The SRT has provided a point-by-point evaluation of Bird critique in the annotated summary of Section 2. In Section 3, we have conducted technical analyses of five specific issues central to the critique. This section summarizes our findings and recommendations.

4.1. Bird's Critique of PG&E Modeling Assumptions

According to Dr. Bird, "one of the reasons that the SSC15 and SSC24 reports seriously underestimated seismic hazard due to thrust faulting is that they were guided by four assumptions that are actually false (§2.1a) … Each time a false assumption in the PG&E SSCs was removed, thrust-faulting activity (seismic potency rate) in the Irish Hills went up by a large factor (§2.4a)."

The SRT has evaluated Bird's arguments by asking three questions about each of his four assumptions: Is the assumption, as stated, true or false? Was the development of the SSC models guided by the assumption? Would removing this guidance be impactful on DCPP hazard assessments by increasing the thrust-faulting component by a significant factor? The SRT's answers are listed in Table 4.1. All four assumptions are false, as stated by Dr. Bird. However, it does not appear that PG&E was actually guided by these assumptions in its source modeling.

Table 4.1. Evaluation of Bird's False Assumptions

Assumption	Truth value	Assumed by PG&E?	Impactful?
1. The Irish Hills are uplifting as a rigid block, with no internal deformation	false	no	no
2. Active thrust faults may dip at any angle	false	no	no
2a. Active reverse faults may dip more steeply than 45º	true*	yes	yes
3. Geologic structures older than ~0.33 Ma are irrelevant to seismic hazard estimation	false	no	no
4. GPS geodetic velocities are not useful for site-specific seismic hazard estimation	false	yes	no
* Bird deems this assumption to be false; evidence that it is true is given in §3.2			

Assumption #1. PG&E explicitly accounted for transpressive internal deformation of the Irish Hills as Local Areal Source Zone earthquakes (§2.2.1). Removing assumption (1) has no hazard impact, because it was not used in the hazard modeling.

Assumption #2. PG&E assumed the dips of reverse faults to be from 35º to 80º, not any angle (§2.2.2). A modified assumption more in line with the main arguments of the Bird critique is listed as (2a) of Table 4.1: *Active reverse faults may dip more steeply than 45º.* Declaring this assumption to be false, as Dr. Bird has done, and thereby requiring reverse faults to dip less than 45º, as he has advocated, would likely have an impact on DCPP hazard by increasing the thrust-faulting component of the SSC. However, high-angle reverse faulting is mechanically feasible and commonly observed in transpressional inverted basins like those in the Los Osos domain (§3.2). Therefore, the modified assumption (2a) is true, not false.

Assumption #3. No earthquake geologist would disagree with Bird's statement that Assumption #3 is false; seismic hazard estimates depend heavily on understanding fault structures developed over many millions of years. PG&E conducted extensive investigations of geologic structures older than 0.33 Ma, and this evidence substantially informed the development of the SSC15 and SSC24 (§2.2.3). Dr. Bird's apparent purpose in attributing this assumption to PG&E is to validate his long-term slip-rate estimation by Method #2, which assumes that the Pliocene deformation that folded the Pismo Syncline continues at the same rate today.

Assumption #4. PG&E (2015, 2024) did not make the blanket assumption that GPS geodetic velocities are not useful for site-specific seismic hazard estimation. Instead, they employed the GPS data and models as validation checks, stating, "Whereas geodesy-based model slip rates are interpreted to be unreliable for use as direct inputs in the SSC model for DCPP, they are useful for comparison and to document whether there are large differences between results" (PG&E, 2024, p. 116). While the SRT agrees with Dr. Bird that the GPS data have been underutilized, the geodetic analysis of §3.4 shows that the existing GPS data place only weak constraints on the SWBZ slip rate, owing to the interference by interseismic deformations from other active faults.

- ➢ Finding 1: *The SRT analysis does not support the claim by Dr. Bird that removing the false assumptions in Table 4.1 would increase the seismic potency rate in the Irish Hills by a large factor.*

4.2. Bird's Estimates of Slip Rates

According to Dr. Bird (§2.5a), "Three independent analytic methods give values for the total slip-rate on all shallow-dipping thrust faults under the Irish Hills: 2.8 mm/yr, ~2.0 mm/yr, or 2.2 mm/yr." Table 4.2 compares these rates with the SRT estimates.

Method #1. Bird's first method for estimating slip-deficit rate is based on the Airy isostatic mechanism in which the compensation is purely local and the depth of compensation is at the Moho discontinuity. A more realistic model is regional compensation in which non-isostatic loads are supported by the flexural rigidity of the lithosphere (see §3.1). The flexural response of loads of small horizontal dimension, such as the Irish Hills, is better approximated by the Bouguer (thick plate) mechanism, rather than the Airy (thin plate) mechanism assumed by Dr. Bird. Adopting this mechanism drops his estimate of slip rate by a factor of six, from 2.8 mm/yr to 0.47 mm/yr. This mean rate is further reduced to 0.32 mm/yr if the average SWBZ dip of 38º is used. The SRT's best estimate of this slip rate is 0.29 ± 0.07 mm/yr, based on an uplift rate of 0.18 ± 0.03 mm/yr.

Method #2. Bird's second method for estimating slip-deficit rate is based on projection of the base of the Obispo formation from the south limb of the Pismo Syncline above the SWBZ and estimating 1.6 to 2.2 km fault throw relative to outcrops mapped on the seafloor. This yields a 0.76-1.04 mm/yr slip rate, averaged since 5 Ma, on a thrust fault with 25° dip. Dr. Bird asserts symmetry of the fault system to double this rate to 1.55-2.08 mm/yr. Dr. Bird's model does not account for normal-faulting offset of strata prior to fault inversion and folding, nor does his model provide a kinematic explanation for the observed folding. Using a kinematically constrained fault-related fold model (§3.3), we estimate fault slip from the observed length of the south limb of the Pismo Syncline and its truncation against the San Miguelito normal fault, which we hypothesize was inverted with reverse slip to produce the fold. This yields 1.8 ± 0.2 km of fault slip, to which we add 0.8 ± 0.1 km of slip restored from other uplift and shortening components, for a total of 2.6 ± 0.3 km of slip on a 40° dipping modeled fault. The faulting is modeled as asymmetric, consistent with the lack of evidence for a throughgoing reverse fault corresponding to the Los Osos trend. This model yields a thrust fault slip rate of 0.5 ± 0.1 mm/yr, averaged since 5.1 ± 0.4 Ma, which is a factor of three to four less than that proposed by Dr. Bird. The short-term estimate is marginally lower than the long-term rate, suggesting some slowing of the compressive deformation; however, the rates are not significantly different at the 95% confidence level.

Method #3. The third method is based on using a combination of modeling results from Shen & Bird (2022) and individually selected GPS station velocities to derive a thrusting slip rate of approximately 2.2 mm/yr. While the Shen and Bird (2022) methods could be applied to create a 3D kinematic model of the SSC fault system, their published results used the 2023 NSHM fault model and slip rates as input, which are significantly different from those of the SSC. Bird's shortening rate of 2 mm/yr across a 20- to 25-km Irish Hills baseline corresponds to a contractional strain rate of –100 to –80 nanostrain/yr. The uncertainties are large (~10 nanostrain/yr), but the four estimates derived from the profile analysis of the corrected Zeng GPS data are negative (contraction) and lie in the range of –19 to –42 nanostrain/yr (average = –27 nanostrain/yr) (Table 3.3). In comparison, the dilatational strain rates from the 2D strain rate inversions averaged over the same 1D baselines are also all negative (contractional) and have values from –26 to –34 nanostrain/yr (average = –30 nanostrain/yr). While we find some larger shortening rates normal to the SWBZ, we show that these can be explained by SAF-parallel shear. The consistency of the velocity-profile estimates with the strain-rate inversions suggests that the best estimates of contraction are in the SAF-normal direction and the dominant deformation in the SAF-parallel direction is simple plate-boundary shear. The GPS constraint on the rate of contraction across the Irish Hills is a factor of two to five times smaller than the Bird estimate. Translating this contraction rate directly into a slip rate requires the unjustified assumptions that all strain is elastic and released by slip on the SWBZ and that no other faults are involved in producing shortening. It thus provides only an upper bound on the slip rate (Table 4.2).

- ➢ <u>Finding 2</u>: *The SWBZ, including its possible reverse-faulting extensions along strike, is the most likely fault system for producing the largest reverse-slip earthquakes beneath the Irish Hills.*
- ➢ <u>Finding 3</u>: *The geological structure of the Irish Hills indicates a moderate (38º ± 3º) dip of the SWBZ, consistent with fault-outcrop observations and reactivation of steeply dipping normal faults in its hangingwall to fold the Pismo Syncline.*

➢ Finding 4: *The best estimate of the SWBZ slip rate during the last 124.0 ± 2.5 ka, inferred from the uplift rate of the MIS 5e marine terrace and the SWBZ dip, is 0.29 ± 0.07 mm/yr, which is about an order of magnitude smaller than the rates proposed by Dr. Bird.*

➢ Finding 5: *The long-term (5 Ma) slip rate of 0.50 ± 0.10 mm/yr inferred for the SWBZ from the kinematically constrained fault analysis is marginally higher than the short-term (120 ka) rate and significantly less than Bird's long-term rate of 2 mm/yr.*

➢ Finding 6: *The GPS results show right-lateral shear deformation across the greater Irish Hills region. The contractional component perpendicular to the SAF is about –20 to –40 nanostrain/yr, which is 2 to 5 times smaller than the strain rate of –80 to –100 nanostrain/yr estimated by Dr. Bird.*

Table 4.2. SWBZ Slip Rates

Method	Bird (mm/yr)	SRT (mm/yr)
1. Isostatic	2.8	0.29 ± 0.07
2. Thrust fault heave rate	~2	0.50 ± 0.10
3. GPS geodetic horizontal shortening rate	2.2*	0.95 ± 0.32*

Bird assumptions: dip: 25º; uplift rate: 0.2 mm/yr.
SRT assumptions: dip: 38º ± 3º; uplift rate: 0.18 ± 0.03 mm/yr.
*Upper bound assuming all strain is elastic and released by slip only on SWBZ.

4.3. Noto24 as an Analog Earthquake

Dr. Bird contends that Noto24 can be used as the characteristic event in a time-independent recurrence model of the DCPP hazards from thrust earthquakes beneath the Irish Hills. By combining the mean Noto24 slip, taken to be 2 m, with his estimates of thrust-fault slip rates (2.0-2.8 mm/yr), he obtains a recurrence interval of 715-1000 yr for **M**7.5 thrust earthquakes under the Irish Hills.

The SRT has reviewed the scientific literature on Noto24 and its tectonic environment, including responses to the Bird's characteristic earthquake hypothesis by Madugo & Kottke (2024), LCI (2024), and NRC (2025). From a comparison of Noto24 with plausible SWBZ ruptures (§3.5), the SRT draws three conclusions:

➢ Finding 7: *Based on the Noto Peninsula uplift data, the best estimate of the recurrence interval for a Noto24-type event on the Noto Peninsula fault system is 4000-5700 yr.*

➢ Finding 8: *Applying the same model to the Irish Hills yields a Noto24 recurrence interval of 22,000 ± 3,800 yr, about 20 times longer than Dr. Bird's estimates.*

➢ Finding 9: *Owing to tectonic differences, including the geometric incompatibility of Noto24-type rupture with the faults available in the SWBZ, the SRT concludes that Noto24 is an implausible analog for reverse faulting beneath the Irish Hills.*

4.4. Overall Assessment of the Bird Critique

The Bird critique comprises three main assertions:

(a) PG&E (2015, 2024) underestimated the hazard to DCPP from thrust faulting under the Irish Hills because it made four false assumptions (§2.2). Removing these assumptions increases the thrust-faulting potency rate by a large factor.

(b) Three independent analytic methods give values for the total slip rate on shallow dipping thrust faults under the Irish Hills in the range of 2.0-2.8 mm/yr (§2.3).

(c) The recurrence interval of Noto24-type earthquakes that involves Irish Hills thrust faulting is 715-1000 yr, which poses an unacceptable risk to DCPP (§2.4).

The SRT analysis discounts the plausibility of all three statements. The SRT concludes that removing the four false assumptions in the development of a revised SSC would have no impact on the hazard estimates (§4.1). The SRT estimates the slip rate on the SWBZ thrust faults under the Irish Hills to be 0.29 ± 0.07 mm/yr, which is an order of magnitude smaller than Bird's estimates (§4.2). The SRT agrees with Madugo & Kottke (2024), LCI (2024), and NRC (2025) that a Noto24-type earthquake is not suitable as a characteristic earthquake for thrust faulting beneath the Irish Hills (§4.3). The SRT notes that, if Noto24 were adopted as the characteristic event for the Irish Hills, the estimated recurrence interval would be ten to twenty times longer than Bird's estimates.

➢ Finding 10: *The best available science does not support the three main assertions of the Bird critique.*

4.5. Findings Regarding the SSC Model

The Bird critique raises many questions regarding the representation of reverse-faulting earthquakes by the SSC model, particularly the SLPB fault geometry models (FGMs) and the slip-rate allocations. The SRT has not formally assessed the current SSC model and has no mandate to do so. However, the SRT has reached findings regarding thrust faulting beneath the Irish Hills that may prove useful in future assessments of the SSC.

The fault system analysis of §3.3 finds that the SSC FGMs include fault-system representations sufficient to characterize the thrust-faulting hazard beneath the Irish Hills, although the range of possible fault dips within the SWBZ fault-set needs to be extended to include the lower values estimated by the SRT.

- ➢ Finding 11: *The existing SSC FGMs, with modifications to include a lower range of dip for the SWBZ, can adequately represent the hazard of thrust faulting beneath the Irish Hills.*

There is no apparent need to supplement the SWBZ fault set with an Inferred Coastline thrust fault, as advocated by Dr. Bird, because the hazard from that hypothetical fault can be adequately represented by the SWBZ sources of the PG&E SSC Southwest-Vergent model, provided that the dip range of the faulting is revised to shallower angles.

- ➢ Finding 12: *The fault system analysis of §3.3 favors the SW-Vergent FGM over the NE-Vergent and Outward-Vergent FGMs in representing what is known about the style of faulting in the SLPB system.*

In the NE-Vergent and Outward-Vergent FGMs, the Los Osos trend is modeled as a reverse fault with a high enough slip rate to qualify it as one of four Primary fault sources that make the largest contributions to the DCPP hazard (Figure 2.1).

- ➢ Finding 13: *Though the Los Osos trend displays evidence for neotectonic activity, this evidence does not require reverse slip on a Los Osos reverse fault.*

The fault system analysis of §3.3 interprets the Los Osos deformation to be related to a hingeline formed above a bend in the SWBZ, although we recognize that it could also result from a component strike-slip faulting. If subsidence of Morro Bay is a result of a dextral stepover, this could affect the pattern of marine-terrace uplift and change interpretation of the deeper geometry of the SWBZ.

- ➢ Finding 14. *The observed dip of SWBZ faulting ranges between 25° and 56° with a mean dip of 38° ± 3°, which is below the dip range allowed by the SW-Vergent FGM (45°-50°).*

The fault system analysis of §3.3 shows that a moderately dipping SWBZ, with slip branching into steeply dipping, reactivated normal faults in its hangingwall, is consistent with fault outcrop exposures, folding of the Pismo syncline and the pattern of uplift evident from Q2 marine terrace elevations. Folding of the Q2 terrace at the Los Osos hingeline indicates that fault dip may flatten to the north within the seismogenic zone. A more gentle 25° dipping fault solution is deemed implausible, because the fault surface would intersect the Obispo formation and well control in the down-dip direction.

- ➢ Finding 15: *The SRT's preferred rate estimate for the SWBZ (0.29 ± 0.07 mm/yr) is marginally higher than the estimate from the SW-Vergent FGM (0.17 ± 0.05 mm/yr) partially because the assumed fault dip is lower (38° ± 3°).*

4.6. Recommendations for Future Work

The SRT makes several recommendations for future research that could further elucidate and quantify the seismic hazards associated with reverse faulting beneath the Irish Hills.

4.6.1. Fault System Modeling

The 2014 geological and geophysical studies (PG&E, 2014a,b,c) included a geometric model of faulting of the Irish Hills, but the model does not correctly reproduce the kinematics of the observed folding since 5 Ma (§2.2.3c and §3.3). Fault-bend fold theory provides a framework to refine existing source model geometries and reveal possible sources outside of the inventory considered by the PG&E SSC. For example, we find that the dip of the south limb of the Pismo Syncline and the field observations of fault dips within the SBFZ support a moderately dipping (~40°) thrust faulting solution, which is below the range presently modeled in the SW-Vergent FGM (45º-75º).

- ❖ Recommendation 1: *The SRT recommends the development of a set of kinematically constrained structural models for reverse faults underlying the Irish Hills that can explain the folding observed since 5 Ma*.

The long-term 0.5 ± 0.1 mm/yr rate of SWBZ slip since 5.1 ± 0.04 Ma is somewhat higher than the 0.29 ± 0.07 mm/yr rate inferred from marine-terrace uplift since 124.0 ± 2.5 ka, which may be interpreted as slowing of the thrusting rate. Another possible explanation is that the reference frame for these measurements differs, because the latter is referenced to sea level, while the former is referenced to the SWBZ footwall. The rate of SWBZ footwall subsidence, relative to sea-level, would add to the uplift rate inferred from marine-terrace elevations in its hangingwall.

- ❖ Recommendation 2: *The SRT recommends dating of low-stand abrasion platforms offshore, south of the Irish Hills, to further constrain the rate of footwall subsidence and its contribution to the SWBZ slip rate.*

Recently presented IRSL dating of the Cayucos marine terrace (Rivera et al., 2025) calls into question the accepted MIS 5 age assignment here (Hanson et al., 1992). The SRT finds these new IRSL dates to be less reliable than high-precision U-series age dating from solitary corals. Should the IRSL dating prove correct, however, this would require reassessment of the critical Q2 marine terrace age from the Irish Hills.

- ❖ Recommendation 3: *The SRT recommends monitoring of IRSL-dating efforts and reassessment, if necessary, of the MIS 5 age assignments for the Q1 and Q2 terraces surrounding the Irish Hills.*

In our fault-system analysis (§3.3) the position and change in marine-terrace uplift rate across the Los Osos trend constrains the geometry of the SWBZ at depth. The pattern of marine terrace uplift could also be independently affected by strike-slip faulting in the vicinity of Morro Bay, which would change the SWBZ interpretation and lend support to the Outward-Vergent model within the SSC logic tree.

- ❖ Recommendation 4: *The SRT recommends further investigation of potential strike-slip faulting along the Los Osos trend and its impacts on the pattern of marine-terrace uplift.*

4.6.2. Geodetic Modeling

GPS data provide integral constraints on the surface deformation rates that are independent of geological rates and can thus be useful in validating fault system deformation models. The SRT geodetic analysis has explored several dimensions of the problem, including the use of elastic dislocation models to remove the deformation due to well-constrained, high-slip faults (in this case the San Andreas and Hosgi) and inversion methods for deriving strain-rate maps from limited collections of uncertain GPS velocity vectors (§3.4).

- ❖ Recommendation 5: *PG&E should follow up the SRT's preliminary work with a more complete study of the available GPS data*.

The corrections for SAF loading are substantial. After correction, the profiles show SAF-normal contraction at a rate of –20 to –40 nanostrain/yr, two to four times smaller than Bird's estimate of –80 to –100 nanostrain/yr. We also observe a strong SAF-parallel shear that is due, at least in part, to active strike-slip faults outside the Los Osos domain, such as the Rinconada and East/West Huasna faults. Assessing the deformation caused by the SLPB fault system using GPS data will require refined regional fault models with better constraints on the slip rates of the Rinconada, Huasna, and other strike-slip faults.

- ❖ Recommendation 6: *The fault slip models that underlie the DCPP SSC should be developed into kinematic and mechanical models that can predict the interseismic deformation and can thus be directly tested against the GPS data.*

A primary objective of this testing should be to determine if the entire suite of SSC fault slip rates produce deformation that is within the uncertainties of the geodetic data. A secondary objective is to quantify the SSC representation of "transpression":

- ❖ Recommendation 7: *PG&E should compute the relative contributions of strike-slip and reverse faulting to the regional deformation predicted by the SSC24 slip models and compare the values with the geodetic constraints*.

PG&E (2015) assumed that earthquakes in the Local Areal Source Zone of the SSC are 70% strike-slip and 30% reverse-slip, but, to our knowledge, the net strain partitioning of complete SSC models into strike-slip and reverse-slip components has not been closely examined.

Better geodetic modeling of the Los Osos domain will require better data on the interfering external signals. Data gaps include the poorly known slip rates of other major strike-slip faults that lie between the SAF and the Los Osos domain.

- ❖ <u>Recommendation 8:</u> *Geologic slip-rate information should be acquired from the Rinconada and Huasna faults to permit better modeling of the shear component evident in the GPS data.*

In the long term, PG&E should consider implementing the NSHM methodology of Field et al. (2023), which uses a suite of deformation models (possibly including NeoKinema), driven by the same inputs, to test the slip rate and fault geometry inputs to the hazard models. Because modeling uncertainties are poorly understood, multiple models based on different assumptions are essential for cross-validation and uncertainty estimation.

4.6.3. SSC Modeling

The SRT is not aware of any plans to revise the DCPP SSC and understands that doing so would be major undertaking. The SSC is an extremely complex model with hundreds of co-varying parameters, and the epistemic uncertainty of the model is represented by an intricate set of logic trees in which the alternative models are weighted by expert judgment. Investigating the hazard implications of the new information provided by the SRT study therefore requires full-model sensitivity experiments to assess the hazard impact of imposing the new constraints (Field et al., 2023).

- ❖ <u>Recommendation 9</u>: *PG&E should conduct modeling experiments to ascertain the sensitivity of DCPP hazard to the SSC modifications recommended by the SRT.*

PG&E should specifically reexamine the weighting of alternative FGMs, and it should assess the impact of placing significantly more weight on and lowering the dip range of the SW-Vergent model, which better represents the likely reverse-fault hazard.

5. References

Allmendinger, R. W., J. P. Loveless, M. E. Pritchard & B. J. Meade (2009). From decades to epochs: Spanning the gap between geodesy and structural geology of active mountain belts, *J. Struct. Geol.*, **31** 1409-1422. doi: 10.1016/j.jsg.2009.08.008.

Allmendinger, R. W., R. Reilinger & J. P. Loveless (2007). Strain and rotation rate from GPS in Tibet, Anatolia, and the Altiplano, *Tectonics*, **26**. https://doi.org/10.1144/transed.8.3.387.

Anderson, E.M. (1905). The dynamics of faulting, *Transactions of the Edinburgh Geological Society*, **8**, 387–402. https://doi.org/10.1144/transed.8.3.387.

Angelier, J. (1979). Determination of the mean principal directions of stresses for a given fault population, *Tectonophysics*, **56**, 17–26, https://doi.org/10.1016/0040-1951(79)90081-7.

Argus, D. F., M. B. Heflin, G. Peltzer, F. Crampé & F. H. Webb (2005). Interseismic strain accumulation and anthropogenic motion in metropolitan Los Angeles, *J. Geophys. Res.*, **110**, doi:10.1029/2003JB002934.

Baker, J., B. Bradley & P. Stafford (2021). *Seismic Hazard and Risk Analysis*, 1st ed., Cambridge University Press. doi:10.1017/9781108425056.

Bawden, G. W., W. Thatcher, R. S. Stein, K. W. Hudnut, and G. Peltzer (2001). Tectonic contraction across Los Angeles after removal of groundwater pumping effects, *Nature*, **412**, 812-815.

Bird, P. (2009). Long-term fault slip rates, distributed deformation rates, and forecast of seismicity in the western United States from fitting of community geologic, geodetic, and stress direction datasets, *J. Geophys. Res.*, **114**, B11403, doi:10.1029/2009JB006317.

Bird, P., & Y. Y. Kagan (2004). Plate-tectonic analysis of shallow seismicity: Apparent boundary width, beta, corner magnitude, coupled lithosphere thickness, and coupling in seven tectonic settings, *Bull. Seismol. Soc. Am.*, **94**, 2380-2399, https://doi.org/10.1785/0120030107.

Bird, P., Y. Y. Kagan, D. D. Jackson, F. P. Schoenberg & M. J. Werner (2009). Linear and nonlinear relations between relative plate velocity and seismicity, *Bull. Seismol. Soc. Am.*, **99**, 3097-3113, doi:10.1785/0120090082.

Bird, P., & C. Kreemer (2015). Revised tectonic forecast of global shallow seismicity based on version 2.1 of the Global Strain Rate Map, *Bull. Seismol. Soc. Am.*, **105**, 152-166, doi:10.1785/0120140129.

Bird, P., C. Kreemer & W. E. Holt (2010). A long-term forecast of shallow seismicity based on the Global Strain Rate Map, *Seismol. Res. Lett.*, **81**, 184-194, plus electronic appendices, https://doi.org/10.1785/gssrl.81.2.184.

Bird, P., & Z. Liu (2007). Seismic hazard inferred from tectonics: California, in: S. E. Hough & K. B. Olsen (ed.), Special Issue on: Regional Earthquake Likelihood Models, *Seismol. Res. Lett.*, **78**, 37-48.

Budnitz, R. J., G. Apostolakis, D.M. Boore, L.S. Cluff, K.J. Coppersmith, C.A. Cornell & P.A. Morris, the Senior Seismic Hazard Analysis Committee (SSHAC) (1997). *Recommendations for Probabilistic Seismic Hazard Analysis: Guidance on Uncertainty and Use of Experts* (NUREG/CR-6372, UCRL-ID-122160), Vols. 1/2, U.S. Nuclear Regulatory Commission, U.S. Department of Energy, Electric Power Research Institute.

Chen, G., Y. Wu, M. Xia & Z. Li (2024). Focal mechanics and disaster characteristics of the 2024 M 7.6 Noto Peninsula Earthquake, Japan, *Frontiers of Structural and Civil Engineering,* **18**, 1378-1387, https://doi.org/10.1007/s11709-024-1111-1.

DeMets, C., B. Márquez-Azúa & E. Cabral-Cano (2014). A new GPS velocity field for the Pacific Plate – Part 2: implications for fault slip rates in western California, *Geophys. J. Int.*, **199**, 1900-1909. doi: 10.1093/gji/ggu347.

Eymold, W. K., & T. H. Jordan (2019), Tectonic regionalization of the Southern California crust from tomographic cluster analysis, *J. Geophys. Res.*, **124**, 11,840-11,865, doi:10.1029/ 2019JB018423.

Field, E. H., K. R. Milner, A. E. Hatem, P. M. Powers, F. F. Pollitz, A. L. Llenos, Y. Zeng, K.M. Johnson, B. E. Shaw, D. McPhillips, J. Thompson Jobe, A. M. Shumway, A. J. Michael, Z.-K. Shen, E. L. Evans, E. H. Hearn, C. S. Mueller, A. D. Frankel, M. D. Petersen, C. DuRoss, R. W. Briggs, M. T. Page, J. L. Rubinstein and J. A. Herrick (2023). (2023). The USGS 2023 Conterminous U.S. Time-Independent Earthquake Rupture Forecast, *Bull. Seismol. Soc. Am.*, **114**, 523-571.

Fukushima, Y., D. Ishimura, N. Takahashi, Y. Iwasa, L. C. Malatesta, T. Takahashi, C. H. Tang, K. Yoshida & S. Toda, S. (2024). Landscape changes caused by the 2024 Noto Peninsula earthquake in Japan. *Science advances*, **10**, p.eadp9193, doi:10.1126/sciadv.adp9193.

Gephart, J.W. (1990). Stress and the direction of slip on fault planes, *Tectonics*, **9**, 845–858. doi:TC009i004p00845.

Gerstenberger, M. C., S. Bora, B. A. Bradley, C. DiCaprio, A. Kaiser, E. F. Manea, A. Nicol, C. Rollins, M.W. Stirling, K. K. S. Thingbaijam, R. J. Van Dissen, E. R. Abbott, G. M. Atkinson, C. Chamberlain, A. Christophersen, K. Clark, G. L. Coffey, C. A. de la Torre, S. M. Ellis, J. Fraser, K. Graham, J. Griffin, I. J. Hamling,M. P. Hill, A. Howell, A. Hulsey, J. Hutchinson, P. Iturrieta, K.M. Johnson, V. O. Jurgens, R. Kirkman, R. M. Langridge, R. L. Lee, N. J. Litchfield, J. Maurer, 654 K. R. Milner, S. Rastin, M. S. Rattenbury, D. A. Rhoades, J. Ristau, D. Schorlemmer, H. Seebeck, B. E. Shaw, P. J. Stafford, A. C. Stolte, J. Townend, P. Villamor, L.M.Wallace, G.Weatherill, C. A.Williams, and L. M. Wotherspoon (2023, 12). The 2022 Aotearoa New Zealand National Seismic Hazard Model: Process, Overview, and Results. *Bulletin of the Seismological Society of America* **114**(1), 7–36.

Hanson, K., W. Lettis, J. Wesling, K. Kelson & L. Mezger (1992). Quaternary marine terraces, south-central coastal California: Implications for crustal deformation and coastal evolution, in: Fletcher, C.H., Wehmiller, J.F. (Eds.), *Quaternary Coasts of the United States*, Society for Sedimentary Geology, https://doi.org/10.2110/pec.92.48.

Hanson, K.L., Wesling, J.R., Lettis, W.R., Kelson, K.I., Mezger, L. (1994). Correlation, ages, and uplift rates of Quaternary marine terraces: South-central coastal California, in: Alterman, I., McMullen, R., Cluff, L., and Slemmons, B., Seismotectonics of the Central California Coast Ranges, *Geological Society of America Special Paper 292*, Geological Society of America, pp. 45–72, https://doi.org/10.1130/SPE292-p45.

Hyndman, R. D., C. A. Currie, S. Mazzotti & A. Frederiksen (2009). Temperature control of continental lithosphere elastic thickness, Te vs Vs, *Earth Planet. Sci. Lett.*, **277**, 539-548, https://doi.org/10.1016/j.epsl.2008.11.023.

IPRP (2024). Initial Review of the PG&E "Updated Seismic Assessment, February 2024", *IPRP Report No. 16*, Aug 26, 2024, 44 pp.

Jiang, J., & R. B. Lohman (2021). Coherence-guided InSAR deformation analysis in the presence of ongoing land surface changes in the Imperial Valley, California, *Remote Sensing of Environment*, **253** 112160: https://doi.org/10.1016/j.rse.2020.112160.

Johnson, K. M., W. C. Hammond & R. J. Weldon, II (2024). Review of geodetic and geologic deformation models for 2023 U.S. National Seismic Hazard Model, *Bull. Seismol. Soc. Am.*, **114**, 1407-1436, doi:10.1785/0120230137.

Jordan, T. H., N. Abrahamson, J. G. Anderson, G. Biasi, K. Campbell, T. Dawson, H. DeShon, M. Gerstenberger, N. Gregor, K. Kelson, Y. Lee, N. Luco, W. Marzocchi, B. Rowshandel, D. Schwartz, N. Shome, G. Toro, R. Weldon, and I. Wong (2023). Panel review of the USGS 2023 Conterminous U.S. Time-Independent Earthquake Rupture Forecast, *Bull. Seismol. Soc. Am.*, **114**, 572–607, https://doi.org/10.1785/0120230140.

Keller, M. A., & J. A. Barron (1993). Re-evaluation of the Miguelito Member of the Pismo Formation of Montana de Oro State Park, California, *American Association of Petroleum Geologists Bulletin*, **77**, 703-704.

Koike, K., & H. Machida (2001). *Atlas of Quaternary Marine Terraces in the Japanese Islands*, University of Tokyo Press, Tokyo, Japan (in Japanese).

Langenheim, V. E., R. C. Jachens, R. W. Graymer, J. P. Colgan, C. M. Wentworth, and R. G. Stanley (2012). Fault geometry and cumulative offsets in the central Coast Ranges, California: Evidence for northward increasing slip along the San Gregorio–San Simeon–Hosgri fault, *Lithosphere*, **5**, 9-48, https://doi.org/10.1130/L233.1.

LCI (2024). Phase 1 Review of the Tectonic and Geomorphic Setting of the January 1, 2024, M7.5 Noto Earthquake, Noto Peninsula, Japan, Lettis Consultants International Project No. 1005.125, 54 pp.

Leonard, M. (2010). Earthquake fault scaling: self-consistent relating of rupture length, width, average displacement, and moment release. *Bull. Seismol. Soc. Am.*, **100**, 1971–1988, https://doi.org/10.1785/0120090189.

Lettis, W.R., & N. T. Hall (1994). Los Osos fault zone, San Luis Obispo County, California, in: Alterman, I., McMullen, R., Cluff, L., and Slemmons, B., *Seismotectonics of the Central California Coast Ranges,* Geological Society of America Special Paper 292, pp. 73–102, https://doi.org/10.1130/SPE292-p73.

Lettis, W.R., Kelson, K.I., Wesling, J.R., Angell, M., Hanson, K.L., & Hall, N.T. (1994). Quaternary deformation of the San Luis Range, San Luis Obispo County, California, in: Alterman, I., McMullen, R., Cluff, L., and Slemmons, B., *Seismotectonics of the Central California Coast Ranges*, Geological Society of America Special Paper 292, pp. 111–132, https://doi.org/10.1130/SPE292-p111.

Liu, C., Bai, Y., Lay, T., He, P., Wen, Y., Wei, X., Xiong, N. and Xiong, X. (2024). Shallow crustal rupture in a major M_W 7.5 earthquake above a deep crustal seismic swarm along the Noto Peninsula in western Japan, *Earth Planet. Sci. Lett.*, **648**, p.119107, https://doi.org/10.1016/j.epsl.2024.119107.

Loveless, J. P., & B. J. Meade (2011). Stress modulation on the San Andreas fault by interseismic fault system interactions, *Geology*, **39**, 1035-1038, doi: 10.1130/g32215.1.

Ma, Z., Zeng, H., Luo, H., Liu, Z., Jiang, Y., Aoki, Y., Wang, W., Itoh, Y., Lyu, M., Cui, Y. and Yun, S.H. (2024). Slow rupture in a fluid-rich fault zone initiated the 2024 Mw 7.5 Noto earthquake, *Science* [online], https://doi.org:10.1126/science.ado5143.

Madugo, C., & A. Kottke (2024). Presentation to the DCISC at the public meeting of October 9, 2024.

Maggi, A., J. A. Jackson, D. Mckenzie & K. Priestley (2000). Earthquake focal depths, effective elastic thickness, and the strength of the continental lithosphere, *Geology*, 28, 495-498.

Marshall, S. T., G. J. Funning & S. E. Owen (2013). Fault slip rates and interseismic deformation in the western Transverse Ranges, CA, *J. Geophys. Res.*, **118**, 4511-4534. doi:10.1002/jgrb.50312.

Masuda, H., Sugawara, D., Cheng, A.C., Suppasri, A., Shigihara, Y., Kure, S. and Imamura, F. (2024). Modeling the 2024 Noto Peninsula earthquake tsunami: implications for tsunami sources in the eastern margin of the Japan Sea, *Geoscience Lett.*, **11**, 1-12, https://doi.org/10.1186/s40562-024-00344-8.

Maurer, J., & K. Materna (2023). Quantification of geodetic strain rate uncertainties and implications for seismic hazard estimates, *Geophs. J. Int.*, **234**, 2128-2142. doi:10.1093/gji/ggad191.

Menke, W. (1989). *Geophysical Data Analysis: Discrete Inverse Theory*, Academic Press, San Diego, CA.

McGregor, I.S., Onderdonk, N.W. (2021). Late Pleistocene rates of rock uplift and faulting at the boundary between the southern Coast Ranges and the western Transverse Ranges in California from reconstruction and luminescence dating of the Orcutt Formation, *Geosphere,* **17**, 932–956, https://doi.org/10.1130/GES02274.1.

Medwedeff, D. (1992). Geometry and kinematics of an active, laterally-propagating wedge-thrust, Wheeler Ridge, California, in: Mitra, S., Fischer, G. (Eds.), *Structural Geology of Fold and Thrust Belts*. Johns Hopkins University Press, pp. 3–28.

Medwedeff, D. (1989). Growth fault-bend folding at Southeast Lost Hills, San Joaquin Valley, California1, *AAPG Bulletin*, **73**, 54–67, https://doi.org/10.1306/703C9AE6-1707-11D7-8645000102C1865D.

Michael, A. J. (1990). Energy constraints on kinematic models of oblique faulting: Loma Prieta versus Parkfield-Coalinga. Geophysical Research Letters, **17**, 1453–1456, https://doi.org/10.1029/GL017i009p01453.

Minster, J.B. & T. H. Jordan (1987). Vector constraints on western U.S. deformation from space geodesy, neotectonics, and plate motions, *J. Geophys. Res.*, **92**, 4798–4804, https://doi.org/10.1029/JB092iB06p04798.

Morris, A., Ferrill, D.A., Brent Henderson, D.B. (1996). Slip-tendency analysis and fault reactivation, *Geology*, **24**, https://doi.org/10.1130/0091-7613(1996)024<0275:STAAFR>2.3.CO;2.

Muhs, D. R., Kennedy, G. L., Rockwell, T. K. (1994). Uranium-series ages of marine terrace corals from the Pacific Coast of North America and implications for last-interglacial sea level history. *Quaternary Research*, **42**, 72–87. https://doi.org/10.1006/qres.1994.1055

Namson, J., & Davis, T. (1990). Late Cenozoic Fold and Thrust Belt of the Southern Coast Ranges and Santa Maria Basin, California, *AAPG Bulletin*, **74**, https://doi.org/10.1306/0C9B2335-1710-11D7-8645000102C1865D.

Murray-Moraleda, J. R., J. L. Svarc, T. Onishi, and W. Thatcher (2011). An interseismic velocity field for the central California coast region derived from Global Positioning System measurements, Unpublished technical report, submitted to PG&E.

Narr, W., & J. Suppe (1994). Kinematics of basement-involved compressive structures. *American Journal of Science*, **294**, 802–860.

Nitchman, S.P., & Slemmons, D.B., 1994. The Wilmar Avenue fault: A late Quaternary reverse fault near Pismo Beach, California, in: Alterman, I., McMullen, R., Cluff, L., and Slemmons, B., *Seismotectonics of the Central California Coast Ranges*, Geological Society of America Special Paper 292, 103–110, https://doi.org/10.1130/SPE292-p103.

NRC (2025). *Proposed Director's Decision Under 10 CFR 2.206*, Adams Accession No. ML24302A148.

O'Connell, D. R. H. & J. Turner (2023). Hosgri Fault transpressional slip rates reproduce observed central California coast uplift rates, *The Seismic Record*, **3**, 182-193, doi: 10.1785/0320220047.

Petersen, M. D., A. M. Shumway, P. M. Powers, E. H. Field, M. P. Moschetti, K. S. Jaiswal, K. R. Milner, S. Rezaeian, A. D. Frankel, A. L. Llenos, et al. (2023). The 2023 U.S. 50-State National Seismic Hazard Model: Overview and implications, *Earthquake Spectra* **40**, https://doi.org/10.1177/87552930231215428.

PG&E (2011). Report on the analysis of the Shoreline fault zone, Central Coastal California, 192 p., 12 appendices.

PG&E (2014a). Geologic Mapping and Data Compilation for the Interpretation Onshore Seismic Reflection Data, 80 pp.

PG&E (2014b). Offshore Low-Energy Seismic-Reflection Studies in Estero Bay, San Luis Obispo Bay, and Point Sal Areas, 307 pp.

PG&E (2014c). ONSIP 2011 Data Report, 134 pp.

PG&E (2014d). Response to Administrative Law Judge's Decision Number 12-09·008 Regarding Dr. Douglas Hamilton's Concerns, 84 pp.

PG&E (2015). Seismic Source Characterization for the Diablo Canyon Power Plant, San Luis Obispo County, California, 652 pp.

PG&E (2024). Diablo Canyon Updated Seismic Assessment, 394 pp.

Powers, P. M., Altekruse, J. M., Llenos, A. L., Michael, A. J., Haynie, K. L., Haeussler, P. J., Bender, A. M., Rezaeian, S., Moschetti, M. P., Smith, J. A., Briggs, R. W., Witter, R. C., Mueller, C. S., Zeng, Y., Girot, D. L., Herrick, J. A., Shumway, A. M., & Petersen, M. D. (2024). The 2023 Alaska National Seismic Hazard Model. *Earthquake Spectra*, **40**, 2545–2597, https://doi.org/10.1177/87552930241266741.

Reilly, C. A. Nicol & J. Walsh (2017). Importance of pre-existing fault size for the evolution of an inverted fault system, in *The Geometry and Growth of Normal Faults*, eds. C. Childs, R. E. Holdsworth, C. A.-L. Jackson, T. Manzocchi, J. J. Walsh & G. Yielding. Geological Society of London Special Publication 439, https://doi.org/10.1144/SP439.2.

Rivera, S., Esparza, L.-E., Onderdonk, N.W., Garcia, A. & (2025). Using infrared stimulated luminescence to better constrain terrace ages along the California coast, in: Geological Society of America Abstracts with Programs. Presented at the 2025 Cordilleran Section Meeting, Geological Society of America, Sacramento, CA.

Sandwell, D. T., and P. Wessel (2016). Interpolation of 2-D vector data using constraints from elasticity, *Geophys. Res. Lett.*, **43**, 10,703-10,709, doi: https://doi.org/10.1002/2016GL070340.

Savage, J. C., & R. O. Burford (1970). Accumulation of tectonic strain in California, *Bull. Seismol. Soc. Am.,* **60**, 1877-1896.

Savage, J. C., & R. O. Burford (1973). Geodetic determination of relative plate motion in central California, *J. Geophys. Res*., **78**, 832-845.

Savage, J. C. (1983). A dislocation model of strain accumulation and release at a subduction zone, *J. Geophys. Res*., 88, 4984-4996.

Scholz, C.H. (2019). *The Mechanics of Earthquakes and Faulting*, 2^{nd} ed., Cambridge University Press, Cambridge, 471 pp., ISBN 0521655404.

Shen, Z.-K., & P. Bird (2022). Neokinema deformation model for the 2023 update to the US National Seismic Hazard model, *Seismol. Res. Lett.*, **93**, 3037–3052, doi:10.1785/0220220179.

Shen, Z. K., M. Wang, Y. Zeng & F. Wang (2015). Optimal Interpolation of Spatially Discretized Geodetic Data, *Bull. Seismol. Soc. Am.*, **105**, 2117-2127, doi:10.1785/0120140247.

Shishikura, M., T. Echigo & Y. Namegaya (2009). Evidence for coseismic and aseismic uplift in the last 1000 years in the focal area of a shallow thrust earthquake on the Noto Peninsula, west-central Japan. *Geophys. Res. Lett*, **36**, L02307, https://doi.org/10.1029/2008GL036252.

Shishikura, M., T. Echigo & Y. Namegaya (2020). Activity of the off-shore active faults along the northern coast of the Noto Peninsula deduced from the height of the lower marine terrace and emerged sessile assemblage, *活断層研究*, **53**, 33-49.

Sibson, R.H. (1989). High-angle reverse faulting in northern New Brunswick, Canada, and its implications for fluid pressure levels, *J. Struct. Geol.*, **11**, 873-877, https://doi.org/10.1016/0191-8141(89)90104-1.

Sibson, R.H. (2020). Preparation zones for large crustal earthquakes consequent on fault-valve action, *Earth, Planets and Space*, ***72***, 1-20, https://doi.org/10.1186/s40623-020-01153-x.

Sibson, R. H., F. Roberts & K. H. Poulsen (1988). High-angle reverse faults, fluid pressure cycling, and mesothermal gold-quartz deposits, *Geology*, **16**, 551–555.

Simms, A.R., H. Rouby & K. Lambeck (2016). Marine terraces and rates of vertical tectonic motion: The importance of glacio-isostatic adjustment along the Pacific coast of central North America, *GSA Bulletin*, **128**, 81–93, https://doi.org/10.1130/B31299.1.

Smith, S. A. F., T. Tesei, J. M. Scott & C. Collettini (2017). Reactivation of normal faults as high-angle reverse faults due to low frictional strength: Experimental data from the Moonlight Fault Zone, New Zealand, *J. Struct. Geol.*, **105**, 34-43, https://doi.org/10.1016/j.jsg.2017.10.009.

Stein, M., G. J. Wasserburg, K. R.Lajoie & J. H. Chen (1991). U-series ages of solitary corals from the California coast by mass spectrometry. *Geochimica et Cosmochimica Acta*, **55**, 3709–3722, https://doi.org/10.1016/0016-7037(91)90069-H.

Suppe, J. (1983). Geometry and kinematics of fault-bend folding. *Am. J. Sci.*, **283**, 684–721, https://doi.org/10.2475/ajs.283.7.684.

Suppe, J., Medwedeff, D., 1990. Geometry and kinematics of fault-propagation folding, *Eclogae Geologicae Helvetiae,* **83**, 409–454.

Thomas, A. L. (1993). POLY3D: A three-dimensional, polygonal element, displacement discontinuity boundary element computer program with applications to fractures, faults, and cavities in the Earth's crust, Stanford University, 52 pp.

Titus, S. J., M. Dyson, C. DeMets, B. Tikoff, F. Rolandone, and R. Bürgmann (2011). Geologic versus geodetic deformation adjacent to the San Andreas fault, central California, *GSA Bulletin*, **123**, 794-820, doi: 10.1130/b30150.1.

Turner, J. P., & G. A. Williams (2004). Sedimentary basin inversion and intra-plate shortening, *Earth Sci. Rev.*, **65**, 277-304, https://doi.org/10.1016/j.earscirev.2003.10.002.

Watts, A. B. (2023). *Isostasy and Flexure of the Lithosphere*, 2nd ed., Cambridge University Press, Cambridge, United Kingdom, https://doi.org/10.1017/9781139027748.

Weigers, M., 2021. Preliminary Geologic Map of the West Half of the San Luis Obispo 30' x 60' Quadrangle, California.

Weigers, M., 2011. Preliminary Geologic Map of the Pismo Beach 7.5' Quadrangle San Luis Obispo County, California.

Wessel, P., Luis, J. F., Uieda, L., Scharroo, R., Wobbe, F., Smith, W. H. F., & Tian, D. (2019). The Generic Mapping Tools Version 6, *Geochemistry, Geophysics, Geosystems*, **20**, 5556–5564, https://doi.org/10.1029/2019GC008515

Xu, L., Ji, C., Meng, L., Ampuero, J.P., Yunjun, Z., Mohanna, S. and Aoki, Y. (2024). Dual-initiation ruptures in the 2024 Noto earthquake encircling a fault asperity at a swarm edge, *Science*, **385**, 871-876, doi:10.1126/science.adp0493.

Yeats, R., Huftile, G., Grigsby, F., 1988. Oak Ridge fault, Ventura fold belt, and the Sisar decollement, Ventura basin, California, *Geology*, **16**, 1112–1116.

Youngs, R. R., & K. J. Coppersmith (1985). Implications of fault slip rates and earthquake recurrence models to probabilistic seismic hazard estimates, *Bull. Seismol. Soc. Am.,* **75,** 939-964.

Zeng, Y. (2022). GPS velocity field of the western United States for the 2023 National Seismic Hazard Model update, *Seismol. Res. Lett.*, **93**, 3121–3134, doi: 10.1785/0220220180.

Appendix A: Biographical Sketches of SRT members

Thomas H. Jordan

Tom Jordan, the SRT chair, is a University Professor and the W. M. Keck Foundation Professor of Earth Sciences at the University of Southern California. His current research is focused on system-level models of earthquake processes, earthquake forecasting, continental structure and dynamics, and seismic tomography. He is an author of approximately 270 scientific publications, including two popular textbooks (with J. Grotzinger) *Understanding Earth, 8th ed.* and *The Essential Earth, 2nd ed*.

As the director of the Southern California Earthquake Center 2002-2017, he coordinated an international research program in earthquake system science that involved over 1000 scientists at more than 70 universities and research organizations. He established the international Collaboratory for the Study of Earthquake Predictability (CSEP) in 2006, and he was the lead SCEC investigator on projects to create and improve the time-dependent Uniform California Earthquake Rupture Forecast (UCERF). Following the 2009 L'Aquila earthquake, he was appointed by the Italian government to chair the International Commission on Earthquake Forecasting for Civil Protection, which developed the concept of operational earthquake forecasting. He has been a member of the Council of the National Academy of Sciences (2006-2009) and the Governing Board of the National Research Council (2008-2011). He chaired the NRC panels that produced two decadal reports, *Basic Research Opportunities in Earth Sciences* (2002) and *Living on an Active Earth: Perspectives on Earthquake Science* (2003). He currently serves on the Steering Committee of the National Seismic Hazard Mapping Project and chairs its Earthquake Rupture Forecast Review Panel.

Jordan received his Ph.D. from the California Institute of Technology in 1972. He was head of MIT's Department of Earth, Atmospheric and Planetary Sciences from 1988 to 1998. In 2000, he moved from MIT to USC and was appointed USC University Professor in 2004. He has been awarded the Macelwane and Lehmann Medals of the American Geophysical Union, the President's Medal and Woollard Award of the Geological Society of America, and the 2012 Award for Outstanding Contribution to Public Understanding of the Geosciences by the American Geosciences Institute. He is a fellow of the American Association for the Advancement of Science and the American Geophysical Union and an elected member of the National Academy of Sciences, the American Academy of Arts and Sciences, and the American Philosophical Society.

Michael E. Oskin

Mike Oskin is a Professor at the University of California, Davis. His research focuses on the geological record of earthquakes, with foundations in structural geology, tectonics, process geomorphology, and Quaternary geochronology. Much of his work involves the characterization of earthquake rupture history and rates of fault slip using high-resolution topography, surficial geologic information, and a variety of age-dating techniques. He has conducted active-fault research in California, Mexico, and China, and is the author of approximately 90 scientific publications.

Oskin received his Ph.D. from the California Institute of Technology in 2002. He joined the Geological Sciences Department at the University of North Carolina - Chapel Hill in 2004, moved to the University of California, Davis in 2008, and chaired the UC Davis Department of Earth and Planetary Sciences from 2017 to 2021. Oskin is a Fellow of the Geological Society of America. He served on the Science Planning Committee of the Southern California Earthquake Center from 2005 to 2023 as one of the leaders for the earthquake geology group. He also served on the project review committee for the 2024 update to the earthquake response plan for the National Earthquake Hazard Reduction Program, and currently serves on the Scientific Earthquake Studies Advisory Committee to the U.S. Geological Survey.

Scott T. Marshall

Scott Marshall is a Professor at Appalachian State University. His research focuses on geophysics where he integrates computational modeling of geometrically complex faults with space geodetic estimates of deformation to better understand how the Earth deforms in response to tectonic stresses. He is currently a developer of the SCEC Community Fault Model, the co-creator and developer of the SCEC Geologic Slip Rate slip rate database, and has recently co-developed the web-based visualization tool for SCEC Community Velocity Models. He is the author of 22 peer-reviewed publications and has authored more than 30 externally funded proposals.

Marshall received his Ph.D. from the University of Massachusetts in 2008. He joined the faculty in the Department of Geology (now Department of Geological and Environmental Sciences) at Appalachian State University in 2008 where he is currently the Program Director for the Environmental Science program and is the co-director for the College of Arts and Sciences Computation and Visualization Laboratory. Marshall served as the co-leader of the SCEC Ventura Special Fault Study Area from 2013-2017, served on the SCEC Science Planning Committee from 2017-2024, and currently serves on the SCEC Board of Directors. Marshall has been the co-leader of the Community Modeling group at SCEC since its inception in 2017 and has been the co-developer of nearly all of the web-based tools that serve the SCEC community models.

Appendix B: Supplementary Figures

This section provides eight supplementary figures related to the geodetic analysis in §3.4.

Figure B.1: Synthetic GPS velocities and the effects of a misaligned profile

Figure B.2: Strain rate inversion of the raw Zeng (2022) data

Figure B.3: Strain rate inversion of the corrected Zeng (2022) data

Figure B.4: Gridded velocities of the raw Zeng (2022) data

Figure B.5: Gridded velocities of the corrected Zeng (2022) data

Figure B.6: Kinematic model strain rates and velocities for a 40° dipping fault similar to the SWBZ

Figure B.7: Kinematic model strain rates and velocities for the ramp-flat-ramp fault geometry described in Figure 3.5.

Figure B.8: Kinematic model velocity predictions on the SAF-normal profile of Figure 3.7c.

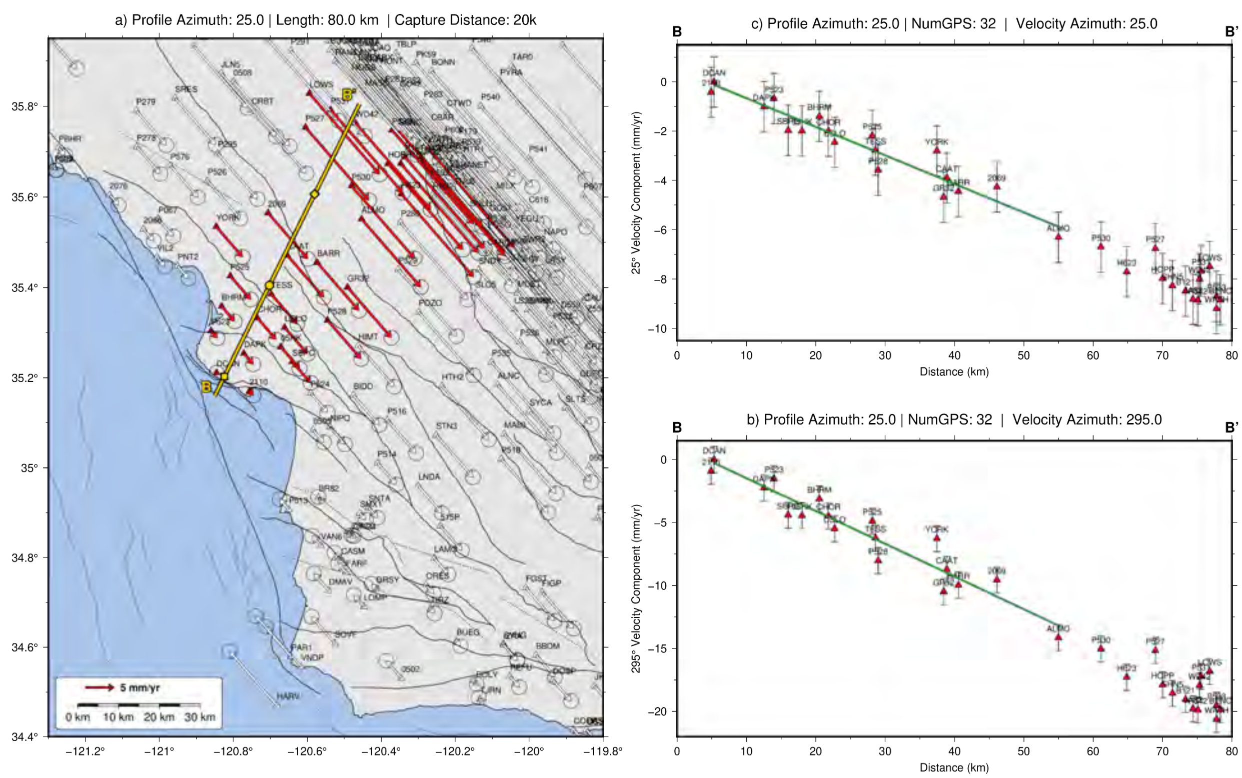

Figure B.1. **(a)** Synthetic GPS velocities with a linear gradient in velocities from simple shear parallel to the SAF. Because the SWBZ-normal profile is not orthogonal to the simple shear direction, this vector mismatch results in an apparent linear contraction. Plotting conventions follow those of Figure 3.7.

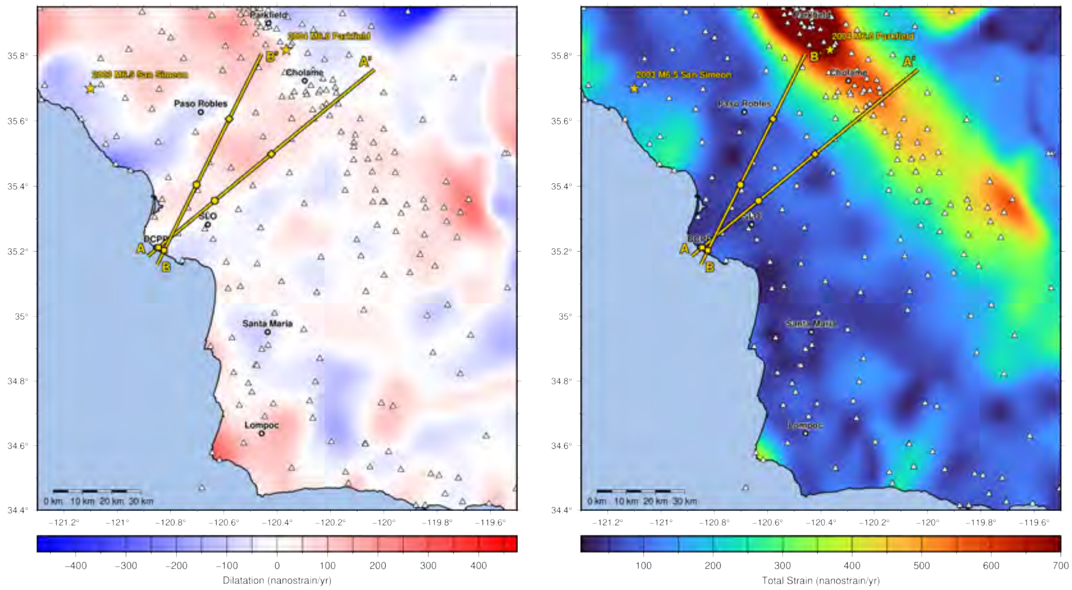

Figure B.2. Strain rate inversions of the raw Zeng GPS velocities plotted as dilatational and total strain rate components. Note that we have saturated the total strain colors at 700 nanostrain/yr, but the values near Parkfield can exceed 1,300 nanostrain/yr. The SAF-normal and SWBZ-normal profiles are shown with along-profile locations of station DCAN (square) and 25 km (circle) and 50 km (diamond) away to the northeast shown. While there is considerable spatial variability, the region southwest of the SAF generally shows extensional dilatation.

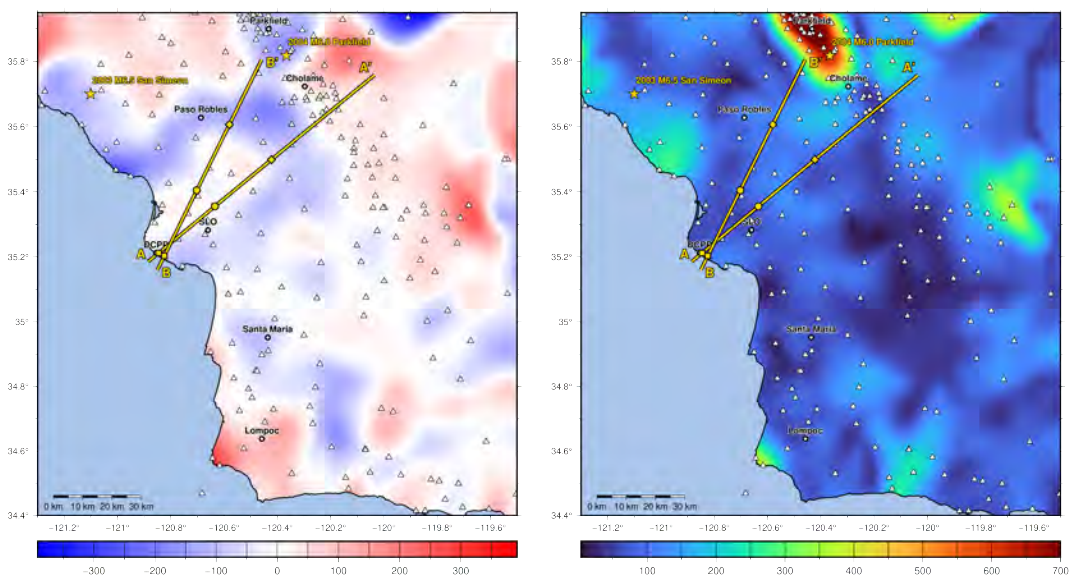

Figure B.3. Strain rate inversions of the corrected Zeng GPS velocities plotted as dilatational and total strain rate components. Note that we have saturated the total strain colors at 700 nanostrain/yr, but the values near Parkfield can exceed 800 nanostrain/yr, which suggests that our dislocation model may not have removed all of the San Andreas creep. Southeast of Cholame, strain due to the San Andreas fault has been successfully removed. Patterns of dilatation and total strain still appear spatially discontinuous, suggesting some non-elastic component of motion or uncertainties may be contaminating the GPS velocities. Labeled features follow from Figure 6.2.

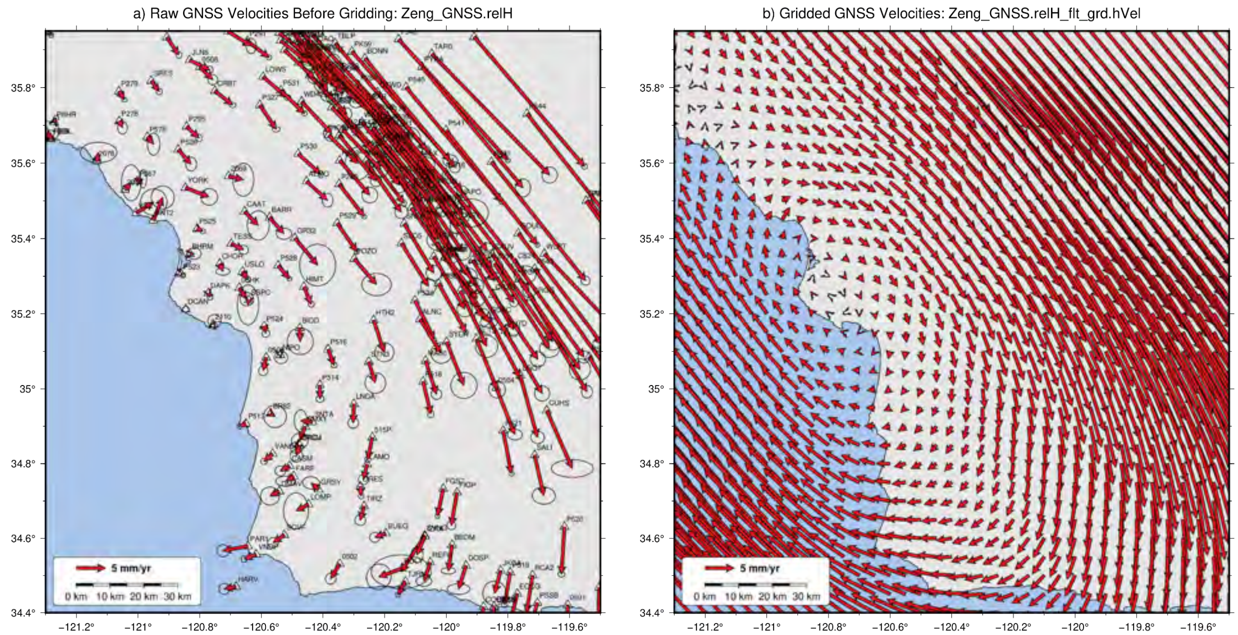

Figure B.4. Uncorrected GPS velocities **(a)** before and **(b)** after gridding using *gpsgridder* (Sandwell & Wessel, 2016). Note that the many vectors offshore are essentially unconstrained by data, but because our strain rate inversions are cropped at the shoreline, these unconstrained velocities have no impact on our reported results except at locations near the coast where the gridded velocities are partially constrained by the onshore GPS data.

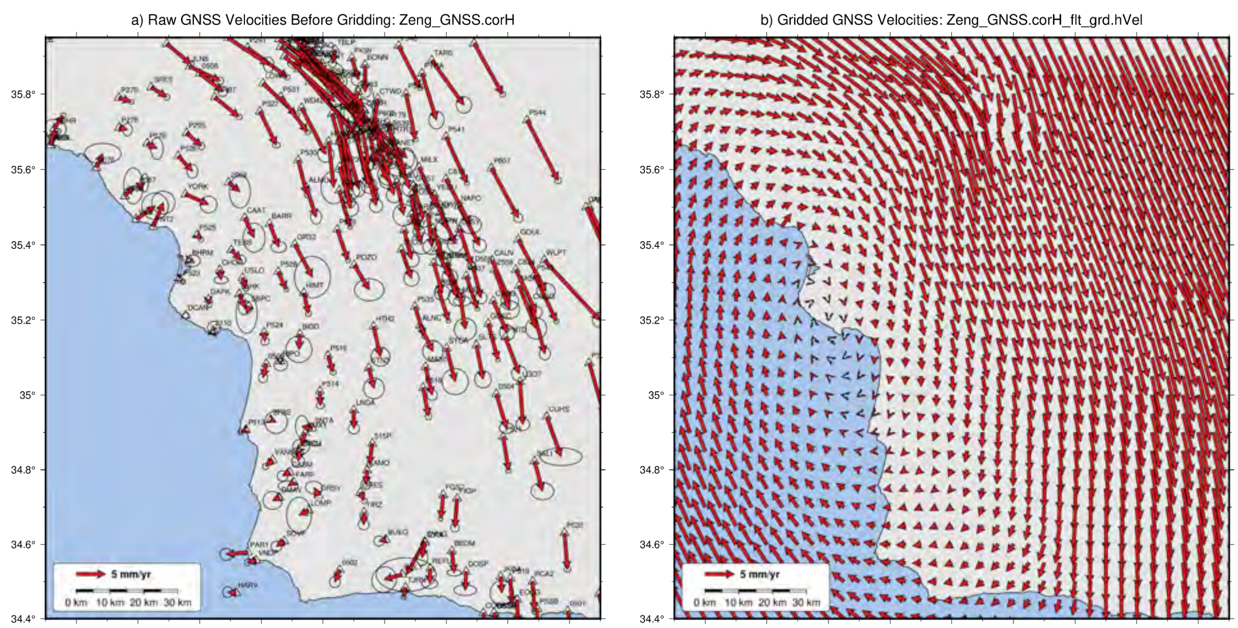

Figure B.5. Corrected GPS velocities **(a)** before and **(b)** after gridding using *gpsgridder* (Sandwell & Wessel, 2016).

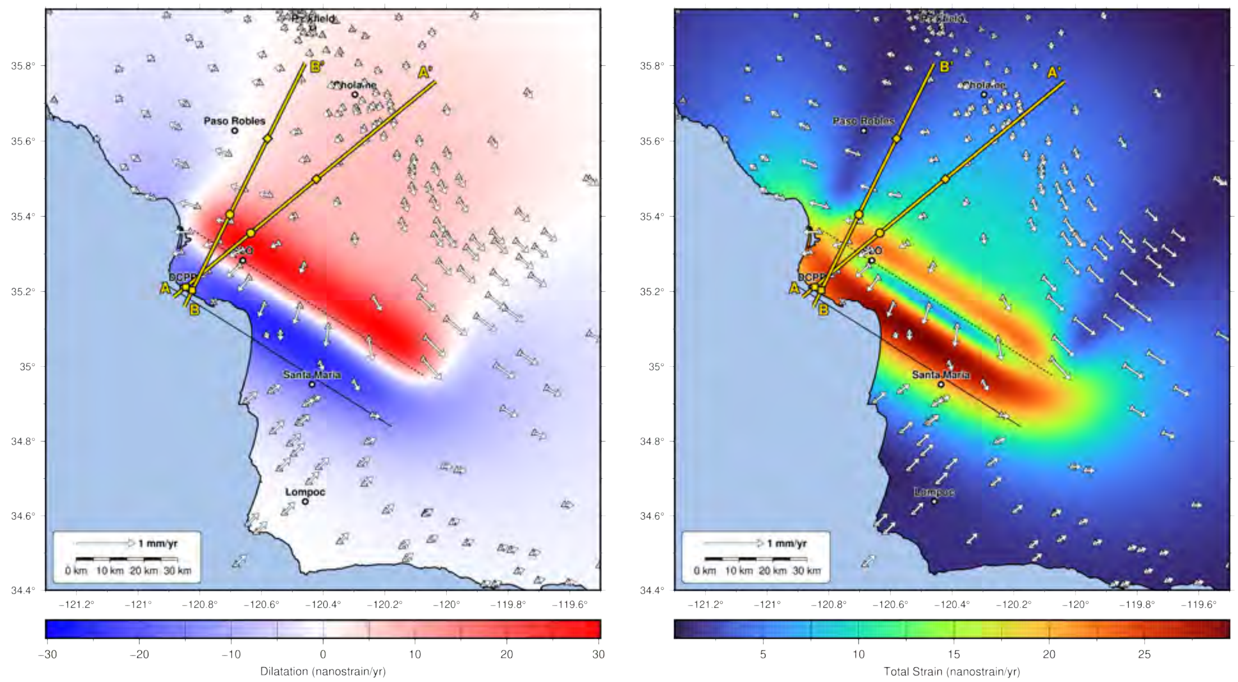

Figure B.6. **(a)** Dilatational and **(b)** total strain rates from a 3D kinematic dislocation model utilizing a 15 km locking depth and a 40° dipping fault with 2.5 mm/yr of slip similar to the geometry of shallowest dipping fault in the SSC24 (SSC24 incorporates a minimum dip of 45°). Plotting conventions are the same as in Figure 3.16.

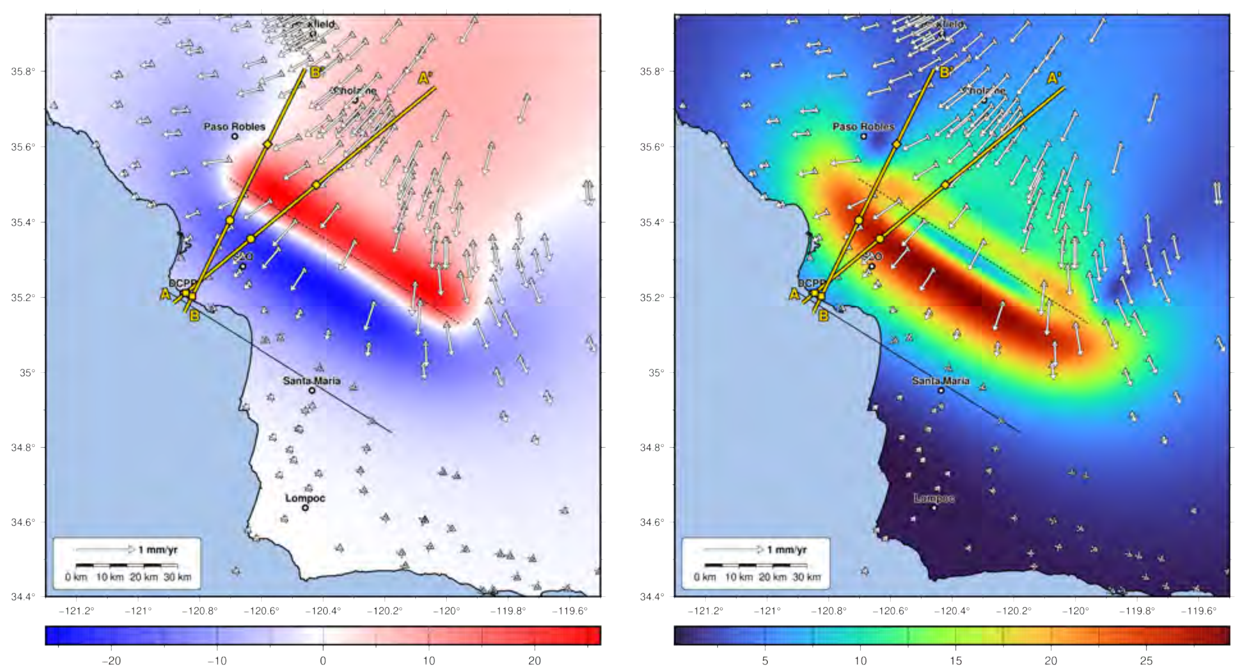

Figure B.7. **(a)** Dilatational and **(b)** total strain rates from a 3D kinematic dislocation model utilizing a 15 km locking depth and the ramp-flat-ramp geometry presented in Figure 3.5. Model results have been cropped to only show onshore strain rates as that is what is available from GPS strain rate inversions. Plotting conventions are the same as in Figure 3.16.

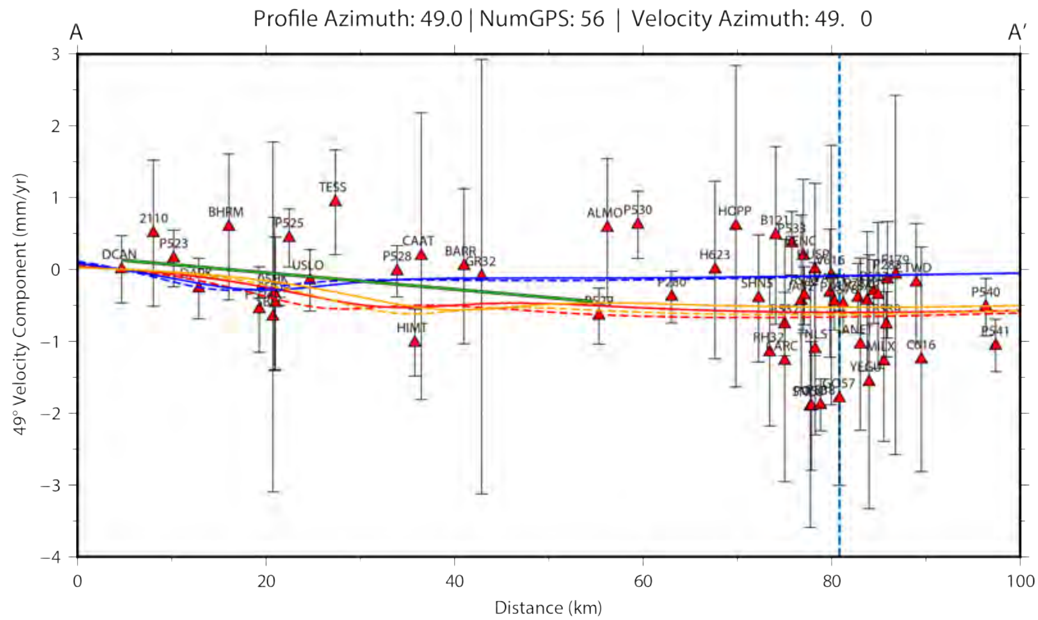

Figure B.8. The SAF-normal profile (Figure 3.7c), showing model-predicted velocities along the profile. Model results include the 25° dipping model (red), 40° dipping model (blue), and the ramp-flat-ramp model (orange) shown for 12 km (dashed) and 15 km (solid) locking depths. The GPS velocities alone cannot discriminate between these models because all of the models produce velocity gradients that are small compared to the velocity uncertainties.